SLOW INVARIANT MANIFOLDS FOR REACTION-DIFFUSION SYSTEMS

A Dissertation

Submitted to the Graduate School
of the University of Notre Dame
in Partial Fulfillment of the Requirements
for the Degree of

Doctor of Philosophy

by

Joshua David Mengers

Joseph M. Powers, Director

Graduate Program in Aerospace and Mechanical Engineering
Notre Dame, Indiana
July 2012

SLOW INVARIANT MANIFOLDS FOR REACTION-DIFFUSION SYSTEMS

Abstract

by

Joshua David Mengers

The method of Slow Invariant Manifolds (SIMs), as developed to model the reduced kinetics of spatially homogeneous reactive systems, is extended to systems with diffusion. Using a Galerkin projection, the governing partial differential equations are cast into a finite system of ordinary differential equations to be solved on an approximate inertial manifold. The SIM construction technique of identifying equilibria and connecting heteroclinic orbits is extended by identifying steady state solutions to the governing partial differential equations and connecting analogous orbits in the Galerkin-projected space. In parametric studies varying the domain length, the time scale spectrum is shifted, and various classes of non-linear dynamics are identified. A critical length scale is identified at which a bifurcation occurs in the equilibria used to construct the one-dimensional SIM. Above this length scale additional real non-singular steady state solutions are found which lead to a diffusion-modified SIM. At these longer lengths, the spectral gap in the time scales indicates that an appropriate manifold for a reduction technique is higher than one-dimensional. This is shown for three examples in closed reaction-diffusion systems: a generic chemical reaction mechanism, an oxygen dissociation reaction mechanism, and the Zel'dovich reaction mechanism of NO production. The extension of SIMs to adiabatic reaction systems is also considered, and results are shown for the Zel'dovich mechanism. Finally, two open chemical systems

are considered: the Gray-Scott reaction mechanism, and a hydrogen-air reaction mechanism. Multiple branches of the SIM are identified, complicating the implementation of the SIM as a reduction technique. Limit cycles are studied and a projection to the SIM across a basin of attraction is shown to provide erroneous results. Low-dimensional Galerkin projections are shown to provide correct order of magnitude predictions for length scales in patterns. The examples are evaluated in the spatially homogeneous case (a one-term projection), a two-term projection capturing the coarsest effects of diffusion, and a high order projection that is fully resolved. The results cast into doubt the SIM as a robust rational reduction technique for reaction dynamics.

To Miriam:

For loving support through this process and for being a phenomenal mother to our children. For all the times that I was late for dinner without calling and the many nights and weekends when I was not able to spend time with you and our family.

Also, for being my proofreader and editor. I thank you for your efforts to make my work grammatically correct, even if I did have to help you with the technical jargon's parts of speech; and yes, for the record, 'dynamical' is a word. Your opinion about which of the figures is your favorite helped to keep me sane, and your names for them put a smile on my face: Figures 4.5 and 5.6 are "basketballs" and "sunrises."

I thank you for being a wonderful wife and supporting me. Without your love I would not have been able to complete my degree.

I love you!

CONTENTS

FIGURES

TABLES

SYMBOLS

Greek

α	Modified Poincaré sphere scaling parameter
$\boldsymbol{\alpha}_{ni}$	Orthonormal normal vectors
$\boldsymbol{\alpha}_t$	Unit tangent vector
β_j	Temperature-dependency exponent of reaction j
γ	Linear stability constant
ϵ	Perturbation parameter
$\boldsymbol{\zeta}_m$	Amplitudes of mode m
$\zeta_{i,m}$	Amplitude of species i mode m
η_i	Dependent variables in Poincaré sphere mapping
κ	Isotropic wave number
$\kappa_{\mathbf{x}}$	Spatial wave number
$\lambda_{i,m}$	Eigenvalue of Jacobian matrix
μ_m	Eigenvalue of diffusion operator
$\bar{\mu}_i^o$	Chemical potential of species i evaluated at the reference pressure
ν_{ij}	Net stoichiometric coefficient matrix
ν'_{ij}	Forward stoichiometric coefficient matrix
ν''_{ij}	Reverse stoichiometric coefficient matrix
ρ	Density

σ_{ni} Normal stretching rates

σ_t Tangent stretching rate

$\tau_{i,m}$ Local time scale

$\tau_{\mathcal{D},m}$ Diffusion time scale of mode m

τ_{kj} Time scale of reaction j

$\tau_{\mathcal{R}}$ Residence time scale of a CSTR

Φ Equivalence ratio

$\phi_m(x)$ Spatial basis function

φ_{li} Species-element matrix

$\hat{\varphi}_{li}$ Modified species-element matrix

χ_i Chemical species i

$\psi_m(x)$ Spatial weighting function

$\dot{\mathbf{\Omega}}_m(\boldsymbol{\zeta}_{\hat{m}})$ Reaction component of amplitude evolution

$\dot{\omega}_i$ Molar production rate of species i

Roman

$A(x,t)$ Linear stability perturbation function

a_j Collision frequency factor of reaction j

C_n Various constants

c_P Mixture specific heat at constant pressure

c_{Pi} Specific heat at constant pressure of species i

$\mathcal{D}$ Mass diffusivity

D_i Dimensionless diffusion coefficient of species i

$\mathfrak{D}_{in}$ Reduction coefficient matrix

$\bar{E}_j$ Activation energy of reaction j

$\mathcal{E}_m$	Relative root mean square error for mode m
$\mathbf{e}(x,t)$	Error in truncated series solution
F	Dimensionless feed rate
$\mathbf{F}(\mathbf{z})$	Non-linear function for amplitude evolution
$\mathbf{f}(\mathbf{z})$	Non-linear function for species evolution
$G(x)$	Linear stability separation of variables spatial function
$H(t)$	Linear stability separation of variables temporal function
h_i	Specific enthalpy of species i
h_i^f	Specific enthalpy of formation of species i
$\mathbf{I}$	Identity matrix
I_n	Label of infinite equilibrium
J	Number of reactions in mechanism
$\mathbf{J}$	Jacobian matrix
J_{ij}	Jacobian matrix
$\mathbf{j}_i$	Spatial diffusive mass flux vector of species i
j_i	Diffusive mass flux of species i
j^q	Diffusive energy flux
K	Reaction rate of $B + B \leftrightharpoons A + A$ mechanism
K_j^c	Equilibrium constant of reaction j
k	Ratio of Gray-Scott reaction time scales
k	Thermal conductivity
k_j	Arrhenius rate of reaction j
L	Dimensionless domain length
L	Number of elements in reaction mechanism
$\hat{L}$	Number of linear dependencies

Le	Lewis number: ratio of thermal to mass diffusivities
$\mathscr{L}_x(\mathbf{z})$	Self adjoint, positive semi-definite linear spatial differential operator
ℓ	Domain length
ℓ_c	Critical domain length
M	Series solution truncation
$\bar{\mathsf{M}}_i$	Molecular mass of species i
m	Basis function mode
$\dot{m}$	Mass feed flow rate
N	Number of species in reaction mechanism
$\mathcal{O}(\ )$	Order of magnitude
P	Pressure
P^o	Reference pressure
$\mathcal{P}$	Projector onto the SIM
R	Dimension of spatially homogeneous system after reduction
R_n	Label of spatially homogeneous equilibrium
$\hat{R}_{n,m}$	Label of spatially inhomogeneous equilibrium for mode m
R'_n	Label of adiabatic equilibrium
$\bar{\mathfrak{R}}$	Universal gas constant
$\mathbf{r}(x,t)$	Residual from the method of weighted residuals
$r(\mathbf{z}_{\mathscr{M}})$	Stretching ratio
r_j	Reaction rate of reaction j
$s(\mathbf{z}_{\mathscr{M}})$	Normalized manifold distance
s_i^o	Specific entropy of species i evaluated at the reference pressure
s_i^f	Specific entropy of formation of species i
T	Temperature

T^o	Reference temperature
t	Time
t	Dimensionless time
V	Volume of the tank reactor
$\mathbf{v}_t$	Tangent vector
x	Distance
x	Dimensionless distance
Y_i	Mass fraction of species i
Y_i^f	Feed flow mass fraction of species i
y	Distance
y	Dimensionless distance
$\mathbf{z}$	Specific moles
z_i	Specific moles of the reduced species
$\hat{z}_i$	Specific moles of all species
z_i	Reduced variable specific mole concentration

Superscripts

c/s	Consideration of cosine/sine amplitude independently
e	Equilibrium
$e:SH$	Spatially homogeneous equilibrium
$*$	Initial conditions
o	Evaluation at reference pressure
$+/-$	Positive/negative amplitude of phase shifted equilibrium

Subscripts

i Species

j Reaction

l Element

m Basis function mode

n Dummy index and others

$\mathscr{M}$ Evaluated on the manifold

Overbars

$\bar{}$ Molar basis

$\tilde{}$ Approximate solution

$\hat{}$ Closely related variable or dummy index

ACKNOWLEDGMENTS

First, I must acknowledge my advisor, Dr. Joseph M. Powers, an amazing teacher from whom I have learned much. I thank Dr. Powers for his wry sense of humor: for helping me to *transition* into a more concise technical writer and to eliminate excessive verbification[1] of perfectly good nouns. Your high standards make me tremendously proud of this accomplishment. You were extremely demanding as my mentor and teacher, but your passion and hard work made it a joy to learn from you. I am truly appreciative of all you have done to help me achieve this accomplishment.

I would also like to acknowledge the members of my doctoral committee: Dr. Andrew Sommese, Dr. Mihir Sen, and Dr. Samuel Paolucci, for their insight and guidance during my studies and assistance reviewing this dissertation.

The present work was funded by the National Science Foundation, grant number CBET-0650843. I also acknowledge additional financial support from various sources at the University of Notre Dame: a graduate fellowship from the Department of Applied and Computational Mathematics and Statistics, a teaching assistantship from the College of Engineering First Year Engineering Teaching Apprenticeship Program, and funding from the Department of Aerospace and Mechanical Engineering and the Donald K. Dorini Fellowship in Hydronics.

[1] the nounification of a perfectly good verb: to verbify

CHAPTER 1

INTRODUCTION

Combustion has been an important source of power for many centuries; since the industrial revolution, it has been a dominant power source. Even today, as society is pushing for faster computing on smaller devices, we still use chemical reactions to generate power for nearly every supercomputer and smartphone. In 2009, the United States generated 87% of its energy through combustion of various fuels [1]. We also burns fuels to move people and goods from place to place. Combustion will continue to play a major role as we seek alternative solutions to generate the power that we demand.

Since it is the driving force in our economy, we desire a better understanding of combustion processes. We seek to learn more about how reactions interact with transport processes such as diffusion with a goal of improving the accuracy of numerical simulations of reactive flows. Better simulations can help to increase our efficient use of fuels, reduce polluting byproducts, and assist in the development of alternative fuel sources.

In addition to combustion modeling, numerical simulations of partial differential equations (PDEs) that model multiscale continuum physics are prevalent across many fields of engineering. To obtain results with fidelity to the underlying continuum model, discrete simulations must generally resolve the entire range of scales present, both spatial and temporal; a large disparity in these scales is

typically referred to as stiffness. The computational costs associated with these stiff simulations grows with the disparity of scales [2], which commonly span eight orders of magnitude.

To computationally solve any set of governing differential equations, they must be approximated as a series of algebraic equations, which can be done using a number of different techniques. The technique chosen, along with the number of equations used to approximate the system, will dictate the accuracy of the solution. Adding more equations (refining the grid) is one simple way to increase the accuracy, but at a direct expense of larger computational costs.

Reactive flows are typically governed by a system of nonlinear PDEs that models the conservation of mass, momentum, energy, and the evolution of a large number of chemical species on domains with generally complicated boundaries. One technique to accurately solve the PDEs is to use a finite difference method with the spatial and temporal grid resolved to the smallest physical scales present in the problem, and evaluate the dependent variables throughout the entire domain. This technique is referred to as direct numerical simulation (DNS). Stiff problems can result in such a large number of computations that DNS techniques are currently intractable for many practical problems on typical engineering scales.

To demonstrate this, we examine the typical scales involved in a DNS of an internal combustion engine. The fastest reaction time scales, based on molecular collisions, are $\mathcal{O}(10^{-9}\ s)$, and the shortest length scales, based on the mean free path, are $\mathcal{O}(10^{-7}\ m)$. For an engine idling at 1000 RPM, one cylinder is $\mathcal{O}(10^{-1}\ m)$ and one cycle is $\mathcal{O}(10^{-2}\ s)$. Assuming there are $\mathcal{O}(10^{2})$ species and, therefore, operations per grid point, a full three-dimensional DNS that resolves all scales executed on an $\mathcal{O}(10^{15}\ flops)$ computer would take $\mathcal{O}(10^{12}\ s)$ to simulate, which is

approximately 30,000 years. Figure 1.1 depicts the typical range of scales resolved in DNS and other common solution techniques.

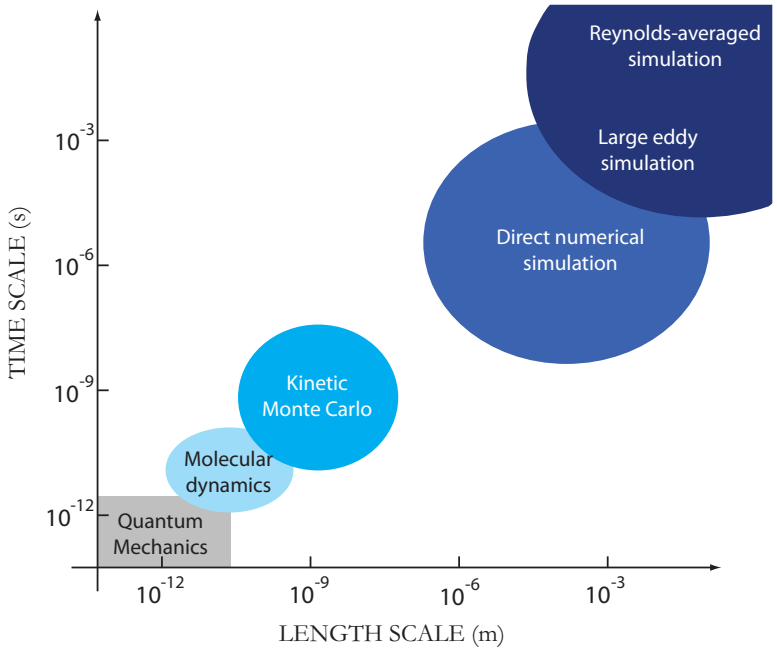

Figure 1.1. Range of scales in combustion processes. Reprinted with permission from Manley et al. [3]. © 2008, American Institute of Physics

To reduce computational costs, many numerical methods use *ad hoc* approximations, and are therefore prone to error. One naïve reduction technique assumes instantaneous combustion. By ignoring all reaction time scales, these simulation predictions are prone to errors and will likely be inconsistent with the observed physical kinetics. If in the design of a SCRAMJET, a prediction is made based on a simulation that omits the small but finite time scale, that engine would likely

fail. This result is due to the small reaction time scales, which were neglected, being larger than the advection time scales. The energy released from combustion would be realized downstream from where predicted. Other techniques are built on better assumptions, but there is room for improvement in those approximations, especially in the case of reaction with transport.

Three options for continuing combustion research are to i) continue to use *ad hoc* approximations with uncertain error bounds, ii) run costly DNS or physical experiments, or iii) develop improved rational reduction techniques. We choose to pursue option iii), because it can increase the accuracy of less costly simulations, allowing for a larger quantity of reliable tests to be run during the design process.

The method we study is an approximation based on isolating the slow time scales of the system's actual dynamics. We implement a geometric analysis technique to identify the slow dynamics. This technique uses a concept called phase space, where the dependent variables of a system are plotted and time is implicit. As the dependent variables evolve, a path is generated in phase space describing this evolution, which is called a trajectory. This dissertation describes how to use the mathematical properties of the dynamical system in phase space to find a canonical trajectory, a slow invariant manifold (SIM), that captures the slow dynamics present in the full system. The goal is to produce a less costly simulation by projecting the initial conditions onto this lower dimensional manifold. This technique has the potential to reduce the errors associated with *ad hoc* approximations since it can identify the slowest dynamics of the system. Since the fast dynamics equilibrate more quickly, the long time dynamics of the system are governed by the slowest time scales. The fast dynamics equilibrating can be thought of as a trajectory in phase space relaxing onto a slow manifold, where

the dynamics on the manifold then govern the system as it approaches equilibrium. A sketch of this is presented in Figure 1.2, which depicts slow manifolds in a three-dimensional phase space for dependent variables z. The sheet outlined

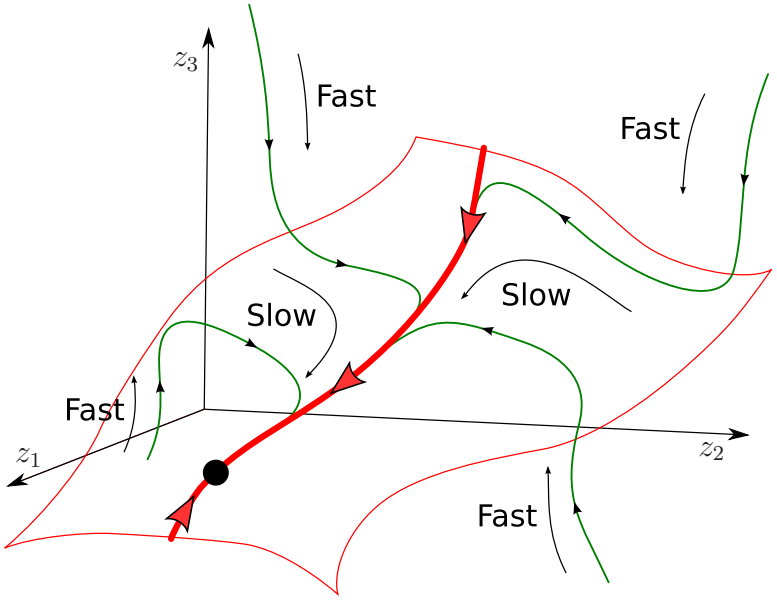

Figure 1.2. Slow manifolds in phase space, adapted from Singh [4].

in thin red is a two-dimensional slow manifold on which slow dynamics evolve. The bold red line is a one-dimensional slow manifold which is a sub-manifold of the two-dimensional slow manifold. The one-dimensional manifold contains the system's slowest dynamics; therefore, neighboring trajectories collapse onto it as their fast dynamics equilibrate. The black dot is an equilibrium sink, which is the steady state solution of the system.

We construct a SIM that is based on the governing PDEs of a reaction-diffusion system. For trajectories to rapidly collapse onto the SIM, there must be a sufficient spectral gap in the time scales. This same separation of scales typically makes simulations costly. Using the SIM, however, allows us to leverage the time scale disparity; by identifying the slowest dynamics, the SIM accurately captures the long time behavior of the system. We will employ the construction technique pioneered by Davis and Skodje [5] for spatially homogeneous reactive systems. In this method, branches of the one-dimensional SIM are specific heteroclinic orbits that connect the systems' equilibria; therefore, one must first identify all equilibria of the system. To be a branch of the SIM, the heteroclinic orbit must connect a non-physical saddle equilibrium that has one positive eigenvalue to the physical equilibrium sink. Trajectories are integrated from initial conditions that are perturbed from the non-physical saddle along its only unstable eigenvector; any such trajectory that osculates with the eigenvector of the physical equilibrium whose eigenvalue corresponds to the slowest local time scale is a branch of the one-dimensional SIM. As sketched in Figure 1.3, the SIM connects the saddle to the sink, and ideally trajectories originating away from the SIM are drawn toward it; however, we find that nonlinearities can cause nearby trajectories to diverge from SIMs that are constructed by integrating heteroclinic orbits as sketched in Figure 1.4.

We extend this SIM construction technique to reaction-diffusion systems by using the method of weighted residuals to reduce the governing PDEs into a system of ordinary differential equations (ODEs); specifically, we employ the Galerkin method. This reaction-diffusion equation is inherently dissipative, meaning that as time increases, higher spatial frequency terms decay exponentially, which proves

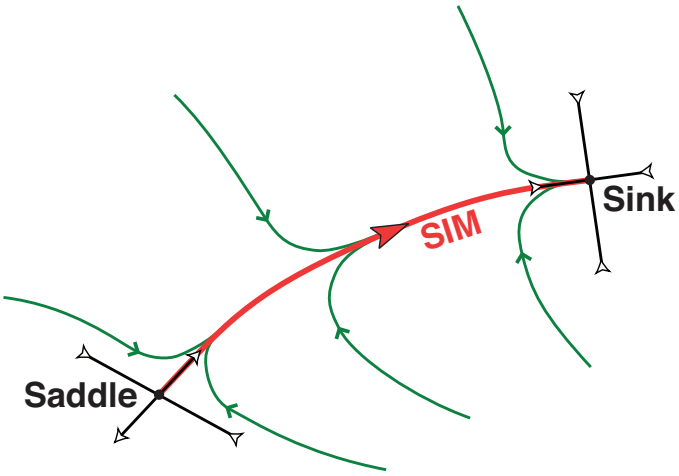

Figure 1.3. Sketch of one-dimensional SIM construction.

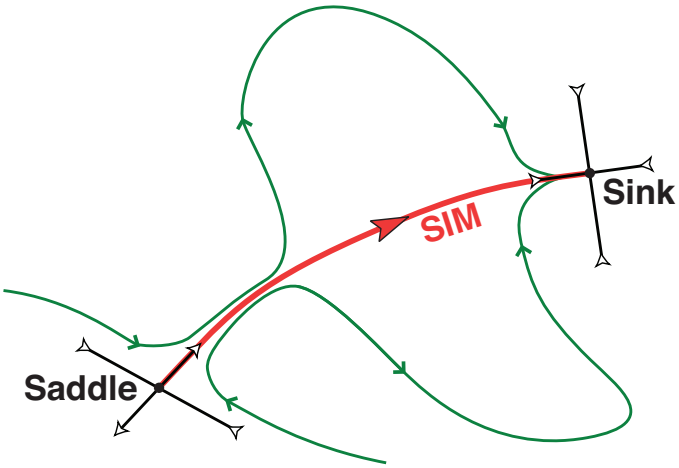

Figure 1.4. Sketch of nonlinear repulsive SIM.

useful in the subsequent analysis.

We thus project solutions to the governing reaction-diffusion PDEs onto an Approximate Inertial Manifold (AIM) [6, 7]. Here we emphasize that this AIM is not an invariant manifold as the acronym can be easily confused. This is the same technique that Lorenz [8] used to simplify the Navier-Stokes equations. The resulting low-dimensional dynamical system has steady state solutions, or equilibria, that lend themselves to the same SIM construction techniques as spatially homogeneous systems. These equilibria in the Galerkin projection correspond to steady state solutions to the governing PDE. We then construct a one-dimensional SIM using heteroclinic orbits which approximates the time-evolution of a spatial function from a non-physical steady state to the physical equilibrium. Thus, our work is distinguished from previous reaction-diffusion reduction techniques, which were developed independent of inertial manifold theories [9, 10].

Our method results in a concise analytical coupling of reaction and diffusion time scales. Other methods, such as operator splitting [11–13], consider reaction and diffusion independently. To apply operator splitting, one integrates reaction terms implicitly and separately integrates diffusion and advection terms explicitly. This contrasts with our approach, which is built upon an underlying physical coupling of reaction and diffusion processes. Our results will demonstrate a full coupling between reaction and diffusion length and time scales in a fashion consistent with Al-Khateeb et al. [14], Mazaheri et al. [15], as well as classical diffusion theory [16, p. 126 and §19.1] and [17, p.475]. This coupling of scales has implications on the necessary grid resolution in discrete simulations which implement spatially homogeneous manifold methods. The lower bound of wavelengths modeled is dependent on the spatial resolution; if a grid is too coarse, the slowest time

scale present in a discrete cell will represent diffusion across the longest unresolved length scale. Since the SIM is dependent on capturing the slowest time scales, a spatially homogeneous manifold proves inadequate across long length scales.

We model reaction-diffusion systems that exhibit an infinite set of time scales that arise from the combined effects of reaction and diffusion. In the spatially homogeneous limit we find a finite set of reaction time scales. By treating the domain length as a variable parameter, we change the spectrum of length scales and, therefore, change the spectrum of diffusion time scales. This allows us to study various classes of behavior of reaction-diffusion systems.

We then study the use of the SIM as a reduction technique for open reaction-diffusion systems. Well resolved simulations of these systems exhibit limit cycle behavior and pattern formation. Our method of SIM construction employes heteroclinic orbits, and is therefore unable to predict limit cycle behavior, since the set of all heteroclinic orbits is disjoint from the set of all limit cycles. We show the pitfalls of projecting onto a SIM for systems with limit cycle behavior. We also explore pattern formation and show that analysis of a low order Galerkin projection of these systems can predict the length scale of the pattern. The construction of SIM branches for these examples identifies many concerns about the implementation of the SIM as a rational reduction technique, which are summarized in Table 1.1.

This dissertation is organized into six chapters. Chapter 2 provides a review of the relevant literature. Chapter 3 describes the mathematical model and our methods of reduction. The next two chapters examine the results of closed (Chapter 4) and open (Chapter 5) reaction-diffusion systems. Finally, Chapter 6 provides a discussion of our methods and results and includes details on future work.

TABLE 1.1

LIST OF SHORTCOMINGS IN SIM IMPLEMENTATION

Shortcomings	Description	Examples	
		Section	Pages
Multiple branches	Using heteroclinic orbits to construct the SIM, multiple branches were found for the same system. This presents a problem in identifying the branch on which to project.	4.1.3.2 5.1.1 5.2	99-101 111-115 144-150
Projection out of basin of attraction	Care is necessary when projecting onto a SIM in systems with multiple basin of attraction to ensure that the projection does not cross the boundary of a basin of attraction.	5.1.1	112-115
Heteroclinic orbit attractiveness	SIMs constructed using heteroclinic orbits are not necessarily attractive along the entire manifold. Attractiveness of the SIM needs to evaluated to ensure nearby trajectories decay onto the manifold.	4.1.1 5.2 F	59-60 147-150 173-188
Reaction-diffusion SIM length scales	Spatially homogeneous SIMs only accurately describe the long time dynamics of reaction-diffusion systems with domains shorter than a critical length scale where reaction and diffusion processes have the same time scales.	4.1.1 4.1.2 4.1.3.1	56-59 68-70 85-88

CHAPTER 2

LITERATURE REVIEW

In this chapter we review relevant topics in the literature, which we split into two sections. In the first section we review reduction techniques that are similar to the ones we employ. In the second section we discuss other topics relevant to our study such as limit cycles, pattern formation, and verification and validation.

2.1 Reduction models

There have been efforts over many decades in model reduction techniques to decrease the computational costs of simulating reactive flows while maintaining as much consistency with the underlying physics as possible. The reviews of Griffiths [18] and Lu and Law [19] provide background information on the strength and weaknesses of many reduction techniques such as principal component analysis, repro-modelling, and skeletal reduction. We shall limit the focus of this review to reduction techniques that are more relevant to our extension of the SIM to reaction-diffusion systems.

Two of the simplest reduction methods are the frozen reaction assumption and the equilibrium flow assumption, described by Vincenti and Kruger [20]. In the frozen reaction assumption the chemical source term is set to zero. This assumes no reactions and is only valid in the limit of low temperatures where reaction

times are slow. The opposite limit is equilibrium flow, which assumes all species are in chemical equilibrium throughout the flow. This requires infinitely fast reaction times and is only valid if reaction times are much shorter than transport times. While these methods are simple and apply to flows with chemistry and transport, they neglect either the chemical or transport time scales, and often fail to accurately describe the coupling of the two mechanisms. To find a better reduction, we investigate spatially homogeneous systems since they simplify the analysis in a rational limit of the full reaction-diffusion systems.

2.1.1 Spatially homogeneous

When a simplification is made that the transport terms in the governing PDEs are negligible, the result is a reduction to a spatially homogeneous system which is governed by ODEs. For such systems, a large number of reaction methods have been developed. The first of these methods requires reducing the elementary reactions to one- or two-step models [21, 22]. This method is *ad hoc* in fitting the reaction rates but greatly simplifies the evaluation of the chemistry. Sensitivity analysis [23] is a similar technique that is used to determine which species and elementary reactions are important and which ones can be removed. Another set of methods, optimization approaches [24], again reduces the number of reactions and species. These three methods reduce the number of dependent variables in the reaction model, but they are not concerned with reducing the stiffness of the system. This is problematic because the fastest time scales must still be resolved.

As an alternative, manifold methods were developed to address the effects of stiffness. Manifold methods are a class of reduction technique that attempt to reduce the computational cost by projecting dynamics onto lower dimensional

manifolds which are chosen to capture the long time dynamics of the system. The justification for manifold methods as a reduction technique is based on a geometric phase space analysis where families of nearby trajectories are predicted to collapse onto low-dimensional manifolds.

One method that is built to reduce the stiffness of the system is the lumping method [25, 26] where the reduced dependent variables are a linear or nonlinear [27, 28] function of the original dependent variables. The nonlinear lumping method isolates the slow variables using a singular perturbation analysis, which restricts it to simple systems. A difficult step in lumping methods is finding the lumping and inverse lumping transformations. The quasi-steady state assumption (QSSA) [29] is another technique used in an attempt to reduce the stiffness of the system. Certain species that react with fast time scales are assumed to be in a quasi-steady state, which yields algebraic constraints for those species instead of differential equations. A similar simplification is the partial equilibrium assumption, where elementary reactions that are deemed fast are assumed to be in equilibrium. This assumption also yields algebraic constraints for some variables. Partial equilibrium and QSSA can be used in conjunction with each other to create a larger set of algebraic constraints. Similar to these methods, rate-controlled constrained-equilibrium (RCCE) [30–32] reduces differential equations to algebraic constraints based on the reaction progressing through states of constrained equilibrium at the rate of the slowly changing constraints. More recently, Tang and Pope [33] used the RCCE to build the constrained equilibrium manifold (CEM) and introduced the idea of a close parallel inertial manifold (CPIM). The close parallel assumption is made based on the rate of change vector being close enough to the manifold to be approximated by the linear dynamics of the

system, and exists in the tangent space of the CEM. While lumping methods, QSSA, RCCE, and CPIM are built to reduce the stiffness of the system, they do not necessarily succeed because they do not consider the time scales of the entire dynamical system.

The following methods use local properties of the dynamical system to evaluate and segregate time scales of the ODEs. These methods examine the eigenvalues of the Jacobian matrix to identify time scales. Computational singular perturbation (CSP) [34, 35] identifies and eliminates local fast exhausted modes, leaving the slower currently active modes. CSP segregates these modes by an iterative scheme that identifies the corresponding local basis. The intrinsic low dimensional manifold (ILDM) [36] is also based on the local fast and slow eigenvalues. Using the corresponding eigenvectors as a basis, algebraic constraints are built for the basis corresponding to the fast eigenvectors, while the differential equations remain for the basis corresponding to the slow eigenvectors. This makes the ILDM similar to the QSSA and RCCE, but the ILDM is based on the system's dynamics while the others are based on *ad hoc* assumptions. Bykov et al. [37] presented global quasi-linearization (GQL), which is built on the framework of ILDM but has global character based on a singularly perturbed vector field. The GQL method is different than the CSP and ILDM in that it evaluates a modified linearization, not the Jacobian matrix. Another reduction technique is the G-Scheme by Valorani and Paolucci [38]. The local dynamics in this method are segregated into four types of modes: fast, active, slow, and conserved. The G-Scheme reduces the stiffness and number of dependent variables integrated, since it only solves for the evolution of the active modes and uses projections and algebraic constraints for the other modes. CSP, ILDM, GQL, and G-Scheme all approximate the manifold in the

system that embodies the slowest dynamics; however, one shortcoming of these methods is they are not invariant manifolds (IMs).

For a manifold to be invariant, the trajectory of an initial condition on the manifold must lie completely within the manifold for all later times. This is advantageous for a reduction technique since after the projection onto an invariant manifold, additional errors will not be incurred. While there has been some dispute about definition of a slow manifold [39–41], we seek the Slow Invariant Manifold (SIM), which we define as the canonical IM that encompasses the slowest dynamics of the system. Our definition of the SIM is consistent with other usage in the combustion community [5, 42–50].

There have been many methods proposing how to calculate the SIM. The first is an iterative technique, where an initial guess is refined through iterations to find the SIM. This method was introduced using algebraic functional iteration by Fraser [42–44]. A computational improvement to this method was made by Davis and Skodje [5]. For some systems the SIM can be found analytically by a perturbation analysis, as shown by Kaper and Kaper [45]. Another method of finding SIMs is by connecting heteroclinic orbits between a saddle equilibrium of the system and the physical equilibrium sink [5, 47–49]. Lebiedz [50] suggests a variational principle be used as a construction technique which asymptotically converges to the SIM. The saddle equilibria may be located at infinity [51], in which case a transformed coordinate system must be used to find them [5, 49]. While these methods find the canonical SIM, it is difficult to extend them to higher dimensional manifolds [4, 48, 49], and they do not guarantee that a SIM will exist for the system [49].

Our preferred method to calculate the SIM is by connecting the system's equi-

libria through integration of heteroclinic orbits [5]. This method is based on finding and characterizing the system's equilibria points. Powers and Paolucci [52] clarified an earlier proof by Zel'dovich [53] that shows there is a unique physical equilibrium for closed spatially homogeneous systems. There are many techniques in the literature to find that equilibrium, such as the one given by Pope [54]. To find the system's other equilibria, an efficient method based on homotopy continuation [55] has been shown to be effective for polynomial systems that would arise from isothermal chemistry [49]. These methods can still be used to find equilibria for systems which are not isothermal, but would have to be applied iteratively. Characterizing each of the points is typically done following the Hartman-Grobman theorem for hyperbolic critical points [51]. A hyperbolic critical point is an equilibrium with no zero eigenvalues, and the Hartman-Grobman theorem states that a hyperbolic equilibrium's character is described by its linearized system. The linearized system is evaluated by the eigenvalues of the Jacobian. Equilibria with zero eigenvalues are nonhyperbolic and must be characterized using the more rigorous technique of the normal form theory [51, 56].

Because of the difficulties in constructing the SIM, there have been other methods proposed that find IMs other than the SIM. One is the minimum entropy production trajectory (MEPT), presented by Lebiedz [57]. MEPT finds a trajectory that has minimized the system's entropy production rate. This technique is based on Prigogine's minimum entropy production principle [58], despite the fact that many have shown [59–61] that the principle is only valid on a stationary state of a non-equilibrium system. The method of invariant manifolds (MIM) [62, 63] is an iterative technique to build an invariant manifold based on an arbitrary thermodynamic projector. The quality of the MIM depends on the choice of

the thermodynamic projector. The invariant constrained equilibrium edge (ICE) [64, 65] manifold is constructed from the trajectories initiating at a manifold of constrained equilibria on the boundary of the system's physical domain. The ICE manifold is also presented with the idea of a pre-image curve (ICE-PIC) as a simple way to construct higher dimensional manifolds. However, Al-Khateeb et al. [49] show that the MEPT and ICE manifolds are not the SIM of the system, and give a detailed discussion on using thermodynamic quantities far from equilibrium.

Another manifold is presented by Davis and Tomlin [66, 67] in a study of the spatial dynamics of low-dimensional manifolds on steady one-dimensional laminar flames. Steady flames are described by Davis and Tomlin [66] as "trajectories on the stable manifold of a saddle fixed point." They present the idea that these stable manifolds have lower dimensional attracting sub-manifolds as the trajectories approach the saddle point, and they use iterative techniques to generate one-dimensional and two-dimensional attracting sub-manifolds. While these manifolds are not spatially homogeneous, they are still governed by ODEs since they are steady and in one spatial dimension.

2.1.2 Reaction and transport

Since most systems in combustion are not spatially homogeneous or steady, we are interested in reduction techniques for systems governed by PDEs instead of ODEs. This does not mean that the spatially homogeneous reaction models are without merit, as these models have been extended to reaction-diffusion systems in different ways. A review of these extensions is given by Ren and Pope [68], where they categorize the approaches into two types: i) those in which a slow manifold is built based on the governing PDEs, which include transport, and ii)

those in which the slow manifold used is the spatially homogeneous manifold, and the method must account for reaction-transport coupling. A review of both types of approaches follows.

Maas and Pope [69, 70] extend the spatially homogeneous ILDM to PDEs by viewing transport processes as disturbances of the chemical reacting system and projecting those disturbances onto the ILDM. The justification is based on the assumption that the time scales of the perturbation are slow compared to the fast chemical time scales. This causes the components of the perturbation in the direction of the fast chemical time scales to relax back to the slow dynamics represented on the ILDM. This approach is typically called the Maas-Pope projection (MPP).

A similar approach, presented by Ren et al. [71], extends the ICE-PIC to spatially inhomogeneous systems. This approach applies a close-parallel assumption similar to the one that builds a CPIM for spatially homogeneous systems [33]. For reaction transport systems the close parallel assumption leads to a transport correction factor that is added to the spatially homogeneous rate of change vector. The close parallel assumption is not unique to the ICE-PIC method; Ren and Pope [72] present it using the ILDM.

The CSP method is also extended to PDEs by Lam [73], who uses a projector operator on the transport terms. Lam also emphasizes the importance of the modification of diffusion terms to compensate for the use of spatially homogeneous reduced chemistry approximations, as using unmodified terms ignores important coupling in the system.

The other approach uses a new reduction technique for the PDEs rather than adjusting the spatially homogeneous technique to account for transport. This

technique is based on the idea of reducing the infinite dimensional system to just a few dimensions on a manifold. An example of this approach is given by Hadjinicolaou and Goussis [74]. They present an extension of CSP to reaction-diffusion systems by segregating the system on a basis of local slow and fast vectors, which are functions of space and time. These bases are then used to construct a new system of slow PDEs, along with algebraic constraints that represent the fast modes.

Another technique given by Singh et al. [75] is the approximate slow invariant manifold (ASIM). This method again segregates the local time scales into basis vectors based on the local eigenvectors of the Jacobian of the spatially homogeneous reaction term. The dynamics of the full PDEs are then projected onto this basis and algebraic and differential constraints are found which define the infinite dimensional ASIM. It is noted that the ideal basis for projection is the eigenfunctions that include the spatial operator; however, this makes the basis infinite dimensional, complicating the analysis.

Similar to the ASIM, Bykov and Maas [76] extend the ILDM to PDE systems by relaxation to reaction-diffusion manifold (REDIM). REDIM is a method similar to the ASIM, except it is given explicitly as the stationary solution of a parabolic system using the ILDM as an initial guess. Another modification to the ASIM is given by Ren and Pope [72]; by using assumptions similar to the close-parallel approach, they formulate the governing PDEs for the ASIM explicitly in terms of prescribed variables.

The SIM has also been extended to reaction-diffusion systems by Davis [9, 77]. Low-dimensional manifolds are built in the infinite dimensional function space by using the predictor corrector method, presented by Davis and Skodje [5], and by

modifying the MPP [69, 70].

Another technique presented by Adrover et al. [10] is the stretching-based reduction (SBR) approach for reduced kinetics on reaction-diffusion systems. SBR uses a normal stretching rate analysis of local linear dynamics to generate a local coordinate that segregates the slow stretching directions from the other time scales. The SBR approach to PDEs treats the reaction and diffusion operators as a single entity. Adrover et al. [10] note that the other reduction techniques based on PDEs described here are developed independent of inertial manifold theories; Davis [9] notes this as well.

2.1.3 Inertial manifold techniques

An inertial manifold is defined as a finite-dimensional Lipschitz manifold which is positively invariant and attracts all trajectories exponentially [6, 7]. Because reaction-diffusion systems are dissipative, they can be projected onto an AIM. One standard technique of doing this is the Galerkin method, where the solution to the governing PDE is approximated as an infinite series of the product of time-dependent amplitudes and their corresponding basis functions. An ideal choice for basis functions is the eigenfunctions of the spatial operator, which can be approximated if they are not easily found. If the spatial operator is self-adjoint, its eigenfunctions will be orthogonal [78]. The infinite series solution can be accurately approximated by truncating at a sufficiently large finite value. ODEs for the time evolution of each amplitude can then be obtained by taking the inner product of the governing PDE with each basis function. This larger system of ODEs approximates the dynamics of the PDEs on a linear space. One classic example of an inertial manifold is the system presented by Lorenz [8], which is

built using a three term standard Galerkin method to represent an atmospheric flow. The resulting deterministic system of ODEs has the well known chaotic attractor in phase space. Other studies have examined the accuracy of Galerkin methods [6, 7, 63, 79–81], which describe the desirable properties of AIMs for dissipative systems. Temam and Wirosoetisno [82] include a concise distinction between AIM and slow manifolds: inertial manifolds consider a spectral truncation of a Laplacian operator, while slow manifolds consider the eigenvalues of a general forcing term.

One specific method, the nonlinear Galerkin method [83], extends this idea by adding what Robinson [6] calls "slaving rules." This method assumes a similar series solution as the standard Galerkin approach, but it retains twice as many terms. The first half of the amplitudes (long wavelength) are still approximated with ODEs, but are now coupled to the second half of the amplitudes (short wavelength). The short wavelength amplitudes are approximated with algebraic constraints (slaving rules) to minimize an error. This creates a system of differential algebraic equations that project the solution of the governing PDEs onto a nonlinear manifold. The nonlinear Galerkin method creates a reduction in error because the long wavelength amplitudes may have large contributions from the short wavelength, despite the short wavelengths having small amplitudes from the dissipative governing equations. Garcia-Archilla and de Frutos [84] present results that compare the nonlinear and standard Galerkin methods, and they find that the nonlinear Galerkin methods require a higher computational cost to converge to the same error. Therefore, we do not employ slaving rules in our analysis.

These Galerkin techniques all project large or infinite-dimensional systems onto lower-dimensional AIMs. The benefit of this is exponential attraction of the

trajectories, which allows for a high order of convergence for dissipative systems, such as those arising from reaction-diffusion problems. This implies that using an inertial manifold can provide a smaller error while retaining fewer terms than other methods, such as a finite difference approximation.

2.2 Related topics

In this dissertation we explore reduction techniques in the context of various chemical systems. We therefore include some relevant discussion of the chemical systems considered. We also discuss the important topic of verification and validation.

2.2.1 Limit cycles

Some open reactive systems exhibit limit cycles, chaos, and pattern formation, such as continuous flow stirred tank reactors (CSTRs) [85]. In CSTRs, species flow in and out of a tank as the reaction proceeds; the feed flow can provide more reactants while removing some products. The tank is assumed to be spatially homogeneous from mixing. An extension of this idea models reaction-diffusion systems in a similar fashion to CSTRs by allowing spatial variations in the reactor.

Many simple chemical systems that display limit cycles and pattern formation have been studied, such as Belousov-Zhabotinsky mechanisms [86–88], the Brusselator [89], and the Gray-Scott mechanism [90–92]. Desroches et al. [88] consider many systems that display mixed mode oscillations and establish a systematic framework for studying their properties. Adrover et al. [10] also study limit cycles and chaotic reaction-diffusion systems in the context of SBR, which shows that SBR is able to capture asymptotic behavior of oscillations. Construction of many

reduction techniques (SIM, ILDM, ICE-PIC) rely on a fixed point equilibrium and constant elemental constraints. These properties are not guaranteed in open systems.

Following the studies of Pearson [93], Marchant [81], and others [12, 94, 95], we examine the Gray-Scott mechanism in the context of constructing a SIM and analyzing pattern formation in a low-dimensional Galerkin projection. Marchant's [81] study of the Gray-Scott reaction system is particularly relevant. Galerkin methods are used to study the spatial structure of the system's patterns, showing that low-order approximations can reasonably predict stability of various patterns.

2.2.2 Verification and validation

Following Boehm [96], Blottner [97], Roache [98, §2.3], Oberkampf et al. [99], Oberkampf and Roy [100], and others, we adopt a nuanced distinction between the terms "verification" and "validation." Verification is the practice of ensuring that the simulation approximates the model equations correctly; it is a purely mathematical exercise. On the other hand, validation is the practice of ensuring that the model system is correctly approximating a physical experiment. The difference between these two terms is subtle but important. Verification is important whenever a model system is implemented, to ensure the system is solved correctly. Validation is necessary when the model system's credibility comes into question.

We evaluate systems using a variety of simplifying assumptions such as trivial geometries, isothermal or adiabatic reactions, and micrometer domains. A consequence of these assumptions is that no physical experiments are readily available for comparison, preventing validation. We will, however, use well-resolved simulations to verify our results. The reasons for analyzing these mechanisms is to gain

a better understanding of typical dynamical systems in combustion in the context of simple systems. We study isothermal systems to allow us to use algebraic and homotopy continuation methods to find the equilibria of low-order polynomial systems. When we consider an adiabatic system, we do so for a simple reaction mechanism to facilitate the analysis. The insight we gain from studying these simple systems assists in developing a general reduction technique that can be applied to realistic systems. Many others [5, 47–49, 57, 64] have studied manifold methods in the context of similar simplifying assumptions.

CHAPTER 3

METHODOLOGY

In this chapter we introduce the mathematical model which we will evaluate. We then show a series of reductions to this model and describe our technique for analysis.

3.1 Mathematical background

We are interested in a rational reduction of systems of PDEs of the form

$$\frac{\partial \mathbf{z}}{\partial t} = \mathbf{f}(\mathbf{z}) - \mathscr{L}_x(\mathbf{z}), \tag{3.1}$$

where $\mathbf{z} \in \mathbb{R}^R$ are dependent variables, $\mathbf{f}$ are non-linear functions that represent rates of change due to reaction, and $\mathscr{L}_x$ is a self-adjoint, positive semi-definite, linear spatial differential operator that models diffusion. These restrictions on $\mathscr{L}_x$ allow for a simple examination of the coupling between reaction and diffusion processes. The one-dimensional spatial domain is of length ℓ, $x \in [0, \ell]$, and the temporal domain is $t \in [0, \infty)$. We choose to study two types of boundary conditions: i) homogeneous Neumann boundary conditions,

$$\left.\frac{\partial \mathbf{z}}{\partial x}\right|_{x=0} = \left.\frac{\partial \mathbf{z}}{\partial x}\right|_{x=\ell} = \mathbf{0}, \tag{3.2}$$

and ii) periodic boundary conditions,

$$\mathbf{z}(0) = \mathbf{z}(\ell) \quad \text{and} \quad \left.\frac{\partial \mathbf{z}}{\partial x}\right|_{x=0} = \left.\frac{\partial \mathbf{z}}{\partial x}\right|_{x=\ell}. \tag{3.3}$$

The choice of these boundary conditions enables a direct comparison of reduction methods developed for spatially homogeneous systems to those that include diffusion. More general boundary conditions could be studied at the expense of introducing additional thin layers into the solution, which would complicate the analysis.

We approximate a solution to Eqs. (3.1–3.2) by using separation of variables coupled with the method of weighted residuals. The dependent variables, $\mathbf{z}$, are approximated by a series of the product of time-dependent amplitudes, $\boldsymbol{\zeta}_m(t)$, and a set of spatial basis functions, $\phi_m(x)$:

$$\mathbf{z}(x,t) \approx \tilde{\mathbf{z}}_M(x,t) = \sum_{m=0}^{M} \boldsymbol{\zeta}_m(t)\phi_m(x), \tag{3.4}$$

where M is the number of terms in the approximation.

If we consider a simple model for diffusive flux, we can choose the basis functions to be the eigenfunctions of the diffusion operator,

$$\mathscr{L}_x(\phi_m) = \mu_m \phi_m, \text{ for } m = 0, \ldots, M, \tag{3.5}$$

where the eigenvalues, μ_m, are guaranteed to be non-negative and real, and the eigenfunctions orthogonal,

$$\langle \phi_m(x), \phi_n(x) \rangle \begin{cases} = 0, & \text{for } m \neq n, \\ \neq 0, & \text{for } m = n. \end{cases} \tag{3.6}$$

We require the eigenfunctions to match the boundary conditions of Eq. (3.2), yielding

$$\left.\frac{d\phi_m}{dx}\right|_{x=0} = \left.\frac{d\phi_m}{dx}\right|_{x=\ell} = 0, \tag{3.7}$$

or the boundary conditions of Eq. (3.3), yielding

$$\phi_m(0) = \phi_m(\ell) \text{ and } \left.\frac{d\phi_m}{dx}\right|_{x=0} = \left.\frac{d\phi_m}{dx}\right|_{x=\ell} \text{ for } x \in [0, \ell). \tag{3.8}$$

Our choice of boundary conditions allow for spatially homogeneous basis functions; We choose ϕ_0 to be the spatially homogeneous basis function whose eigenvalue is zero, $\mu_0 = 0$.

When the approximation from Eq. (3.4) is substituted into the form from Eq. (3.1), the result does not satisfy the equation exactly, but will have a non-zero residual,

$$\mathbf{r}(x,t) = \sum_{m=0}^{M} \frac{d\boldsymbol{\zeta}_m}{dt}\phi_m(x) - \mathbf{f}\left(\sum_{\hat{m}=0}^{M} \boldsymbol{\zeta}_{\hat{m}}(t)\phi_{\hat{m}}(x)\right) + \sum_{m=0}^{M} \mu_m \boldsymbol{\zeta}_m(t)\phi_m(x), \tag{3.9}$$

when M is finite. This residual is not the error, $\mathbf{e}(x,t) = \mathbf{z}(x,t) - \sum_{m=0}^{M} \boldsymbol{\zeta}_m(t)\phi_m(x)$; however, if the residual is zero, the error will be zero as well. To formulate evolution equations for the amplitudes, we take a series of M spatially weighted averages of the residual and require each be zero,

$$\langle \mathbf{r}(x,t), \psi_m(x) \rangle = 0, \text{ for all } m = 0, \ldots, M \text{ and } t \in [0, \infty), \tag{3.10}$$

where $\psi_m(x)$ is a set of M spatial weighting functions. There are many viable choices for weighting functions. If we make the common [6, 7] choice of the basis functions as the weighting functions, $\psi_m(x) = \phi_m(x)$, our method is a Galerkin

method. Substituting Eq. (3.9) (with dummy indices changed from m to n) into Eq. (3.10) and distributing the inner product linear operator to each term in the residual yields

$$\left\langle \sum_{n=0}^{M} \frac{d\boldsymbol{\zeta}_n}{dt}\phi_n(x), \phi_m(x) \right\rangle - \left\langle \mathbf{f}\left(\sum_{\hat{m}=0}^{M} \boldsymbol{\zeta}_{\hat{m}}(t)\phi_{\hat{m}}(x) \right), \phi_m(x) \right\rangle + \left\langle \sum_{n=0}^{M} \mu_n \boldsymbol{\zeta}_n(t)\phi_n(x), \phi_m(x) \right\rangle = 0. \quad (3.11)$$

Further simplification removes spatially independent terms from the inner products and arranges the terms in the order they were in Eq. (3.1),

$$\sum_{n=0}^{M} \frac{d\boldsymbol{\zeta}_n}{dt}\langle \phi_n(x), \phi_m(x) \rangle = \left\langle \mathbf{f}\left(\sum_{\hat{m}=0}^{M} \boldsymbol{\zeta}_{\hat{m}}(t)\phi_{\hat{m}}(x) \right), \phi_m(x) \right\rangle - \sum_{n=0}^{M} \mu_n \boldsymbol{\zeta}_n(t)\langle \phi_n(x), \phi_m(x) \rangle. \quad (3.12)$$

Because of the orthogonality of our basis functions, Eq. (3.12) can be reformulated to express the evolution of the amplitudes as

$$\frac{d\boldsymbol{\zeta}_m}{dt} = \frac{\left\langle \mathbf{f}\left(\sum_{\hat{m}=0}^{M} \boldsymbol{\zeta}_{\hat{m}}(t)\phi_{\hat{m}}(x) \right), \phi_m(x) \right\rangle}{\langle \phi_m(x), \phi_m(x) \rangle} - \mu_m \boldsymbol{\zeta}_m(t), \text{ for } m = 0, \ldots, M, \quad (3.13)$$

which yields a system of $R(M+1)$ ODEs. We define the reactions' contribution to the amplitude evolution as

$$\dot{\boldsymbol{\Omega}}_m(\boldsymbol{\zeta}_{\hat{m}}) = \frac{\left\langle \mathbf{f}\left(\sum_{\hat{m}=0}^{M} \boldsymbol{\zeta}_{\hat{m}}(t)\phi_{\hat{m}}(x) \right), \phi_m(x) \right\rangle}{\langle \phi_m(x), \phi_m(x) \rangle}. \quad (3.14)$$

To obtain the exact solution of Eq. (3.1), the residual must be driven to zero,

which requires the limit of $M \to \infty$. In this sense, the PDE of Eq. (3.1) can be considered to be an infinite set of ODEs. While the exact solution to an infinite-dimensional system is intractable, approximations with finite M project the trajectories of solutions to the infinite-dimensional system onto a finite-dimensional AIM [6]. The dynamics on this finite-dimensional approximation are governed by a system of ODEs,

$$\frac{d\boldsymbol{\zeta}_m}{dt} = \dot{\boldsymbol{\Omega}}_m(\boldsymbol{\zeta}_{\hat{m}}) - \mu_m \boldsymbol{\zeta}_m, \text{ for } m, \hat{m} = 0, \ldots, M. \tag{3.15}$$

Robinson [6, p. 387] shows that this AIM exponentially attracts all of the trajectories of solutions to the PDE of Eq. (3.1). Note that we choose not to employ slaving rules. Our approximate solutions are obtained by integrating this finite-dimensional system of ODEs to obtain the amplitude evolution, and then employing Eq. (3.4) to reconstruct an approximation of $\mathbf{z}(x,t)$. The evolution of amplitudes in Eq. (3.15) is forced by a nonlinear function, $\mathbf{F}_m(\boldsymbol{\zeta}_{\hat{m}}) = \dot{\boldsymbol{\Omega}}_m(\boldsymbol{\zeta}_{\hat{m}}) - \mu_m \boldsymbol{\zeta}_m(t)$, for $m, \hat{m} = 0, \ldots, M$. The projection of the function $\mathbf{f}(\mathbf{z})$ onto the AIM, $\dot{\boldsymbol{\Omega}}_m(\boldsymbol{\zeta}_{\hat{m}})$, represents the rate of change of each amplitude due to reaction, and the projection of $\mathscr{L}_x(\mathbf{z})$ onto the AIM, $\mu_m \boldsymbol{\zeta}_m(t)$, represents the contribution from diffusion.

In the case where the Galerkin projection is truncated at $M = 0$, the spatially homogeneous case is recovered, and Eq. (3.15) reduces to

$$\frac{d\boldsymbol{\zeta}_0}{dt} = \dot{\boldsymbol{\Omega}}_0(\boldsymbol{\zeta}_0). \tag{3.16}$$

If our spatially homogeneous basis function is unity, $\phi_0 = 1$, then Eq. (3.16) is

identical to the spatially homogeneous system in the original variables,

$$\frac{d\mathbf{z}}{dt} = \mathbf{f}(\mathbf{z}). \tag{3.17}$$

Since many manifold methods, including the SIM, focus on the spatially homogeneous system, we consider this case for comparison. Since spatially homogeneous dynamics are present in a subspace of all truncations of this Galerkin projection, we can use the results from the higher order truncations to identify deviations from the slow dynamics of the spatially homogeneous approximation.

3.1.1 Governing equations

We now specialize Eqs. (3.1–3.2) to consider isothermal, isochoric, reaction-diffusion systems of ideal gases which are described by Dalton's law and detailed mass-action Arrhenius kinetics. Our system consists of N species composed of L elements interacting in J reactions. We model spatial dynamics using Fick's law of diffusion with a constant mass diffusivity and neglect advection.

The governing equations for our reaction-diffusion system are the species evolution equations,

$$\rho\frac{\partial Y_i}{\partial t} = \bar{\mathsf{M}}_i\dot{\omega}_i + \frac{\dot{m}}{V}(Y_i^f - Y_i) - \frac{\partial j_i}{\partial x}, \text{ for } i = 1, \ldots, N, \tag{3.18}$$

where Y_i, Y_i^f, j_i, $\dot{\omega}_i$, and $\bar{\mathsf{M}}_i$, are mass fraction, feed flow mass fraction, diffusive mass flux, molar production rate, and molecular mass of species i, respectively; $\dot{m}$ is the mass feed flow rate, V is the volume of the tank, and ρ is the mixture density. By demanding that the initial conditions have the same elemental composition as the feed flow conditions, stoichiometric constraints can be exactly applied, and

the density will remain constant for this isothermal, isochoric, open system.

In addition to considering open systems in Eq. (3.18), we will also consider the case where the system is closed, $\dot{m} = 0$:

$$\rho \frac{\partial Y_i}{\partial t} = \bar{\mathsf{M}}_i \dot{\omega}_i - \frac{\partial j_i}{\partial x}, \text{ for } i = 1, \ldots, N. \tag{3.19}$$

We allow the initial conditions for each species to have spatial variations,

$$Y_i(x, t = 0) = Y_i^*(x), \text{ for } i = 1, \ldots, N, \tag{3.20}$$

and we model both sets of boundary conditions considered: homogeneous Neumann boundary conditions,

$$\left.\frac{\partial Y_i}{\partial x}\right|_{x=0} = \left.\frac{\partial Y_i}{\partial x}\right|_{x=\ell} = 0, \text{ for } i = 1, \ldots, N, \tag{3.21}$$

and periodic boundary conditions,

$$Y_i(0) = Y_i(\ell) \text{ and } \left.\frac{\partial Y_i}{\partial x}\right|_{x=0} = \left.\frac{\partial Y_i}{\partial x}\right|_{x=\ell}, \text{ for } i = 1, \ldots, N. \tag{3.22}$$

We consider a general set of J reactions with N species, χ_i, $i = 1, \ldots, N$,

$$\sum_{i=1}^{N} \nu'_{ij} \chi_i \leftrightharpoons \sum_{i=1}^{N} \nu''_{ij} \chi_i, \tag{3.23}$$

where $j = 1, \ldots, J$. The forward and reverse stoichiometric coefficients, ν'_{ij} and ν''_{ij}, are combined to a single net stoichiometric coefficient,

$$\nu_{ij} = \nu''_{ij} - \nu'_{ij}, \tag{3.24}$$

such that each reaction can be represented as

$$\sum_{i=1}^{N} \chi_i \nu_{ij} = 0, \text{ for all } j = 1, \ldots, J. \tag{3.25}$$

Note that ν_{ij} has dimension $N \times J$ and rank R, where $R \leq N - L$. Stoichiometric constraints, which require elements to be conserved in each reaction, can be written as

$$\sum_{i=1}^{N} \varphi_{li} \nu_{ij} = 0, \text{ for } l = 1, \ldots, L \text{ and } j = 1, \ldots, J, \tag{3.26}$$

where φ_{li} is the number of elements, l, in species i; this constrains ν_{ij} to be in the right null space of φ_{li}.

We sum Eq. (3.18) over all species,

$$\sum_{i=1}^{N} \rho \frac{\partial Y_i}{\partial t} = \sum_{i=1}^{N} \bar{\mathsf{M}}_i \dot{\omega}_i + \sum_{i=1}^{N} \frac{\dot{m}}{V}(Y_i^f - Y_i) - \sum_{i=1}^{N} \frac{\partial j_i}{\partial x}. \tag{3.27}$$

Since $\sum_{i=1}^{N} Y_i = 1$, which does not change over time, the left hand side of Eq. (3.27) and the feed flow terms are both zero. The reaction source term also sums to zero because of stoichiometric constraints; therefore, we demand a choice of mass flux whose spatial derivative sums to zero, $\sum_{i=1}^{N} \partial j_i / \partial x = 0$, to have a consistent system.

3.1.2 Constitutive equations

To complete the system, the following constitutive equations are specified. The mass flux is given by Fick's law of diffusion,

$$j_i = -\rho \sum_{\hat{i}=1}^{N} \mathcal{D}_{i\hat{i}} \frac{\partial Y_{\hat{i}}}{\partial x}, \text{ for } i = 1, \ldots, N, \tag{3.28}$$

where $\mathcal{D}_{i\hat{i}}$ are the mass diffusivities, which are assumed to be constant. We are primarily concerned with systems which model all species with identical mass diffusivities, in which case $\mathcal{D}_{ii} = \mathcal{D}$ for $i = 1, \ldots, N$ and $\mathcal{D}_{i\hat{i}} = 0$ for $i \neq \hat{i}$. However, when we consider unequal species mass diffusivities, we assume $\mathcal{D}_{ii} = \mathcal{D}_i$ for $i = 1, \ldots, N-1$; we use the algebraic constraint, $\sum_{i=1}^{N} Y_i = 1$, to solve for the Nth species and need not consider its complicated diffusivity. More details are provided in Buckmaster and Ludford [21, pp. 7–8].

The spatial gradient of mass flux in Eq. (3.28) is a self-adjoint, positive semi-definite, linear differential operator which is in the form of $\mathscr{L}_x$ from Eq. (3.15). As a result of Eq. (3.28), along with our chosen boundary conditions (either homogeneous Neumann or periodic), there is no net mass flux out of the domain. The pressure, P, is given by the ideal gas equation of state for a mixture that obeys Dalton's law:

$$P = \rho \bar{\mathfrak{R}} T \sum_{i=1}^{N} \frac{Y_i}{\bar{\mathsf{M}}_i}, \tag{3.29}$$

where $\bar{\mathfrak{R}} = 8.314 \times 10^7 \ erg/(mol\ K)$ is the universal gas constant, and T is the constant temperature. The reaction source terms, $\dot{\omega}_i$, are given by detailed mass-action Arrhenius kinetics:

$$\dot{\omega}_i = \sum_{j=1}^{J} \nu_{ij} r_j, \text{ for } i = 1, \ldots, N, \tag{3.30a}$$

$$r_j = k_j \left(\prod_{i=1}^{N} \left(\frac{\rho Y_i}{\bar{\mathsf{M}}_i} \right)^{\nu'_{ij}} - \frac{1}{K_j^c} \prod_{i=1}^{N} \left(\frac{\rho Y_i}{\bar{\mathsf{M}}_i} \right)^{\nu''_{ij}} \right), \text{ for } j = 1, \ldots, J, \tag{3.30b}$$

$$k_j = a_j T^{\beta_j} \exp\left(\frac{-\bar{E}_j}{\bar{\mathfrak{R}} T} \right), \text{ for } j = 1, \ldots, J, \tag{3.30c}$$

$$K_j^c = \left(\frac{P^o}{\bar{\mathfrak{R}} T} \right)^{\sum_{i=1}^{N} \nu_{ij}} \exp\left(\frac{-\sum_{i=1}^{N} \bar{\mu}_i^o \nu_{ij}}{\bar{\mathfrak{R}} T} \right), \text{ for } j = 1, \ldots, J, \tag{3.30d}$$

$$\bar{\mu}_i^o = \bar{\mathsf{M}}_i (h_i - T s_i^o), \text{ for } i = 1, \ldots, N, \tag{3.30e}$$

where r_j, k_j, and K_j^c are the reaction rate, Arrhenius rate, and equilibrium constant of reaction j, respectively, and $\bar{\mu}_i^o$ is the chemical potential of species i evaluated at the reference pressure, P^o. The Arrhenius rate depends on the collision frequency factor, a_j, the temperature-dependency exponent, β_j, and the activation energy, $\bar{E}_j$; the equilibrium constant depends on the reference pressure and chemical potentials; and the chemical potential depends on specific enthalpy, h_i, and the specific entropy evaluated at the reference pressure, s_i^o. Equations (3.18–3.21) and (3.28–3.30) form a complete set.

3.1.3 Model reduction

In this section a series of reductions to Eqs. (3.18–3.21) and (3.28–3.30) will be described in detail.

3.1.3.1 Generalized Shvab-Zel'dovich relations

First, we implement a reduction technique using the generalized Shvab-Zel'dovich relations similar to the reduction found in Lam and Bellan [101]. Similar to Eq. (3.26), we use a modified species-element matrix, $\hat{\varphi}_{li}$, that spans the left null space of matrix ν_{ij},

$$\sum_{i=1}^{N} \hat{\varphi}_{li}\nu_{ij} = 0, \text{ for } l = 1, \ldots, \hat{L} \text{ and } j = 1, \ldots, J, \tag{3.31}$$

to replace $\hat{L}$ differential equations with algebraic constraints. We note that $\hat{L} = N - R$ because of the dimension and rank of ν_{ij}. This reduction allows algebraic constraints to couple the evolution of $\hat{L}$ species to a reduced set of R species. Note that $\hat{L} \geq L$ is the total number of linear constraints for the reaction mechanism,

which includes all L stoichiometric constraints, as well as any others. Operating on the molar production rates, Eq. (3.30a), with $\hat{\varphi}_{li}$, and summing over all species, i, we get

$$\sum_{i=1}^{N} \hat{\varphi}_{li}\dot{\omega}_i = \sum_{i=1}^{N} \hat{\varphi}_{li} \sum_{j=1}^{J} \nu_{ij} r_j = \sum_{j=1}^{J} r_j \sum_{i=1}^{N} \hat{\varphi}_{li}\nu_{ij} = 0, \text{ for } l = 1, \ldots, \hat{L}. \tag{3.32}$$

We apply the operator $\hat{\varphi}_{li}$ to Eq. (3.18), use the diffusive mass flux from Eq. (3.28), and sum over all species to obtain

$$\frac{\partial}{\partial t}\left(\sum_{i=1}^{N} \hat{\varphi}_{li}\frac{Y_i}{\bar{\mathsf{M}}_i}\right) - \mathcal{D}\frac{\partial^2}{\partial x^2}\left(\sum_{i=1}^{N} \hat{\varphi}_{li}\frac{Y_i}{\bar{\mathsf{M}}_i}\right) = \sum_{i=1}^{N} \hat{\varphi}_{li}\dot{\omega}_i = 0, \text{ for } l = 1, \ldots, \hat{L}. \tag{3.33}$$

We now restrict our evaluation to systems whose initial conditions are spatially homogeneous in the values $\sum_{i=1}^{N} \hat{\varphi}_{li} Y_i/\bar{\mathsf{M}}_i$, for $l = 1, \ldots, \hat{L}$, which implies the initial element distribution is spatially homogeneous, as would typically be found in premixed combustion. Since the homogeneous Neumann boundary conditions yield no perturbations in the spatial distributions of these linear combinations of species, Eq. (3.33) can be integrated to yield

$$\sum_{i=1}^{N} \hat{\varphi}_{li}\frac{Y_i}{\bar{\mathsf{M}}_i} = \sum_{i=1}^{N} \hat{\varphi}_{li}\frac{Y_i^*}{\bar{\mathsf{M}}_i}, \text{ for } l = 1, \ldots, \hat{L}; \tag{3.34}$$

therefore, these linear combinations of species will remain spatially homogeneous for all time. Note that, similar to premixed combustion, individual species are not required to be spatially homogeneous; only the distribution of the linear constraints (i.e. elements) given in Eq. (3.34) has this requirement. The set of $\hat{L}$ algebraic relations implies that we need not solve for the dynamics of all N species. Instead, we focus our attention on $R = N - \hat{L}$ reduced species, then use Eq. (3.34)

to determine the dynamics of the remaining species.

3.1.3.2 Transformation to reduced variables

Following Ren et al. [64] and Al-Khateeb et al. [49], we now transform the mass fractions into specific mole concentrations, $\hat{z}_i$, where

$$\hat{z}_i \equiv \frac{Y_i}{\mathsf{M}_i}, \text{ for } i = 1, \ldots, N. \tag{3.35}$$

We can use the constraints in Eq. (3.34) to obtain a set of reduced variables. We choose the first R linearly independent species as our reduced variables, z_n, $n = 1, \ldots, R$, and then couple the values of $\hat{z}_i$ for $i = 1, \ldots, N$ to those reduced variables by the linear relation

$$\hat{z}_i(x,t) = \mathsf{z}_i + \sum_{n=1}^{R} \mathfrak{D}_{in} z_n(x,t), \text{ for } i = 1, \ldots, N. \tag{3.36}$$

Here, z_n are the R reduced specific mole concentrations, z_i are the values of specific mole concentration when $z_n = 0\ mol/g$ for all $n = 1, \ldots, R$, and $\mathfrak{D}_{in}$ is a coefficient matrix of dimension $N \times R$ that couples the variations in z_n to $\hat{z}_i$. We define $\mathfrak{D}_{in}$ to be an $N \times R$ full rank matrix that spans the column space of ν_{ij}, $\sum_{i=1}^{N} \hat{\varphi}_{li} \mathfrak{D}_{in} = 0$ for $l = 1, \ldots, \hat{L}$ and $n = 1, \ldots, R$. This reduction is not unique. The following is a technique to obtain $\mathfrak{D}_{in}$: reduce the transpose of ν_{ij} to a row-echelon form, truncate the final $J - R$ rows of zeros in this echelon form, and take the transpose of this truncation to form $\mathfrak{D}_{in}$. In this construction of $\mathfrak{D}_{in}$, the first R rows form a sub-matrix which is an $R \times R$ identity matrix; this fact, along with the choice

of $\mathsf{z}_i = 0\ mol/g$ for $i = 1, \ldots, R$, renders

$$z_i = \hat{z}_i, \text{ for } i = 1, \ldots, R. \tag{3.37}$$

This leaves the initial and boundary conditions in the reduced variables as

$$z_i^* = \frac{Y_i^*}{\mathsf{M}_i}, \text{ for } i = 1, \ldots, R, \tag{3.38}$$

and

$$\left.\frac{\partial z_i}{\partial x}\right|_{x=0} = \left.\frac{\partial z_i}{\partial x}\right|_{x=\ell} = 0, \text{ for } i = 1, \ldots, R. \tag{3.39}$$

The remaining $\mathsf{z}_i,\ i = R+1, \ldots, N$, are chosen to satisfy the $\hat{L}$ algebraic constraints, Eq. (3.34), which are simplified to

$$\sum_{i=1}^{N} \hat{\varphi}_{li} \left(\mathsf{z}_i + \sum_{n=1}^{R} \mathfrak{D}_{in} z_n \right) = \sum_{i=1}^{N} \hat{\varphi}_{li} z_i^*, \text{ for } l = 1, \ldots, \hat{L}, \tag{3.40}$$

and have the solution,

$$\mathsf{z}_i = z_i^* - \sum_{n=1}^{R} \mathfrak{D}_{in} z_n^*, \text{ for } i = R+1, \ldots, N. \tag{3.41}$$

Substituting specific mole concentrations, Eq. (3.35), along with the constitutive equation for mass flux, Eq. (3.28), into Eq. (3.18) yields N evolution equations for $\hat{z}_i,\ i = 1, \ldots, N$, where only the first R equations are linearly independent. Therefore, we only consider the evolution equations for the reduced variables,

$$\frac{\partial z_i}{\partial t} = \frac{\dot{\omega}_i(z_n)}{\rho} + \mathcal{D}\frac{\partial^2 z_i}{\partial x^2}, \text{ for } i, n = 1, \ldots, R, \tag{3.42}$$

where we define a scaled chemical source term, $f_i(z_n) = \dot{\omega}_i(z_n)/\rho$, and diffusive

flux term, $\mathscr{L}_x(z_i) = -\mathcal{D}\ \partial^2 z_i/\partial x^2$, so Eq. (3.42) is in identical form to Eq. (3.1).

3.1.3.3 Galerkin reduction to ODEs

To analyze Eq. (3.42), we apply a Galerkin projection onto an AIM [6]. We accomplish this by assuming the reduced variables are approximated in the form of Eq. (3.4),

$$z_i(x,t) \approx \sum_{m=0}^{M} \zeta_{i,m}(t)\phi_m(x), \text{ for } i = 1,\ldots,R, \tag{3.43}$$

where $\phi_m(x)$ are chosen as basis functions and $\zeta_{i,m}(t)$ are the corresponding time-dependent amplitudes of species i. For a given domain length, we choose the truncation of our approximation by setting M to a value above which the amplitude evolution is dominated by diffusion; diffusion causes the amplitudes, $\zeta_{i,m}$ for all i and $m > M$, to decay rapidly before substantial reaction dynamics occur.

We choose basis functions that are the eigenfunctions of the diffusion operator that match the boundary conditions. For the remainder of the analysis we consider the homogeneous Neumann boundary conditions with eigenfunctions, $\phi_m = \cos(m\pi x/\ell)$. Appendix A gives details of the analogous analysis for periodic boundary conditions. The series of cosines is a complete orthogonal basis in the limit as $M \to \infty$, and the corresponding eigenvalues are non-negative and real, $\mu_m = \mathcal{D}m^2\pi^2/\ell^2$. Our solution is decomposed into a Fourier cosine series whose $m = 0$ amplitudes model the spatially homogeneous components and $m > 0$ amplitudes model the spatial variations. By substituting Eq. (3.43) into Eq. (3.42) and taking the inner product with each basis function, $\phi_n(x)$, we obtain a finite system of ODEs for the evolution of the amplitudes in the form of Eq. (3.13). Since our molar production rates are low-order polynomials and our basis functions are cosines, the integration of the $\dot{\Omega}_m(\zeta_{\hat{m}})$ terms in Eq. (3.14) can be performed ana-

lytically using trigonometric identities, as shown in Appendix B. We can therefore focus on the evaluation of our finite-dimensional system in the form of Eq. (3.15),

$$\frac{d\zeta_{i,m}}{dt} = \dot{\Omega}_{i,m}(\zeta_{j,n}) - \frac{\mathcal{D}m^2\pi^2}{\ell^2}\zeta_{i,m}, \text{ for } i,j = 1,\ldots,R \text{ and } m,n = 0,\ldots,M. \quad (3.44)$$

The initial conditions of the reduced species amplitudes are given by

$$\zeta_{i,m}(0) = \frac{\langle \phi_m, z_i^* \rangle}{\langle \phi_m, \phi_m \rangle}, \text{ for } i = 1,\ldots,R \text{ and } m = 0,\ldots,M. \quad (3.45)$$

For very small ℓ, a truncation at $M = 0$ is appropriate, in which case Eqs. (3.44) and (3.45) reduce to a spatially homogeneous system in the form of Eq. (3.17),

$$\frac{dz_i}{dt} = f_i(z_n), \text{ for } i,n = 1,\ldots,R, \quad (3.46)$$

$$z_i(0) = z_i^*, \qquad \text{for } i = 1,\ldots,R. \quad (3.47)$$

For this to be the case, ℓ must be sufficiently small such that the diffusion term, $\mathcal{D}m^2\pi^2/\ell^2$, will dominate the evolution equation for $m \geq 1$. At this small length scale, diffusion alone will cause all spatial inhomogeneities to equilibrate quickly, and the remaining reaction dynamics can be accurately modeled as the spatially homogeneous system given in Eqs. (3.46–3.47).

3.2 SIM construction for reaction-diffusion systems

In this section we describe our extension of SIM construction from spatially homogeneous systems to reaction-diffusion systems and describe some of the ramifications of our approach. The approach we take to SIM construction is an extension of the spatially homogeneous technique given by Davis and Skodje [5]

and Al-Khateeb et al. [49]. This technique requires the construction of individual branches of the one-dimensional SIM by integrating a heteroclinic orbit from a non-physical saddle equilibrium, along its only unstable eigenvector, to the physical equilibrium sink, which the SIM approaches along the equilibrium's slowest eigenvector. We label the non-physical saddle equilibrium from which a SIM branch emanates the SIM Branch Initial Condition (SIM-BIC). The evaluation of the entire dynamical system, including the equilibria with negative concentrations and other non-physical mathematical artifacts, provides useful insights into the physical dynamics, as shown by Davis and Skodje [5] and Al-Khateeb et al. [49].

This technique is extended to the infinite-dimensional PDEs governing a reaction-diffusion equation by use of the Galerkin projection onto an AIM, as described in Section 3.1.3.3. This AIM is an $R(M+1)$-dimensional system of ODEs, whose equilibria are amenable to a similar SIM construction technique as used for the spatially homogeneous system of ODEs. While the SIM is invariant for the governing ODEs in each Galerkin projection, it only approximates an invariant manifold for the governing PDEs. The SIM will converge to an invariant manifold for the governing PDEs in the limit as $M \to \infty$. Here we make a distinction between our terminology of equilibrium and chemical equilibrium. What we call an equilibrium is a fixed point in our finite-dimensional projection of an infinite-dimensional dynamical system which is the steady state solution to Eq. (3.1),

$$\mathbf{f}(\mathbf{z}^e) - \mathscr{L}_x(\mathbf{z}^e) = \mathbf{0}, \tag{3.48}$$

not necessarily the chemical equilibrium. This solution, or equilibrium manifold, is a spatial function, $\mathbf{z}^e(x)$, which can be approximated by the steady state solution

of the Galerkin projection in Eq. (3.15),

$$\mathbf{F}_m(\boldsymbol{\zeta}^e_{\hat{m}}) = \dot{\boldsymbol{\Omega}}_m(\boldsymbol{\zeta}^e_{\hat{m}}) - \mu_m \boldsymbol{\zeta}^e_m = \mathbf{0}, \text{ for } m, \hat{m} = 0, \ldots, M. \tag{3.49}$$

The solution to Eq. (3.49) is a fixed point in the finite-dimensional phase space which can be reconstructed into the approximation $\tilde{\mathbf{z}}^e_M(x)$ using Eq. (3.4). In the $M = 0$ truncation, the spatially homogeneous reaction-only equilibria are recovered,

$$\mathbf{f}(\mathbf{z}^{e:SH}) = \mathbf{0}. \tag{3.50}$$

The concentrations of one of these spatially homogeneous equilibria are equal to their chemical equilibrium values.

The spatially homogeneous equilibria, $\mathbf{z}^{e:SH}$, which satisfy the steady state $M = 0$ Galerkin projection, Eq. (3.50), will have no contribution from the diffusion operator $\mathscr{L}_x(\mathbf{z}^{e:SH}) = \mathbf{0}$, and will also satisfy the full steady state equation, Eq. (3.48). The spatially homogeneous equilibria are also exact steady state solutions to any Galerkin projection, where $\boldsymbol{\zeta}_0 = \mathbf{z}^{e:SH}$ and $\boldsymbol{\zeta}_m = \mathbf{0}$ for $m > 0$. Furthermore, all spatially homogeneous dynamics of the $M > 0$ Galerkin projections occur in a subspace of these larger AIMs; when $\zeta_{i,m} = 0$ for all i and for $m > 0$, all dynamics occur on the $M = 0$ AIM, which we call the spatially homogeneous subspace.

We seek additional equilibria to the steady state Galerkin projection, Eq. (3.49). Since the reaction-diffusion AIM projection has a higher dimension than the spatially homogeneous system, its Jacobian has additional eigenvalues. We analytically examine the additional eigenvalues at an arbitrary point in the spatially homogeneous subspace, focusing first on the spatially homogeneous equilibria. From

local linear analysis of the spatially homogeneous system, we find a reaction-only Jacobian matrix, defined as

$$J_{ij} = \frac{\partial f_i}{\partial z_j}, \text{ for } i, j = 1, \ldots, R. \tag{3.51}$$

This Jacobian has R eigenvalues, $\lambda_{i,0},\ i = 1, \ldots, R$, which we sort from largest to smallest by their real parts ($\mathrm{Re}(\lambda_{i,0}) \geq \mathrm{Re}(\lambda_{i+1,0})$ for $i = 1, \ldots, R-1$). By defining the local chemical time scales as the reciprocal of the eigenvalues,

$$\tau_{i,0} = \frac{1}{|\lambda_{i,0}|}, \text{ for } i = 1, \ldots, R, \tag{3.52}$$

we see that when all eigenvalues have negative real parts (as they do in the neighborhood of the physical equilibrium), this ordering becomes slowest (at $i = 1$) to fastest (at $i = R$). Local linear analysis of any point in the spatially homogeneous subspace in $M > 0$ truncations of the Galerkin projection, Eq. (3.44), yields a Jacobian matrix that is of block diagonal form

$$\mathbf{J}_{\mathrm{AIM}} = \begin{bmatrix} \mathbf{J} & \mathbf{0} & \ldots & \mathbf{0} & \ldots & \mathbf{0} \\ \mathbf{0} & \mathbf{J} - \mu_1 \mathbf{I} & \ldots & \mathbf{0} & \ldots & \mathbf{0} \\ \vdots & \vdots & \ddots & \vdots & & \vdots \\ \mathbf{0} & \mathbf{0} & \ldots & \mathbf{J} - \mu_m \mathbf{I} & \ldots & \mathbf{0} \\ \vdots & \vdots & & \vdots & \ddots & \vdots \\ \mathbf{0} & \mathbf{0} & \ldots & \mathbf{0} & \ldots & \mathbf{J} - \mu_M \mathbf{I} \end{bmatrix}, \tag{3.53}$$

as seen from the derivation in Appendix C, where $\mathbf{J}$ is the reaction-only Jacobian matrix evaluated at the spatially homogeneous concentrations, and $\mathbf{I}$ and $\mathbf{0}$ are identity and zero $R \times R$ square matrices, respectively.

The eigenvalues of this block diagonal Jacobian matrix are correlated to the R reaction-only eigenvalues of $\mathbf{J}$ and are given by

$$\lambda_{i,m} = \lambda_{i,0} - \mu_m, \text{ for } i = 1, \ldots, R \text{ and } m = 0, \ldots, M. \tag{3.54}$$

We label these the diffusion-modified eigenvalues for $m \geq 1$. Using the same definition of local time scales as in the spatially homogeneous case, we find

$$\tau_{i,m} = \left|\lambda_{i,0} - \mu_m\right|^{-1}, \text{ for } i = 1, \ldots, R \text{ and } m = 0, \ldots, M, \tag{3.55}$$

where we see that these diffusion-modified time scales have a contribution from reaction, $\lambda_{i,0}$, and a contribution from diffusion, μ_m; therefore, we define a diffusion time scale for each spatially inhomogeneous Fourier mode:

$$\tau_{\mathcal{D},m} = \frac{1}{\mu_m}, \text{ for } m = 1, \ldots, M. \tag{3.56}$$

Since the diffusion contribution to the modified eigenvalues is always negative, the addition of diffusion provides a stabilizing effect (the eigenvalues become more negative). For equilibria with positive chemical eigenvalues, $\lambda_{i,0} > 0$, Eq. (3.54) identifies critical length scales where the diffusion-modified eigenvalue will be zero. This can be seen by substituting in the definition of μ_m into Eq. (3.55) and solving for the length scale that makes $\tau_{i,m} = 0$. For homogeneous Neumann boundary conditions, this critical length will be $\ell_c = m\pi\sqrt{\mathcal{D}\tau_{i,0}}$, where $\tau_{i,0}$ is substituted for $1/\lambda_{i,0}$ using Eq. (3.52) to show consistency with Al-Khateeb et al. [14], and others [15–17].

3.3 Phase shifts and symmetry

We note that our boundary conditions admit a phase shift for inhomogeneous solutions; periodic boundary conditions allow a continuous phase shift, while Neumann boundary conditions only allow solutions π radians out of phase. With our choice of basis functions, this phase shift appears as a symmetry in the amplitudes of the Galerkin projection. For example, the initial conditions of $z_i^*(x)$ that satisfy the homogeneous Neumann boundary conditions will have the solution evolution of $z_i(x,t)$ for all $i = 1, \ldots, R$. A symmetric initial condition, $z_i^*(\ell - x)$, will also satisfy the same boundary conditions and will have a symmetric evolution of $z_i(\ell - x, t)$ that satisfies the governing PDE. When projected into cosine basis functions, the amplitudes of $z_i(x,t)$ are $\zeta_{i,m}(t)$, while the amplitudes of $z_i(\ell - x, t)$ are $(-1)^m \zeta_{i,m}(t)$. This symmetry means that phase space will have a reflective symmetry about the spatially homogeneous subspace, $\zeta_{i,m}(t) = 0$ for all $i = 1, \ldots, R$ and $m = 1, \ldots, M$. We restrict our analysis to the half of phase space where $\zeta_{1,1}(t) \geq 0$, since the dynamics of the other half will be symmetric.

CHAPTER 4

CLOSED REACTION-DIFFUSION SYSTEMS

In this chapter we examine closed reaction-diffusion systems to identify and evaluate changes that occur in the SIM for these systems. We will examine two cases: i) a highly resolved 26-term truncation that takes into account one spatially homogeneous mode and 25 modes with various spatial wavelengths. This allows us to examine the accuracy of lower truncations and to identify underlying consistencies between our method and the continuum model; and ii) a two-term truncation that only includes the spatially homogeneous mode and the fundamental spatial mode. The advantage of this approach is that it is a low-dimensional, simple model that demonstrates the interesting dynamics of the interaction between reaction and diffusion; however, for large domain lengths, this truncation lacks spatial resolution.

This chapter examines three model problems with different chemical kinetic mechanisms, each coupled with a simple diffusion model. The first is a simple one-step kinetic mechanism, the second is a one-step oxygen dissociation reaction, and the third is the two-step Zel'dovich reaction mechanism of NO production. The third system's spatially homogeneous SIM was studied by Al-Khateeb et al. [49]. This chapter provides an extension of Ref. [49] to include the effects of diffusion.

4.1 Model problems

4.1.1 Simple chemical mechanism

We examine a simple problem with $R = 1$ in the form of Eq. (3.1), specifically

$$\frac{\partial z}{\partial t} = -K(z - C_1)(z - C_2) + \mathcal{D}\frac{\partial^2 z}{\partial x^2}, \tag{4.1}$$

with homogeneous Neumann boundary conditions consistent with Eq. (3.2),

$$\left.\frac{\partial z}{\partial x}\right|_{x=0} = \left.\frac{\partial z}{\partial x}\right|_{x=\ell} = 0. \tag{4.2}$$

In Eq. (4.1) we assume the parameters to be $K > 0$ and $C_1 < C_2$. We take $z^e(x)$ to be a steady solution to Eqs. (4.1–4.2) and evaluate its linear stability. We assume the initial conditions are perturbed from the steady state solution, $z(x, 0) = z^e(x) + \epsilon A(x, 0)$, where $A(x, 0)$ is $\mathcal{O}(1)$ and $0 < \epsilon \ll 1$, and evaluate the subsequent evolution of

$$z(x, t) = z^e(x) + \epsilon A(x, t). \tag{4.3}$$

When we substitute the solution from Eq. (4.3) into Eq. (4.1), collect the terms that are $\mathcal{O}(\epsilon)$, and assume a separation of variables, $A(x, t) = G(x)H(t)$, we obtain two linear ODEs,

$$\frac{dH}{dt} = \gamma H(t), \tag{4.4}$$

$$\frac{d^2G}{dx^2} = \left(\frac{\gamma + K(2z^e(x) - C_1 - C_2)}{\mathcal{D}}\right) G(x), \tag{4.5}$$

where γ is a constant. The solution to Eq. (4.4) is an exponential, $H(t) = H(0)\exp(\gamma t)$, where the sign of γ indicates the stability of the solution. The solution to Eq. (4.5) for a general steady state equilibrium, $z^e(x)$, typically requires numerical evaluation; however, if we evaluate spatially homogeneous equilibria, $z^e(x) = z^{e:SH}$, the solutions to Eq. (4.5) that match the boundary conditions are of the form,

$$G(x) = \cos\left(\sqrt{\frac{-\gamma - K(2z^{e:SH} - C_1 - C_2)}{\mathcal{D}}}x\right), \tag{4.6}$$

where the coefficient of x in the argument of the cosine function must be an integer multiple of π/ℓ. Therefore, we can solve for the stability parameter, γ, which yields the spectrum of values,

$$\gamma = -K(2z^{e:SH} - C_1 - C_2) - \frac{m^2\pi^2\mathcal{D}}{\ell^2}, \tag{4.7}$$

for any integer value of $m \geq 0$. Note that γ is composed of two terms: $\lambda_0 = -K(2z^{e:SH} - C_1 - C_2)$, which is the eigenvalue of the reaction-only system, and $-\mu_m^2\mathcal{D} = -m^2\pi^2\mathcal{D}/\ell^2$, which is the diffusion-modification term. Therefore, the linear stability analysis for a spatially homogeneous equilibrium is consistent with the Jacobian eigenvalue analysis in Section 3.2. We also find that for a spatially inhomogeneous solution, the eigenvalues of the Jacobian of the Galerkin projection are a good approximation of the stability parameter, γ.

By inspection, we find two finite spatially homogeneous steady state solutions to Eqs. (4.1–4.2), $z^{e:SH} = C_1$ and $z^{e:SH} = C_2$. There are other finite steady solutions which are spatially inhomogeneous; their composition and stability are dependent on the reaction parameters and the domain length, which will be illustrated in an upcoming example. The reaction-only eigenvalue of the spatially

homogeneous equilibrium, $z^{e:SH} = C_2$, is negative, $\lambda_0 = -K(C_2 - C_1) < 0$, and the diffusion-modification contribution is non-positive; therefore, all values of γ are negative, and $z^{e:SH} = C_2$ is stable. The equilibrium $z^{e:SH} = C_1$ has a positive reaction-only eigenvalue, $\lambda_0 = -K(C_1 - C_2) > 0$. Since the $m = 0$ mode has no diffusion contribution, γ for this mode will also be positive, and $z^{e:SH} = C_1$ will be unstable for at least one mode; however, there is an infinite spectrum of values for γ, so for any finite domain length, there will be modes where the negative diffusion contribution has stabilized the positive reaction contribution, resulting in a stable mode. The number of unstable modes depends on the domain length ℓ.

We now examine a simple reaction mechanism,

$$B + B \leftrightharpoons A + A, \tag{4.8}$$

with $N = 2$ species, $J = 1$ reaction, and $\hat{L} = 1$ constraint, which can be modeled by a system in the form of Eq. (4.1). By choosing $i = \{1, 2\}$ to correspond to the species $\{A, B\}$, respectively, the rate equation for this reaction is

$$r = k\left(\left(\frac{\rho Y_2}{\bar{\mathsf{M}}}\right)^2 - \frac{1}{K^c}\left(\frac{\rho Y_1}{\bar{\mathsf{M}}}\right)^2\right). \tag{4.9}$$

The mole fractions must sum to unity, $Y_1 + Y_2 = 1$, facilitating the reduction shown in Section 3.1.3. Since $R = N - \hat{L} = 1$, we choose to model the evolution of species A as the reduced variable $z = Y_1/\bar{\mathsf{M}}$, and algebraically solve for the evolution of B with the mole fraction constraint. This yields the evolution equation in the form of Eq. (3.42),

$$\frac{\partial z}{\partial t} = 2\rho k\left(\left(\frac{1}{\bar{\mathsf{M}}} - z\right)^2 - \frac{z^2}{K^c}\right) + \mathcal{D}\frac{\partial^2 z}{\partial x^2}. \tag{4.10}$$

We choose parameters to induce scales that are loosely correlated to those found in reactive gases at atmospheric pressure, $k = 2.5 \times 10^8\ cm^3/mol/s$, $\bar{\mathsf{M}} = 1\ g/mol$, $K^c = 0.25$, $\rho = 1 \times 10^{-3}\ g/cm^3$, and $\mathcal{D} = 1\ cm^2/s$. The resulting evolution equation is in the form of Eq. (4.1) with parameters $K = 2k\rho(1 - 1/K^c) = 1.5 \times 10^6\ g/mol/s$, $C_1 = \sqrt{K^c}/((\sqrt{K^c} - 1)\bar{\mathsf{M}}) = -1\ mol/g$, and $C_2 = \sqrt{K^c}/((\sqrt{K^c} + 1)\bar{\mathsf{M}}) = 1/3\ mol/g$:

$$\frac{\partial z}{\partial t} = -1.5 \times 10^6\,(z+1)\left(z - \frac{1}{3}\right) + \frac{\partial^2 z}{\partial x^2}. \tag{4.11}$$

This system has two finite spatially homogeneous equilibria,

$$z^{e:SH} = \left\{-1, \frac{1}{3}\right\}\ mol/g, \tag{4.12}$$

which we label R_1 and R_2, respectively. The reaction-only eigenvalues of the linearized system about these equilibria are $\lambda_0 = 2 \times 10^6\ s^{-1}$ at R_1 and $\lambda_0 = -2 \times 10^6\ s^{-1}$ at R_2. We know that R_2 is linearly stable since all of the values of γ from its linear stability analysis are negative, independent of domain length. This result for the stability, along with the fact that both species concentrations are positive, indicates that R_2 is the physical equilibrium. Evaluating R_1, we find that the $m = 0$ mode is unstable, but the sign of γ for larger values of m depends on the domain length.

In addition to evaluating the stability of the spatially inhomogeneous modes at R_1, we now find any additional spatially inhomogeneous steady solutions and evaluate their stability. The Galerkin projection admits an infinite number of steady solutions in the $M \to \infty$ limit. Most of these equilibria are complex and/or singular; we are only interested in the real non-singular steady state solutions. By

identifying all the roots with an algebraic analysis for a low order system ($M = 3$ Galerkin projection) and resolving these roots to a higher order system ($M = 25$) using Newton's method, we find that the number of real non-singular solutions increases as ℓ increases. We present the results for three different domain lengths: $\ell = 5\ \mu m$, $22.5\ \mu m$, and $100\ \mu m$.

For $\ell = 5\ \mu m$, the only steady state solutions we identify are the spatially homogeneous equilibria, R_1 and R_2; we find R_1 to have only one positive value of γ for $m = 0$, and it is therefore only unstable in the spatially homogeneous mode. For $\ell = 22.5\ \mu m$, we find that R_1 is unstable in two modes ($m = 0$ and $m = 1$); also, we identify two real non-singular spatially inhomogeneous steady solutions, which each have only one positive value of γ. For $\ell = 100\ \mu m$, R_1 has five unstable modes for $m = 0$ through $m = 4$. At this length we identify eight real non-singular spatially inhomogeneous steady solutions, all of which are unstable in some modes; two of these solutions have one positive value of γ, two have two, two have three, and two have four. The spatial reconstructions of the steady solutions in the $M = 25$ Galerkin approximation are shown in Figure 4.1 for $\ell = 22.5\ \mu m$ and for $\ell = 100\ \mu m$, where the value m in $\hat{R}_{1,m}$ indicates the number of unstable modes in the spatially inhomogeneous solutions. Some of the solutions for $\ell = 100\ \mu m$ with low values of m are quite similar and are therefore hard to discern in Figure 4.1; the spatially homogeneous R_2 at $z = 1/3\ mol/g$ (black) and one $\hat{R}_{1,2}$ (blue dash-dashed) are both nearly obscured by half of each $\hat{R}_{1,1}$ solution (red dashed), which cross at $x = 50\ \mu m$.

We see from these examples that for longer values of ℓ, more of the modes in the neighborhood of R_1 become unstable. These transitions from stable to

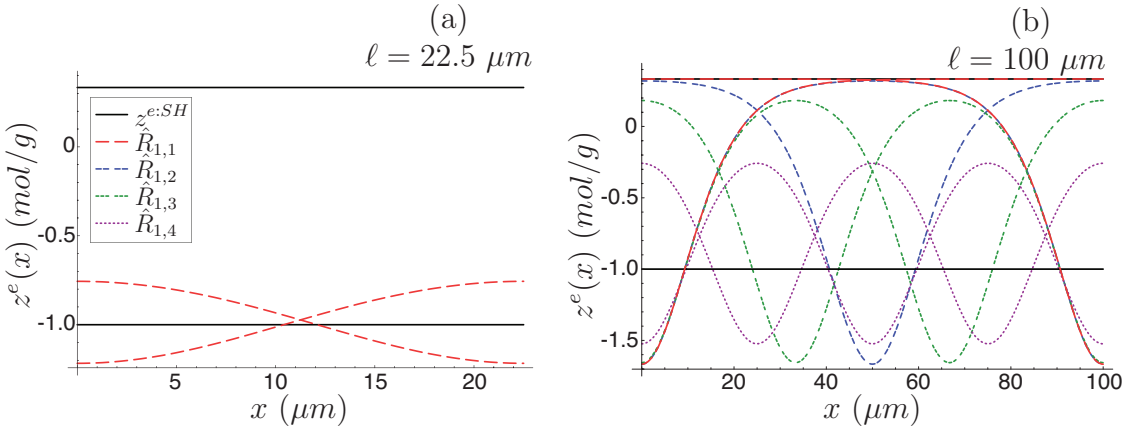

Figure 4.1. Steady state solutions for the $B + B \leftrightharpoons A + A$ mechanism.

unstable occur at integer multiples of a critical domain length,

$$\ell_c = \pi\sqrt{\frac{\mathcal{D}}{\lambda_0}} = \frac{\pi}{\sqrt{2 \times 10^6}} = 22.214\ \mu m, \tag{4.13}$$

where the $m = 1$ diffusion-modification time scale is equal to the unstable reaction time scale. The critical length scale is coupled to a chemical time scale by diffusion: $\ell_c = \pi\sqrt{\mathcal{D}\tau_0}$.

Therefore, when $\ell < \ell_c$, R_1 will have one positive eigenvalue and will in fact be a SIM-BIC for the system; however, for domain lengths longer than ℓ_c, R_1 will have more than one positive eigenvalue, and will no longer qualify as a candidate equilibrium for the SIM-BIC. We therefore seek other candidate equilibria of the steady state Galerkin projection, Eq. (3.49), to fill the role of SIM-BIC for $\ell > \ell_c$.

When the domain length is an integer multiple of the critical length scale, $\ell = m\ell_c$, Eq. (4.13) predicts one of the spectrum of eigenvalues at R_1 to be equal to zero. At these length scales, there are supercritical pitchfork bifurcations at R_1; two additional equilibria undergo a transition from complex to real through the

spatially homogeneous equilibrium R_1. These equilibria have spatial symmetry, so we label them $\hat{R}^+_{1,m}$ and $\hat{R}^-_{1,m}$. This bifurcation can be seen in Figure 4.2 for $m = 1$, where the bold branches have one positive eigenvalue and the dashed branch has two. Since the dynamics of $\hat{R}^+_{1,1}$ and $\hat{R}^-_{1,1}$ are identical, as shown in Section 3.2, we can focus our analysis on one root, $\hat{R}^+_{1,1}$ (with $\zeta_1 > 0$), and for simplicity drop the plus sign superscript. For $\ell > \ell_c$, the $\hat{R}_{1,1}$ equilibria each have one positive eigenvalue and are candidates for the SIM-BIC.

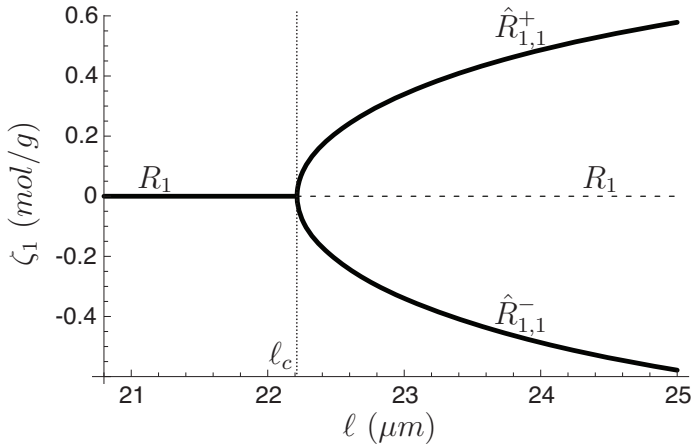

Figure 4.2. Locus of real equilibria in the neighborhood of R_1 for $B + B \leftrightharpoons A + A$.

We examine the solution whose initial conditions are in the neighborhood of $\hat{R}_{1,1}$, perturbed along the eigenfunction whose eigenvalue is positive, and find that it approaches the physical equilibrium along its slowest spatially homogeneous eigenfunction. (Note that an eigenvector of the Jacobian of Eq. (3.49) approxi-

mates an eigenfunction of Eq. (3.48) and is referred to as such.) Therefore, the $\hat{R}_{1,1}$ equilibria meet the requirements to formally become SIM-BICs for all $\ell > \ell_c$.

Subsequent bifurcations at longer domain lengths exhibit similar properties; additional equilibria pairs, $\hat{R}_{1,m}$, correspond to bifurcations at integer multiples of the critical length scale. The bifurcation at $\ell = m\ell_c$ corresponds to the m-th Fourier mode's wavelength being identical to the critical length scale. Additional information about these equilibria is found in Appendix D. Linear stability analysis of these equilibria shows that for $\ell > m\ell_c$, $\hat{R}_{1,m}$ will only have m positive eigenvalues, and the remaining spectrum of eigenvalues will be negative.

Each $\hat{R}_{1,m}$ equilibrium is a fixed point on the finite-dimensional AIM that converges to an equilibrium manifold in the limit as $M \to \infty$. The equilibrium manifolds are spatial functions that satisfy the steady state differential equation,

$$\frac{\dot{\omega}(z^e)}{\rho} + \mathcal{D}\frac{d^2 z}{dx^2} = 0. \tag{4.14}$$

To show the convergence for $\hat{R}_{1,1}$, we quantify the error by comparing the steady solution in a lower order truncation to its corresponding solution in an $M = 25$ Galerkin projection and find the relative root mean square error,

$$\mathcal{E}_m = \left(\frac{\int_0^\ell \left(\tilde{z}_m^e - \tilde{z}_{25}^e\right)^2 dx}{\int_0^\ell \left(\tilde{z}_{25}^e\right)^2 dx} \right)^{\frac{1}{2}}, \text{ for } m = 1, \ldots, 24. \tag{4.15}$$

This convergence is shown in Figure 4.3 for $\ell = 22.5\ \mu m$ and $\ell = 100\ \mu m$. The error of the spatially inhomogeneous steady state solution provides a good metric for the convergence of the Galerkin projection at a particular length scale without imposing an arbitrary initial condition or requiring time integration. We see that the error for $\ell = 100\ \mu m$ converges slowly, remaining relatively large, while the

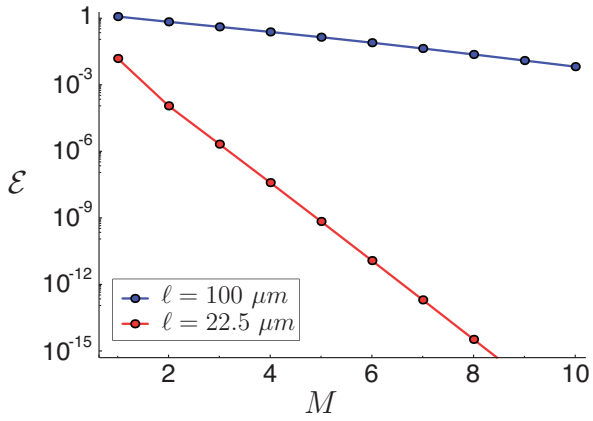

Figure 4.3. Relative error of $\hat{R}_{1,1}$ approximations for $B + B \leftrightharpoons A + A$.

error for $\ell = 22.5\ \mu m$ converges rapidly. This shows that for short domain lengths, where $\ell \lesssim \mathcal{O}(\ell_c)$, lower order truncations not only provide accurate representation of the equilibrium manifold, but also accurately describe the reaction-diffusion dynamics.

We now evaluate approximations of Eq. (4.11) with lower order Galerkin projections. In the limit of an infinitesimal domain length, $\lim \ell \to 0$, the diffusion terms in the projection become infinitely fast for all $m > 0$, any spatial inhomogeneities equilibrate immediately, and the system can be modeled as spatially homogeneous,

$$\frac{dz}{dt} = -1.5 \times 10^6 \, (z+1) \left(z - \frac{1}{3} \right). \tag{4.16}$$

In addition to R_1 and R_2, this system also has two infinite equilibria, $z^{e:SH} \to +\infty \ mol/g$, labeled I_1, and $z^{e:SH} \to -\infty \ mol/g$, labeled I_2. These infinite equilibria are identified using a Poincaré sphere mapping [51]; more details can be found in Appendix E. Evaluating the infinite equilibria, we find that I_1 is unstable and I_2 is stable. The rate of change, $\dot{\Omega}$, is plotted in Figure 4.4; the physical domain,

where both species have positive concentrations, is shown as a gray shaded region. For this $R = 1$-dimensional spatially homogeneous system, a one-dimensional SIM is degenerate; however, we construct it to provide an example of how diffusion modifies the dynamics of a spatially homogeneous system. In one-dimensional systems, there are only sinks and sources, so the SIM-BIC in this case will be a source, since it must have at least one positive eigenvalue. To construct a branch of the SIM, we integrate a system trajectory from the SIM-BIC to the physical equilibrium sink. The two SIM-BICs for this system are at R_1, $z^e = -1$, and at I_1, $z^e \to +\infty$; the SIM branches are shown as a bold red line in Figure 4.4 and constitute the entire phase space between these SIM-BIC equilibria and the physical sink. We will focus our analysis of the reaction-diffusion system on the finite branch of the SIM between R_1 and R_2.

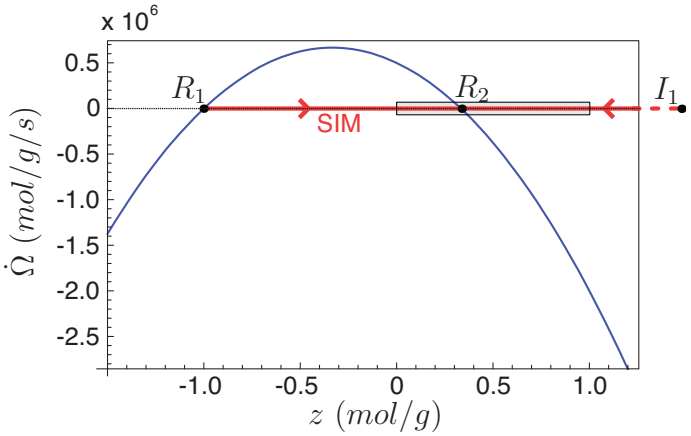

Figure 4.4. Spatially homogeneous rate of change, equilibria, and SIM branches for $B + B \leftrightharpoons A + A$.

We now examine the performance of the spatially inhomogeneous diffusion-modified one-dimensional SIM. In order to evaluate the dynamics of the entire phase space, we use a Poincaré sphere mapping [51], which is given by

$$\eta_i = \frac{\zeta_i}{\sqrt{1 + \sum_{m=0}^{M} \zeta_m^2}}, \quad \text{for } m \in [0, M]. \tag{4.17}$$

In this mapping the system's finite dynamics are shown in addition to the influences that come from the equilibria at infinity. More detail on the Poincaré sphere mapping is provided in Appendix E.

Figure 4.5 shows a projection of the Poincaré sphere mapping of the $M = 1$ truncation at three domain lengths. These results demonstrate the bifurcation of the SIM-BIC and the resulting changes in dynamics; In Figure 4.5(a), where $\ell = 5\ \mu m < \ell_c$, the diffusion time scale is much faster than the reaction time scale. At this length scale the SIM-BIC still resides at the spatially homogeneous R_1, whose eigenvalues are $\lambda = \{2 \times 10^6, -3.748 \times 10^7\}\ s^{-1}$. This causes the slow dynamics to be driven by the reaction mechanism only; therefore, the spatially homogeneous SIM remains the SIM for this reaction-diffusion system. Because the diffusion time scale is faster than the reaction time scale at this length, the trajectories all rapidly collapse onto the η_0 axis, the spatially homogeneous subspace. This results in the spatially homogeneous SIM accurately describing the long time dynamics of the system.

When the length scale is increased to $\ell = 22.5\ \mu m > \ell_c$, as seen in Figure 4.5(b), the diffusion time scale is marginally slower than the unstable reaction time scale at R_1. At this domain length, the first pitchfork bifurcation has three real branches, R_1 and both $\hat{R}_{1,1}$ roots. The slower diffusion means it does not provide a sufficient stabilizing effect on $\lambda_{1,1}$, so R_1 has two positive eigenvalues, $\lambda =$

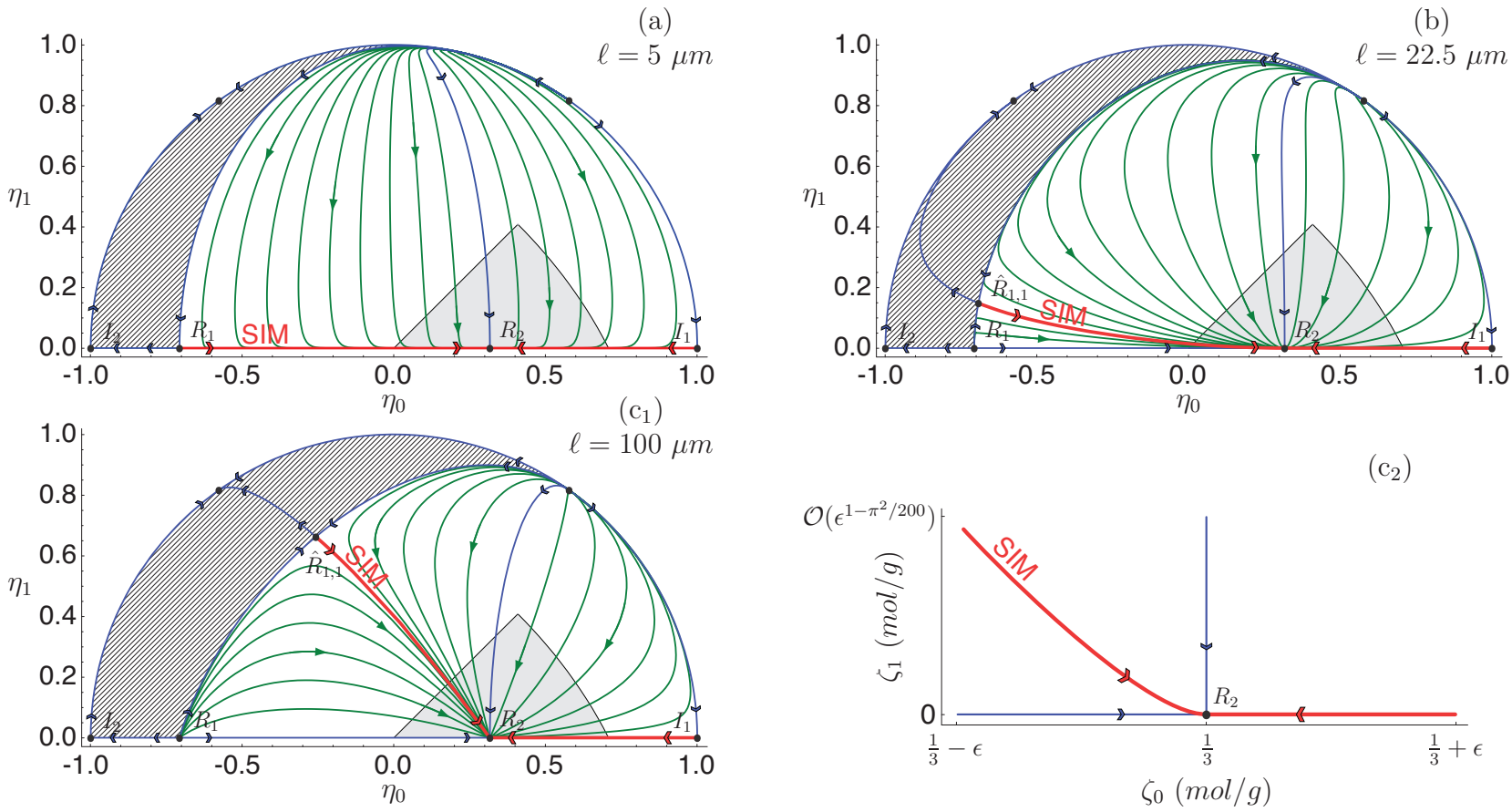

Figure 4.5: Poincaré sphere projection showing the $M = 1$ Galerkin dynamics of $B + B \leftrightharpoons A + A$.

$\{2 \times 10^6, 5.045 \times 10^4\}\ s^{-1}$, and is therefore not a candidate for SIM-BIC; however, $\hat{R}_{1,1}$ each have only one positive eigenvalue, $\lambda = \{2.047 \times 10^6, -9.734 \times 10^4\}\ s^{-1}$, and they formally assume the role as SIM-BIC; however, when we consider the eigenvalues of the physical equilibrium, R_2, $\lambda = \{-2 \times 10^6, -3.950 \times 10^6\}\ s^{-1}$, we find that they have become much closer to the same order of magnitude. This lack of spectral gap indicates that the trajectories in the $\ell = 22.5\ \mu m$ case will not collapse onto either one-dimensional SIM as quickly as they do for shorter lengths. In fact, for lengths on the order of and longer than ℓ_c, trajectories define two- or higher-dimensional manifolds that describe the long time dynamics. Therefore, both the spatially homogeneous and diffusion-modified one-dimensional SIMs in Figure 4.5(b) appear less attractive than the SIM in Figure 4.5(a), where the trajectories in the latter figure approach the one-dimensional SIM with higher curvature than the former.

We consider a still longer length scale, $\ell = 100\ \mu m$, as seen in Figure 4.5(c_1). At this length, the $m = 1$ diffusion time scale is too slow to provide an appreciable stabilizing effect on $\lambda_{1,1}$, and R_1 has two nearly identical positive eigenvalues, $\lambda = \{2 \times 10^6, 1.9013 \times 10^6\}\ s^{-1}$. $\hat{R}_{1,1}$ remains the formal SIM-BIC for this length scale with eigenvalues $\lambda = \{2.048 \times 10^6, -1.949 \times 10^6\}\ s^{-1}$. The ratio of the two eigenvalues associated with the slowest modes in the neighborhood of the physical equilibrium, R_2, approaches unity at this length scale and, therefore, trajectories in this region do not collapse onto the one-dimensional SIM; however, the trajectories in the neighborhood of the SIM-BIC, $\hat{R}_1$, collapse onto the SIM with higher curvature than they did for the $\ell = 22.5\ \mu m$ case. This is because the magnitude of the stable eigenvalue is on the same order of magnitude as the unstable eigenvalue, making for a saddle whose trajectories collapse onto the unstable eigenvector. The

SIM in Figure 4.5(c_1) does not appear to approach R_2 along the slowest (spatially homogeneous) eigenvector, but upon a linear evaluation of the SIM in the neighborhood of R_2. A point on the SIM at $\zeta_0 = 1/3 - \epsilon$ will have $\zeta_1 \sim \mathcal{O}(\epsilon^{1-\pi^2/200})$ as ϵ decays to zero, where the exponent, $1 - \pi^2/200$, is just less than 1. Therefore, as shown in Figure 4.5(c_2), the SIM does osculate the ζ_0 axis in its approach to R_2, confirming that this manifold meets all of our SIM criteria. The $M = 1$ truncation at this length scale is under-resolved; however, the dynamics presented in Figure 4.5(c) are qualitatively the same as a well resolved truncation.

We quantify the attractiveness of the SIM branch for these three length scales using a ratio of normal and tangent stretching rates along the manifold, $r(\boldsymbol{\eta}_{\mathscr{M}})$, adopted from Adrover et al. [10]. More details on this metric are provided in Appendix F. The stretching ratios along the SIM, which quantify the visual metric used in the analysis of Figure 4.5, are shown in Figure 4.6 plotted against the normalized manifold distance $s(\boldsymbol{\eta}_{\mathscr{M}})$. We see that for $\ell = 5\ \mu m$, the stretching ratio is $\mathcal{O}(-20)$, indicating the SIM is a highly attractive manifold for this domain length. For $\ell = 22.5\ \mu m$, the stretching ratio is near zero in the neighborhood of the SIM-BIC, $\hat{R}_{1,1}$, indicating the SIM is only barely attractive in this region; however, near the physical equilibrium, R_2, the stretching ratio is $\mathcal{O}(-2)$, indicating that it is moderately attractive in the physical domain. For the longest domain length, $\ell = 100\ \mu m$, the stretching ratio is $\mathcal{O}(-1)$ along the entire length of the SIM. While the SIM is still attractive, because the normal stretching rate is negative, a manifold such as this SIM, whose normal stretching rates are nearly equal to the tangent stretching rates, is only marginally attractive.

This analysis shows that the use of the spatially homogeneous SIM is only valid for $\ell < \ell_c$; when $\ell > \ell_c$, the bifurcation indicates that both reaction and diffusion

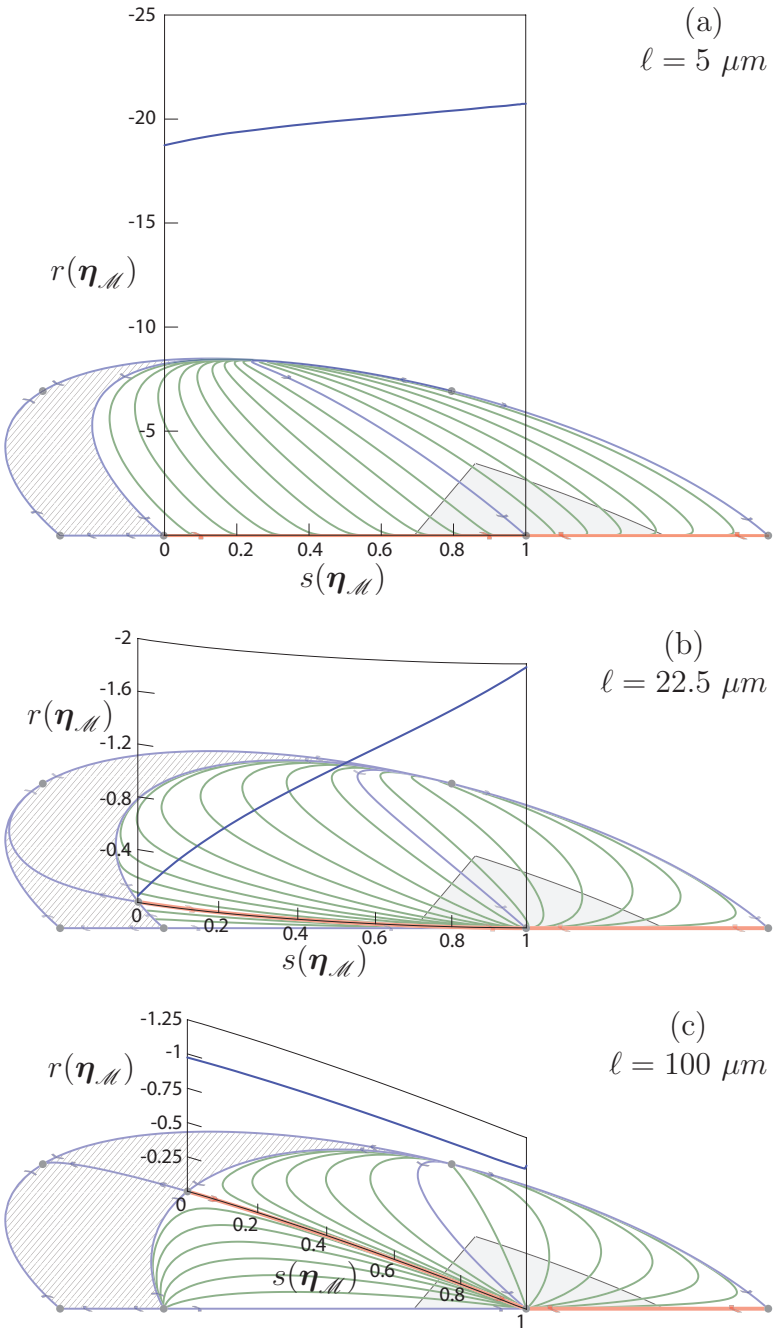

Figure 4.6. Stretching ratios along the SIM in the $M = 1$ Galerkin projection of $B + B \leftrightharpoons A + A$.

must be accounted for in order for a reduced manifold to potentially capture the slow dynamics of the system. Furthermore, a spectral gap needs to be present for a manifold to attract local trajectories and accurately capture the slow dynamics; for $\ell > \ell_c$, a one-dimensional SIM proves to be inadequate.

4.1.2 Diatomic oxygen dissociation

We now examine a physical reaction mechanism under isothermal and isochoric constraints whose spatially homogeneous dynamics are $R = 1$-dimensional: a diatomic-monatomic oxygen dissociation mechanism adapted from Miller et al. [102], which is shown in Table 4.1.

TABLE 4.1

OXYGEN DISSOCIATION MECHANISM

Reaction	a_j $[cm^3/(mol\ s\ \sqrt{K})]$	β_j	$\bar{E}_j$ $[erg/mol]$
$O_2 + M \rightleftharpoons O + O + M$	1.85×10^{11}	0.5	4.0009×10^{12}

There are $N = 2$ species, $J = 1$ reaction, and $L = 1$ element where we choose $i = \{1, 2\}$ to correspond to the species $\{O, O_2\}$, respectively. This system has the species-element matrix,

$$\varphi_{ln} = \begin{bmatrix} 1 & 2 \end{bmatrix}, \tag{4.18}$$

and the species-reaction matrix,

$$\nu_{nj} = \begin{bmatrix} 2 \\ -1 \end{bmatrix}. \tag{4.19}$$

The reaction rate is given by

$$r_1 = k_1 \left(\frac{\rho Y_2}{\bar{\mathsf{M}}_{O_2}} \left(\frac{\rho Y_1}{\bar{\mathsf{M}}_O} + \frac{\rho Y_2}{\bar{\mathsf{M}}_{O_2}} \right) - \frac{1}{K_1^c} \left(\frac{\rho Y_1}{\bar{\mathsf{M}}_O} \right)^2 \left(\frac{\rho Y_1}{\bar{\mathsf{M}}_O} + \frac{\rho Y_2}{\bar{\mathsf{M}}_{O_2}} \right) \right), \tag{4.20}$$

where the terms with the summation of both species represent the third body molecule, M. This system has $\hat{L} = L = 1$ algebraic constraint, representing the elemental constraint on oxygen atoms,

$$C_O = \frac{Y_1}{\bar{\mathsf{M}}_O} + 2\frac{Y_2}{\bar{\mathsf{M}}_{O_2}}, \tag{4.21}$$

where C_O is a constant which can be defined from the initial conditions

$$C_O = \frac{Y_1^*}{\bar{\mathsf{M}}_O} + 2\frac{Y_2^*}{\bar{\mathsf{M}}_{O_2}}. \tag{4.22}$$

In this case, the constant can be determined, independent of initial conditions, because $Y_1 + Y_2 = 1$ and $\bar{\mathsf{M}}_O = 2\bar{\mathsf{M}}_{O_2}$, yielding

$$C_O = \frac{1}{\bar{\mathsf{M}}_O}. \tag{4.23}$$

Following the reduction technique described in Section 3.1.3, we now transform the equations to describe the evolution in one reduced variable. We choose specific moles of O, which we represent as z without any subscript, for our reduced

variable,

$$z = \frac{Y_1}{\mathsf{M}_O}. \tag{4.24}$$

The modified coefficient matrix, $\hat{\nu}$, used in our reduction is

$$\hat{\nu} = \begin{bmatrix} 1 \\ -\frac{1}{2} \end{bmatrix}. \tag{4.25}$$

The specific moles of O_2 are algebraically coupled to z by the relation

$$\hat{z}_2 = \frac{1}{2\bar{\mathsf{M}}_O} - \frac{z}{2}, \tag{4.26}$$

which can then be substituted into Eq. (4.20) to yield the evolution in terms of the reduced variables,

$$\frac{\partial z}{\partial t} = \frac{k_1\rho}{2\bar{\mathsf{M}}_O^2} - \left(\frac{k_1\rho}{2} + \frac{k_1\rho^2}{K_1^c\bar{\mathsf{M}}_O}\right) z^2 - \frac{k_1\rho^2}{K_1^c} z^3 + \mathcal{D}\frac{\partial^2 z}{\partial x^2}. \tag{4.27}$$

We evaluate this system at constant temperature, $T = 5000\ K$, and density, $\rho = 1.6 \times 10^{-4}\ g/cm^3$. These parameters yield pressures between $P = 2.05\ atm$ and $P = 4.10\ atm$ when both species have physical concentrations. We use a diffusion coefficient, $\mathcal{D} = 8.09\ cm^2/s$, which is approximated from a weighted average of the ordinary multi-component coefficients in the `CHEMKIN TRANSPORT` database [103]. These parameters yield the evolution equation,

$$\begin{aligned} \frac{\partial z}{\partial t} \;=\; & \left(270.32\ \frac{mol}{g\ s}\right) - \left(80861\ \frac{g}{mol\ s}\right) z^2 - \left(1.8654 \times 10^6\ \frac{g^2}{mol^2\ s}\right) z^3 + \\ & \left(8.09\ \frac{cm^2}{s}\right) \frac{\partial^2 z}{\partial x^2}. \end{aligned} \tag{4.28}$$

Expanding Eq. (4.28) through a Galerkin projection yields a system of ODEs. In the limit of an infinitesimal domain length, $\lim \ell \rightarrow 0$, the diffusion terms in the projection become infinitely fast, any spatial inhomogeneities equilibrate immediately, and the system can be modeled as spatially homogeneous,

$$\frac{dz}{dt} = \left(270.32 \ \frac{mol}{g \ s}\right) - \left(80861 \ \frac{g}{mol \ s}\right) z^2 - \left(1.8654 \times 10^6 \ \frac{g^2}{mol^2 \ s}\right) z^3. \quad (4.29)$$

Figure 4.7 shows the spatially homogeneous reaction source term, which has the following three finite equilibria,

$$z^{e:SH} = \{-0.4255, -0.0625, 0.05449\} \ mol/g, \quad (4.30)$$

that are labeled R_1, R_2, and R_3, respectively; the eigenvalues of the linearized

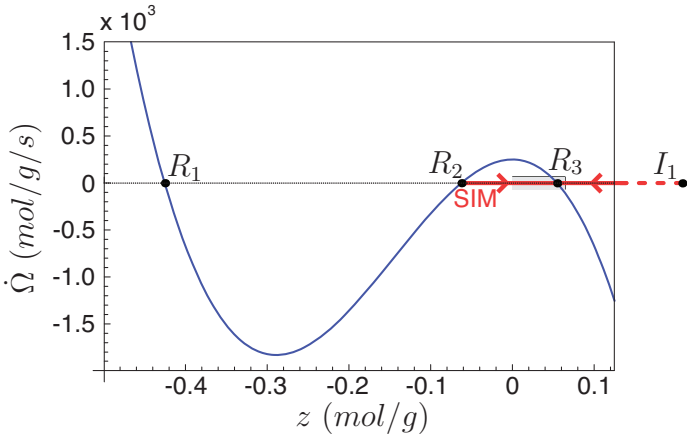

Figure 4.7. Spatially homogeneous oxygen dissociation SIM branches.

system about these equilibria are

$$\lambda_0 = \left\{-3.250 \times 10^4, 7.922 \times 10^3, -1.047 \times 10^4\right\}\ s^{-1}, \tag{4.31}$$

respectively. Therefore, the first and third equilibria are stable, while the second is unstable. This system also has two infinite equilibria (identified by using a Poincaré sphere mapping [51]) at $z^e =\!\!\rightarrow \pm\infty$, each of which are unstable. Note that only the equilibrium at $z^e = 0.05449\ mol/g$ is physical, as the other equilibria have negative species concentrations. The physical domain is shown in Figure 4.7 as a gray shaded region. For this $R = 1$-dimensional spatially homogeneous system, a one-dimensional SIM is degenerate; however, we still construct it to assist in the following spatially inhomogeneous analysis. Again, the SIM-BIC will be a source, since it only has one eigenvalue, which must be positive. To construct a branch of the SIM, we integrate a system trajectory from the SIM-BIC to the physical equilibrium sink. The two SIM-BICs for this system are at R_2, $z^e = -0.0625\ mol/g$ and $z^e =\!\!\rightarrow +\infty$; the SIM branches are shown as a bold line in Figure 4.7 and constitute the entire phase space between these SIM-BIC equilibria and the physical sink. We will focus our analysis of the reaction-diffusion system on the finite branch of the SIM between R_2 and R_3.

For slightly longer lengths, we retain one additional term in the Galerkin projection by truncating the series at $M = 1$. This yields a two-dimensional system of ODEs in ζ_0 and ζ_1. Here ζ_0 represents the spatially homogeneous specific moles of O, and ζ_1 represents the amplitude of the spatial variations in the specific moles of O corresponding to the first Fourier mode. In this projection, the spatially homogeneous subspace remains, including all five spatially homogeneous equilibria. The additional Fourier mode introduces one of the diffusion time scales; this

time scale depends on domain length ℓ and combines with the reaction time scale to make a modified time scale. This additional time scale is shown in Figure 4.8, where the bold solid lines are the spatially homogeneous, reaction-only time

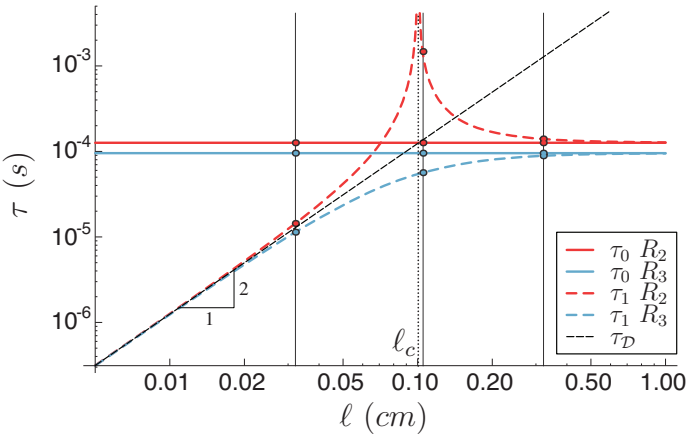

Figure 4.8. Local time scales of R_2 and R_3.

scales, the bold dashed lines are the diffusion-modified time scales, and the thin dashed line is the diffusion time scale of the first Fourier mode for length ℓ. The reaction-only time scales are independent of ℓ, while the diffusion-modified time scales are dominated by diffusion for small ℓ and dominated by reaction for large ℓ. In the neighborhood of the SIM-BIC, R_2, we see a singularity in the diffusion modified time scale, indicating a zero eigenvalue where the stable diffusion equals the unstable reaction; this occurs at the critical length scale,

$$\ell_c = \pi \sqrt{\frac{\mathcal{D}}{\lambda_{0,1}^{e:R2}}} = 1.004 \ mm. \tag{4.32}$$

At this critical length scale, there is a supercritical pitchfork bifurcation at R_2, which can be seen in Figure 4.9. The two additional equilibria, $\hat{R}^+_{2,1}$ and $\hat{R}^-_{2,1}$,

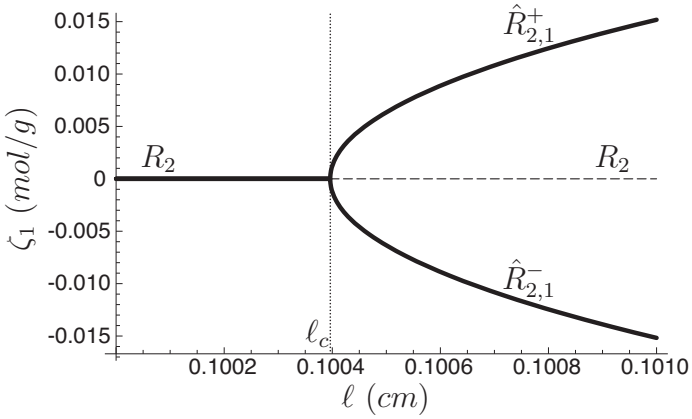

Figure 4.9. Locus of real equilibria in the neighborhood of R_2.

are spatially symmetric, so we again analyze $\hat{R}^+_{2,1}$ (root with $\zeta_1 > 0$), and drop the plus sign superscript; their locations vary with the domain length. If the diffusion time scale is slower than the unstable reaction time scale, $\ell > \ell_c$, then $\hat{R}_{2,1}$ is complex; however, if the reaction is as slow as or slower than diffusion, $\ell \leq \ell_c$, then it is real. At the critical domain length, ℓ_c, $\hat{R}_{2,1}$ forms a spatially homogeneous triple-root at R_2 with a diffusion-modified eigenvalue of zero.

In order to evaluate this bifurcation in the entire phase space, we use a modified Poincaré sphere mapping, which scales the finite region in ζ-space to provide a more clear illustration of the dynamics in the physical domain. This mapping is

given by

$$\eta_i = \frac{\zeta_i}{\sqrt{\alpha^2 + \sum_{m=0}^{M} \zeta_m^2}}, \quad \text{for } m \in [0, M], \tag{4.33}$$

where α is a scaling parameter, which we choose as $\alpha = 1/\mathsf{M}_O = 0.0625\ mol/g$. The results, shown in Figure 4.10, are qualitatively the same as those described in Section 4.1.1. In Figure 4.10(a), diffusion across the domain length, $\ell = 321\ \mu m$, occurs at a faster time scale than the reaction time scale. The SIM-BIC is the spatially homogeneous R_2, whose eigenvalues are $\lambda = \{7922, -6.957 \times 10^4\}\ s^{-1}$. Reaction (the spatially homogeneous SIM) governs the slow dynamics, and all trajectories rapidly collapse onto the η_0 axis.

Figure 4.10(b) depicts the dynamics of a slightly longer domain length, $\ell = 1.01\ mm$. The SIM-BIC is now the $\hat{R}_{2,1}$ equilibrium, whose eigenvalues are $\lambda = \{7918, -188.0\}\ s^{-1}$, since R_2 has two positive eigenvalues, $\lambda = \{7922, 94.46\}\ s^{-1}$. The lack of spectral gap between the two eigenvalues indicates that neighboring trajectories do not rapidly collapse onto the SIM.

The longest domain length we examine, $\ell = 3.21\ mm$, is shown in Figure 4.10(c). The SIM-BIC remains R_2, whose eigenvalues are $\lambda = \{7776, -9932\}\ s^{-1}$, while $\hat{R}_{2,1}$ remains a source in this projection with eigenvalues $\lambda = \{7922, 7147\}\ s^{-1}$. We again predict a low stiffness ratio in the neighborhood of the physical equilibrium, indicating trajectories in this region do not collapse onto the SIM; however, near $\hat{R}_{2,1}$, the ratio of eigenvalues provides for a SIM that is more attractive than for $\ell = 1.01\ mm$. The $M = 1$ truncation of $\ell = 3.21\ mm$ is under-resolved, but qualitatively depicts the same dynamics as a well resolved simulation.

We again find that the spatially homogeneous SIM is only the canonical slow manifold for $\ell < \ell_c$. When we evaluate domains longer than the critical length scale, $\ell > \ell_c$, we predict spatial inhomogeneities to persist until the approach to

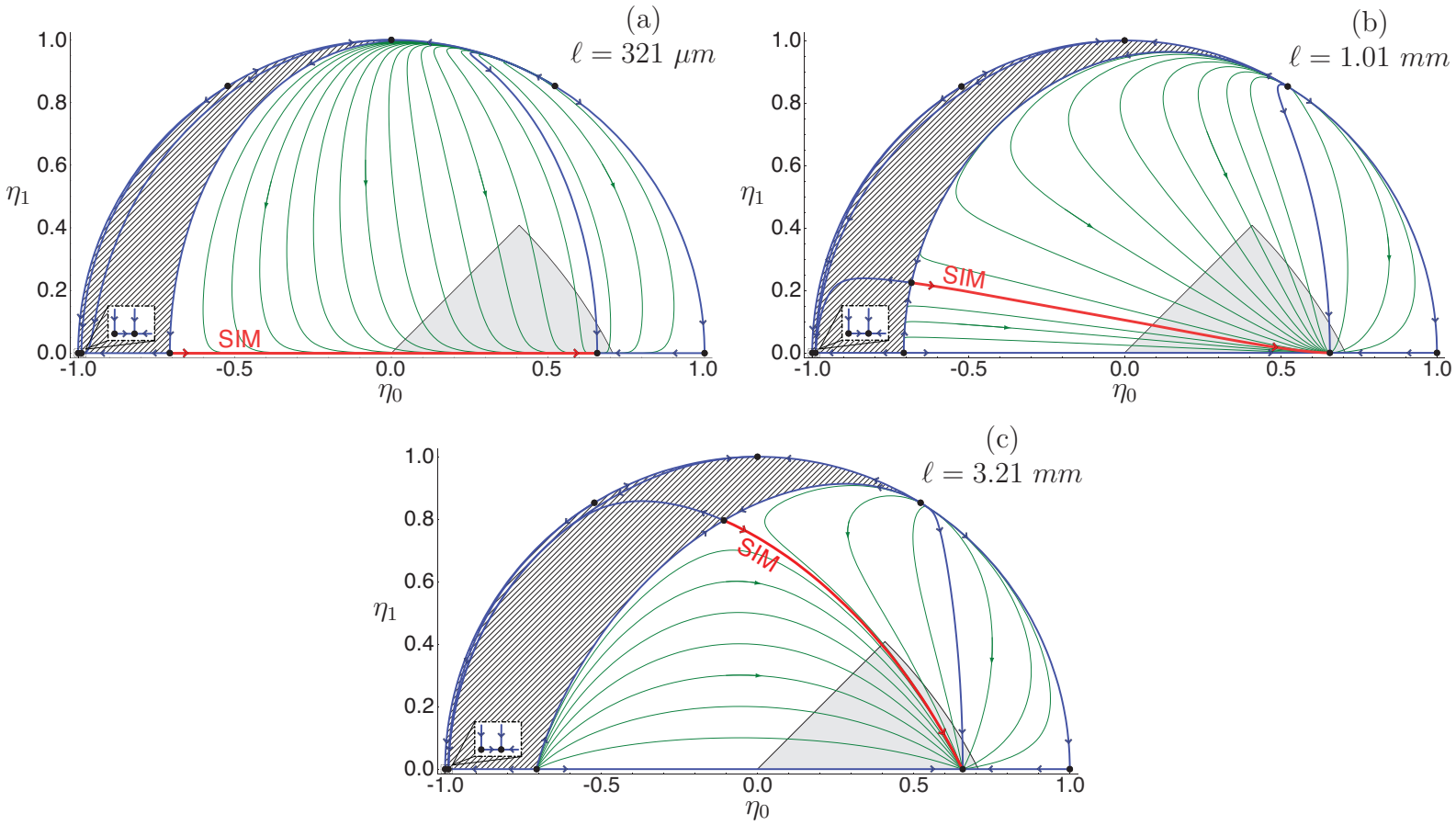

Figure 4.10: $M = 1$ Galerkin projection dynamics in Poincaré sphere.

the physical equilibrium. The diffusion-modified one-dimensional SIM that we identify does not accurately capture the slow dynamics of the system. The parity in the eigenvalues of these longer length scales identifies that a higher dimensional SIM is necessary to accurately describe the long time dynamics of the system.

To examine the accuracy of truncations at small M, we retain additional terms in the Galerkin projection and evaluate the convergence of $\hat{R}_{2,1}$. The approximations of $\hat{R}_{2,1}$ in each subsequent truncation are fixed points on higher, yet still finite, dimensional AIMs that converge to an equilibrium manifold of the PDE in the limit of $M \to \infty$. We demonstrate this convergence by finding the amplitudes of $\hat{R}_2$ in the first six truncations for $\ell = 1.01\ mm$ and $\ell = 3.21\ mm$, shown in Table 4.2. The spatial reconstruction of these approximate equilibria manifolds is shown in Figure 4.11. To quantify the error, we compared the solutions at each

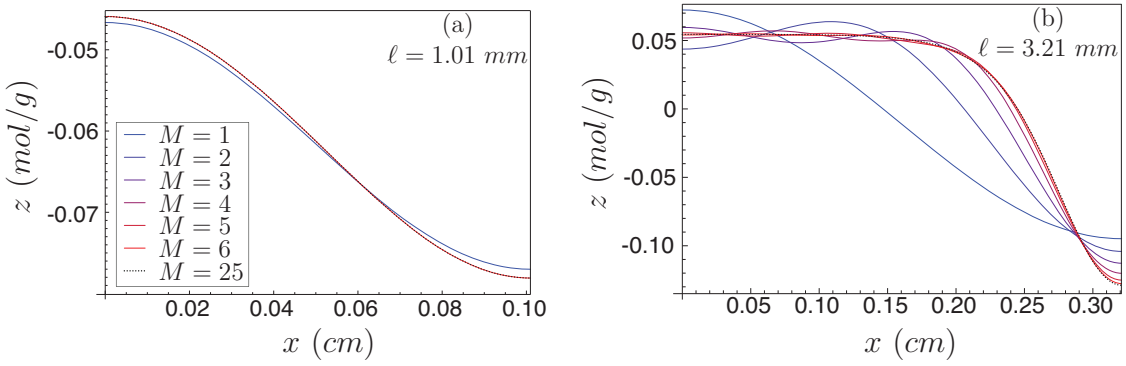

Figure 4.11. Convergence to an equilibrium manifold.

length scale to a Galerkin projection truncated at $M = 25$. Figure 4.12 shows

TABLE 4.2:

CONVERGENCE OF THE AMPLITUDES OF $\hat{R}_{2,1}$ IN THE O_2 DISSOCIATION MECHANISM

M	ζ_0 $[mol/g]$	ζ_1 $[mol/g]$	ζ_2 $[mol/g]$	ζ_3 $[mol/g]$	ζ_4 $[mol/g]$	ζ_5 $[mol/g]$	ζ_6 $[mol/g]$
for $\ell = 1.01\ mm$							
1	-0.06182	0.01518					
2	-0.06174	0.01609	-2.549×10^{-4}				
3	-0.06174	0.01609	-2.549×10^{-4}	-7.300×10^{-8}			
4	-0.06174	0.01609	-2.549×10^{-4}	-7.379×10^{-8}	6.628×10^{-8}		
5	-0.06174	0.01609	-2.549×10^{-4}	-7.379×10^{-8}	6.628×10^{-8}	-1.031×10^{-9}	
6	-0.06174	0.01609	-2.549×10^{-4}	-7.379×10^{-8}	6.628×10^{-8}	-1.031×10^{-9}	-6.019×10^{-13}
for $\ell = 3.21\ mm$							
1	-0.01127	0.08357					
2	0.007801	0.07391	-0.03801				
3	0.01487	0.06689	-0.04147	0.01926			
4	0.01761	0.06367	-0.04210	0.02230	-0.00963		
5	0.01856	0.06249	-0.04223	0.02341	-0.01105	0.00446	
6	0.01882	0.06217	-0.04227	0.02374	-0.01152	0.00493	-0.00183

the convergence of the relative error, $\mathcal{E}_i$, defined in Eq. (4.15). We see that

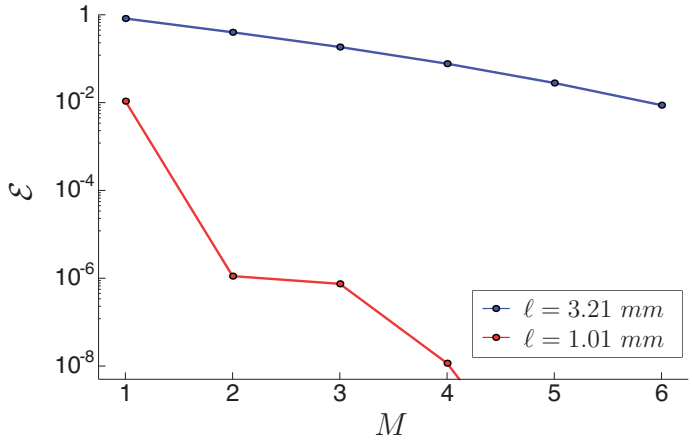

Figure 4.12. Relative error of $\hat{R}_2$ approximations.

the $\ell = 3.21\ mm$ equilibrium has large errors for the truncations with small M, where the $\ell = 1.01\ mm$ equilibrium's errors are much smaller and converge to the resolution of Figure 4.11 by $M = 2$.

Another manifestation of the truncation error is apparent in the evolution of Galerkin amplitudes for the $M = 6$ truncation. The absolute value of the amplitudes are shown in Figure 4.13 evolving in time for the three length scales. This demonstrates why there is large error for the longer length scales in the truncations at smaller M values. Each of these evolutions has identical initial conditions in their respective Galerkin projections, $\zeta_0 = 0.02083\ mol/g$, $\zeta_1 = 0.02083\ mol/g$, and $\zeta_m = 0\ mol/g$ for $m > 1$; these initial conditions correspond to similar functions with varying wavelengths, which are all physically realizable

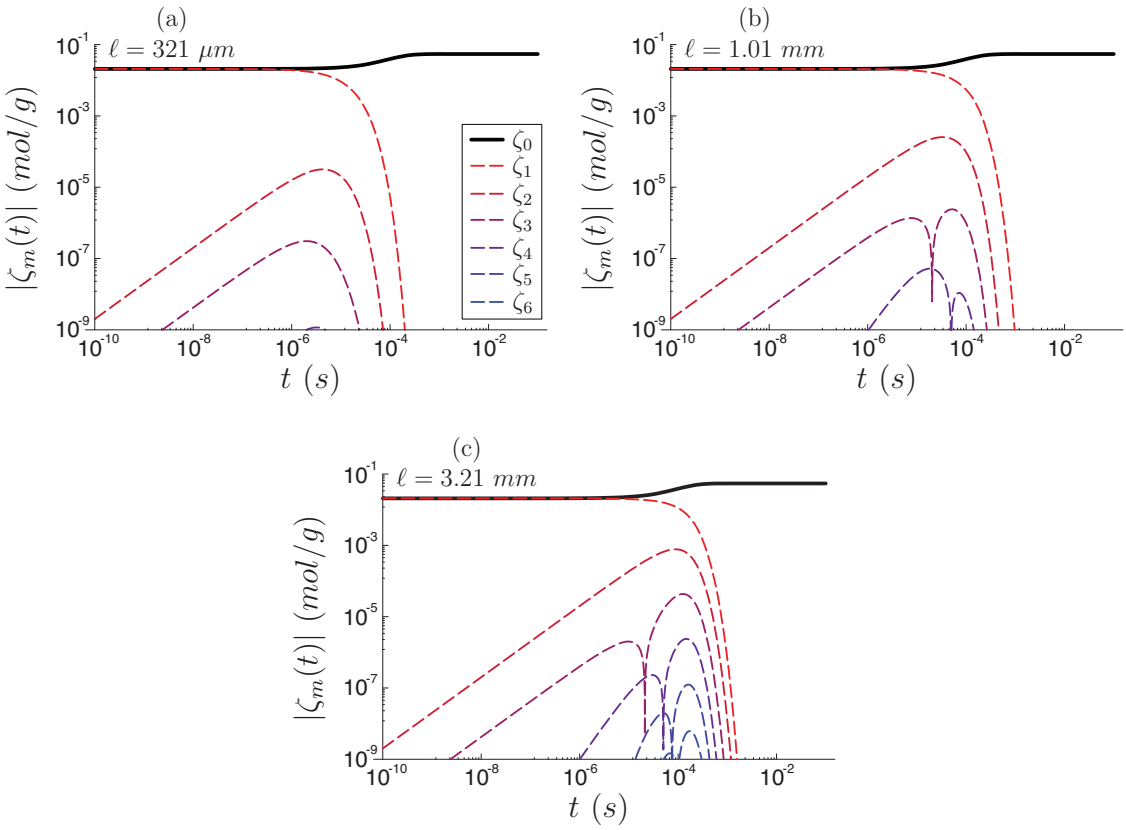

Figure 4.13. Evolution of $M = 6$ Galerkin projection amplitudes.

(spatial functions all have positive species concentrations). Despite initially having zero amplitudes for $m > 1$, the nonlinear reaction term induces a coupling of modes that causes growth in these higher amplitudes. For short domain lengths, where diffusion is faster than reaction, the stabilizing effects of diffusion cause the decay of these amplitudes both before they grow too large and before the reaction occurs; however, for domain lengths longer than ℓ_c, diffusion does not induce a decay in the larger m amplitudes before reaction, which allows the higher modes to grow and affect the dynamics of reaction. The larger the wavelength in the initial conditions, the slower the decay, including the shorter wavelength-induced amplitudes; therefore, including more modes in the simulation is necessary in order to resolve the system's dynamics. The cusps in Figure 4.13 (b) and (c) are a result of sign changes in the amplitude of the spatially inhomogeneous modes whose absolute values are plotted on a logarithmic scale.

We now examine another pertinent aspect of this Galerkin representation of our system; in the higher order Galerkin projections, we find additional equilibria pairs that each correspond to a bifurcation at the length scale where the diffusion time scale in the higher modes, $m = 2$ through $m = M$, is equal to the unstable reaction time scale at R_2,

$$\ell_{c,m} = m\pi\sqrt{\frac{\mathcal{D}}{\lambda_{0,1}^{e:R2}}} = m\ell_c; \tag{4.34}$$

we label these equilibria $\hat{R}_{2,m}$. Furthermore, we find that the $\hat{R}_{2,m}$ equilibria on domain length ℓ converge to identical spatial functions as $\hat{R}_2$ on domain length ℓ/m. This phenomena indicates that the bifurcation and subsequent $\hat{R}_{2,m}$ equilibria are correlated to a physical wavelength; the bifurcation will always occur where the physical wavelength's diffusion time scale is equal to the unstable reac-

tion time scale, and for a given physical wavelength, the $\hat{R}_{2,m}$ equilibrium manifold will have a specific shape in function space. This phenomena is examined in more detail in Appendix D. Using the unstable reaction time scale at R_2, we find the critical length scale is $\ell_c = 1.004\ mm$; therefore, the $\hat{R}_{2,2}$ bifurcation occurs at $\ell = \ell_{c,2} = 2\ell_c = 2.008\ mm$, $\hat{R}_{2,3}$ at $\ell = \ell_{c,3} = 3\ell_c = 3.012\ mm$, and so on. This means that when we consider $\ell = 1.01\ mm$, only the first pair of equilibria will have undergone the bifurcation, while for $\ell = 3.21\ mm$, the first three pairs of equilibria will have bifurcated.

Examining these equilibria at $\ell = 3.21\ mm$, which are shown in Figure 4.14, we find the amplitudes of $\hat{R}_{2,2}$ to be

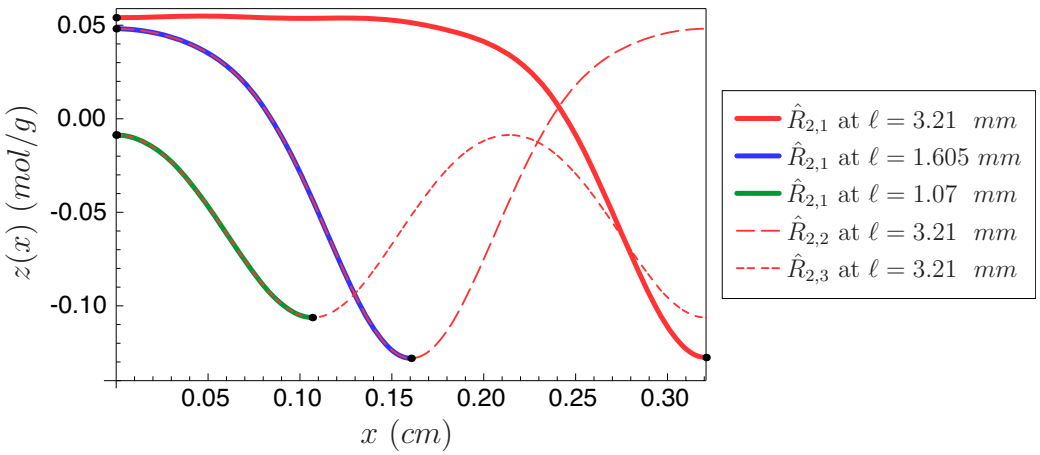

Figure 4.14. Higher truncation $\hat{R}_{2,m}$ approximations and corresponding fundamental $\hat{R}_2$ approximations.

$$\hat{R}_{2,2}(\ell = 3.21\ mm) = \begin{bmatrix} -0.01689 \\ 0 \\ 0.08428 \\ 0 \\ -0.02308 \\ 0 \\ 0.003813 \end{bmatrix}, \tag{4.35}$$

which correspond to

$$\hat{R}_{2}(\ell = 1.605\ mm) = \begin{bmatrix} -0.01689 \\ 0.08428 \\ -0.02308 \\ 0.003813 \end{bmatrix}. \tag{4.36}$$

We find that $\hat{R}_{2,2}$ has two positive eigenvalues and the rest negative, and find that it is simply a composite function of the two spatially symmetric functions: $\hat{R}_2^+(\ell = 1.605\ mm)$ from $x \in [0\ mm, 1.605\ mm]$ and $\hat{R}_2^-(\ell = 1.605\ mm)$ from $x \in [1.605\ mm, 3.21\ mm]$. The third bifurcation, $\hat{R}_{2,3}$, predicted at $\ell = 3.21\ mm$,

has three positive eigenvalues and the rest negative, and amplitudes

$$\hat{R}_{2,3}(\ell = 3.21\ mm) = \begin{bmatrix} -0.05467 \\ 0 \\ 0 \\ 0.04880 \\ 0 \\ 0 \\ -0.002798 \end{bmatrix}, \tag{4.37}$$

which correspond to

$$\hat{R}_{2}(\ell = 1.07\ mm) = \begin{bmatrix} -0.05467 \\ 0.04880 \\ -0.002798 \end{bmatrix}. \tag{4.38}$$

Again, we find that $\hat{R}_{2,3}$ is simply a composite function of spatially symmetric functions, $\hat{R}_2^+(\ell = 1.07\ mm)$ and $\hat{R}_2^-(\ell = 1.07\ mm)$. This consistency in equilibria solutions for physical wavelengths indicates that only the $\hat{R}_2$ equilibrium need be solved for since it can be used subsequently to identify all $\hat{R}_{2,m}$ equilibria for longer length scales, which could prove useful in building higher-dimensional SIMs.

We see for this simple one-dimensional realistic chemical system, when the spatial resolution is not fine enough to have the fundamental diffusion time scale faster than the pertinent reaction time scale, the assumption of spatially homogeneous dynamics breaks down.

4.1.3 Zel'dovich mechanism

We now examine the Zel'dovich mechanism of NO production, which is shown in Table 4.3. Al-Khateeb et al. [49] studied the spatially homogeneous Zel'dovich mechanism under isothermal and isochoric constraints; we extend their analysis to reaction-diffusion and adiabatic systems. This system displays realistic chemical dynamics and has a slightly higher dimension ($R = 2$) than the previous example.

TABLE 4.3

THE ZEL'DOVICH MECHANISM FOR NO PRODUCTION

Reaction	a_j $[cm^3/(mol\ s)\ K^{-\beta_j}]$	β_j	$\bar{E}_j$ $[erg/mol]$
$N + O_2 \leftrightharpoons NO + O$	5.841×10^9	1.01	6195.6
$N + NO \leftrightharpoons N_2 + O$	21.077×10^{12}	0.00	0.0

There are $N = 5$ species, $J = 2$ reactions, and $L = 2$ elements, where the species $\{NO, N, O, O_2, N_2\}$ correspond to $i = 1, \ldots, 5$. The species-reaction ma-

trix for this mechanism is

$$\nu_{ij} = \begin{bmatrix} 1 & -1 \\ -1 & -1 \\ 1 & 1 \\ -1 & 0 \\ 0 & 1 \end{bmatrix}, \tag{4.39}$$

and the species-element matrix is

$$\varphi_{li} = \begin{bmatrix} 1 & 1 & 0 & 0 & 2 \\ 1 & 0 & 1 & 2 & 0 \end{bmatrix}. \tag{4.40}$$

The reaction rates are given by

$$r_2 = k_2 \left(\frac{\rho Y_2}{\bar{\mathsf{M}}_N} \frac{\rho Y_4}{\bar{\mathsf{M}}_{O_2}} - \frac{1}{K_2^c} \frac{\rho Y_1}{\bar{\mathsf{M}}_{NO}} \frac{\rho Y_3}{\bar{\mathsf{M}}_O} \right), \tag{4.41a}$$

$$r_1 = k_1 \left(\frac{\rho Y_2}{\bar{\mathsf{M}}_N} \frac{\rho Y_1}{\bar{\mathsf{M}}_{NO}} - \frac{1}{K_1^c} \frac{\rho Y_5}{\bar{\mathsf{M}}_{N_2}} \frac{\rho Y_3}{\bar{\mathsf{M}}_O} \right). \tag{4.41b}$$

This mechanism has one additional constraint; since both reactions are bimolecular, the total number of molecules remains constant; therefore, the system has $\hat{L} = 3$ algebraic constraints,

$$C_M = \frac{Y_1}{\bar{\mathsf{M}}_{NO}} + \frac{Y_2}{\bar{\mathsf{M}}_N} + \frac{Y_3}{\bar{\mathsf{M}}_O} + \frac{Y_4}{\bar{\mathsf{M}}_{O_2}} + \frac{Y_5}{\bar{\mathsf{M}}_{N_2}}, \tag{4.42a}$$

$$C_N = \frac{Y_1}{\bar{\mathsf{M}}_{NO}} + \frac{Y_2}{\bar{\mathsf{M}}_N} + 2\frac{Y_5}{\bar{\mathsf{M}}_{N_2}}, \tag{4.42b}$$

$$C_O = \frac{Y_1}{\bar{\mathsf{M}}_{NO}} + \frac{Y_3}{\bar{\mathsf{M}}_O} + 2\frac{Y_4}{\bar{\mathsf{M}}_{O_2}}. \tag{4.42c}$$

The variables C_M, C_N, and C_O are constants that are defined by the initial condi-

tions and correspond to the conservation of total molecules, nitrogen atoms, and oxygen atoms, respectively. We use these algebraic constraints to transform our system into two reduced variables, choosing specific moles of NO and N, which we represent as z_1 and z_2, respectively,

$$z_1 = \frac{Y_1}{\mathsf{M}_{NO}}, \tag{4.43a}$$

$$z_2 = \frac{Y_2}{\mathsf{M}_{N}}. \tag{4.43b}$$

Using the reduction technique from Section 3.1.3, we find the modified coefficient matrix to be

$$\mathfrak{D}_{in} = \begin{bmatrix} 1 & 0 \\ 0 & 1 \\ 0 & -1 \\ -\frac{1}{2} & \frac{1}{2} \\ -\frac{1}{2} & -\frac{1}{2} \end{bmatrix}. \tag{4.44}$$

The remaining $\hat{L} = 3$ species' specific mole values are coupled to z_1 and z_2 by the algebraic relations

$$\hat{z}_3 = \hat{z}_3^* + z_2^* - z_2, \tag{4.45a}$$

$$\hat{z}_4 = \hat{z}_4^* + \frac{1}{2}z_1^* - \frac{1}{2}z_2^* - \frac{1}{2}z_1 + \frac{1}{2}z_2, \tag{4.45b}$$

$$\hat{z}_5 = \hat{z}_5^* + \frac{1}{2}z_1^* + \frac{1}{2}z_2^* - \frac{1}{2}z_1 - \frac{1}{2}z_2. \tag{4.45c}$$

4.1.3.1 Isothermal

This system is evaluated at the constant temperature, $T = 4000\ K$, and density, $\rho = 1.20024 \times 10^{-4}\ g/cm^3$, which yields a constant pressure, $P =$

1.64 atm. The species' thermodynamic data comes from the `CHEMKIN` thermodynamic database [104]. The diffusion coefficient, $\mathcal{D} = 14.0\ cm^2/s$, is approximated from a weighted average of the ordinary multi-component coefficients in the `CHEMKIN TRANSPORT` database [103]. We choose initial conditions such that the values of the constants are $C_O = C_N = 3.3327 \times 10^{-2}\ mol/g$ and $C_M = 4.1658 \times 10^{-2}\ mol/g$. The governing equations, when transformed into specific moles, are

$$\begin{aligned}
\frac{\partial z_1}{\partial t} &= \left(250.46\ \frac{mol}{g\ s}\right) - \left(99728\ \frac{1}{s}\right) z_1 + \left(1.1611 \times 10^7\ \frac{1}{s}\right) z_2 - \\
&\quad \left(3.2210 \times 10^9\ \frac{g}{mol\ s}\right) z_1 z_2 + \left(6.9858 \times 10^8\ \frac{g}{mol\ s}\right) z_2^2 + \\
&\quad (14.0\ cm^2/s) \frac{\partial^2 z_1}{\partial x^2}, \qquad (4.46a) \\
\frac{\partial z_2}{\partial t} &= \left(250.46\ \frac{mol}{g\ s}\right) + \left(84697\ \frac{1}{s}\right) z_1 - \left(1.1656 \times 10^7\ \frac{1}{s}\right) z_2 - \\
&\quad \left(1.8359 \times 10^9\ \frac{g}{mol\ s}\right) z_1 z_2 - \left(6.9768 \times 10^8\ \frac{g}{mol\ s}\right) z_2^2 + \\
&\quad (14.0\ cm^2/s) \frac{\partial^2 z_1}{\partial x^2}. \qquad (4.46b)
\end{aligned}$$

When we evaluate the system in the limit of an infinitesimal domain length, a truncation at $M = 0$ is appropriate, and we are left with the spatially homogeneous system,

$$\begin{aligned}
\frac{dz_1}{dt} &= \left(250.46\ \frac{mol}{g\ s}\right) - \left(99728\ \frac{1}{s}\right) z_1 + \left(1.1611 \times 10^7\ \frac{1}{s}\right) z_2 - \\
&\quad \left(3.2210 \times 10^9\ \frac{g}{mol\ s}\right) z_1 z_2 + \left(6.9858 \times 10^8\ \frac{g}{mol\ s}\right) z_2^2, \qquad (4.47a) \\
\frac{dz_2}{dt} &= \left(250.46\ \frac{mol}{g\ s}\right) + \left(84697\ \frac{1}{s}\right) z_1 - \left(1.1656 \times 10^7\ \frac{1}{s}\right) z_2 - \\
&\quad \left(1.8359 \times 10^9\ \frac{g}{mol\ s}\right) z_1 z_2 - \left(6.9768 \times 10^8\ \frac{g}{mol\ s}\right) z_2^2, \qquad (4.47b)
\end{aligned}$$

which is the same system described by Al-Khateeb et al. [49]. The phase space for this system is shown in Figure 4.15. This system has three finite spatially-homogeneous equilibria,

$$\mathbf{z}^e = \left\{ \begin{bmatrix} -1.7833 \times 10^{-5} \\ -1.6681 \times 10^{-2} \end{bmatrix}, \begin{bmatrix} -4.1950 \times 10^{-3} \\ -2.6642 \times 10^{-5} \end{bmatrix}, \begin{bmatrix} 3.0474 \times 10^{-3} \\ 2.9446 \times 10^{-5} \end{bmatrix} \right\} \; mol/g, \tag{4.48}$$

labeled R_1, R_2, and R_3, respectively. The eigenvalues of the linearized system in the neighborhood of each equilibrium are: near R_1, $\lambda = \{4.1760 \times 10^7, 2.3523 \times 10^7\}$ s^{-1}; near R_2, $\lambda = \{7.1039 \times 10^5, -4.6413 \times 10^6\}$ s^{-1}; and near R_3, $\lambda = \{-1.9129 \times 10^5, -1.7295 \times 10^7\}$ s^{-1}. R_3 is the physical equilibrium sink, while the non-physical R_1 and R_2 are of source and saddle type, respectively; we find that R_2 is a SIM-BIC. The second branch of the SIM originates at a SIM-BIC at $z \to +\infty$, I_1. We focus our analysis on the SIM that connects R_2 to R_3. Figure 4.15(a) shows the physically realizable region shaded grey, individual rate of change vectors as arrows, system trajectories as thin green lines, and the SIM's two branches as bold red lines. In this system we see a disparity in the two reaction time scales, resulting in high curvature of trajectories as they approach the SIM, which is shown in the close-up plot of the SIM in Figure 4.15(b).

We now evaluate the Galerkin projection to predict the effects of diffusion across finite length scales. Similar to the results from the example in Section 4.1.1, this system retains the spatially homogeneous equilibria and gains (among others) pairs of equilibria, $\hat{R}_{2,m}$, which bifurcate from the R_2 equilibria at integer multiples of a critical length scale,

$$\ell_c = \pi \sqrt{\frac{\mathcal{D}}{\lambda_{0,1}^{e:R2}}} = 139.5 \; \mu m. \tag{4.49}$$

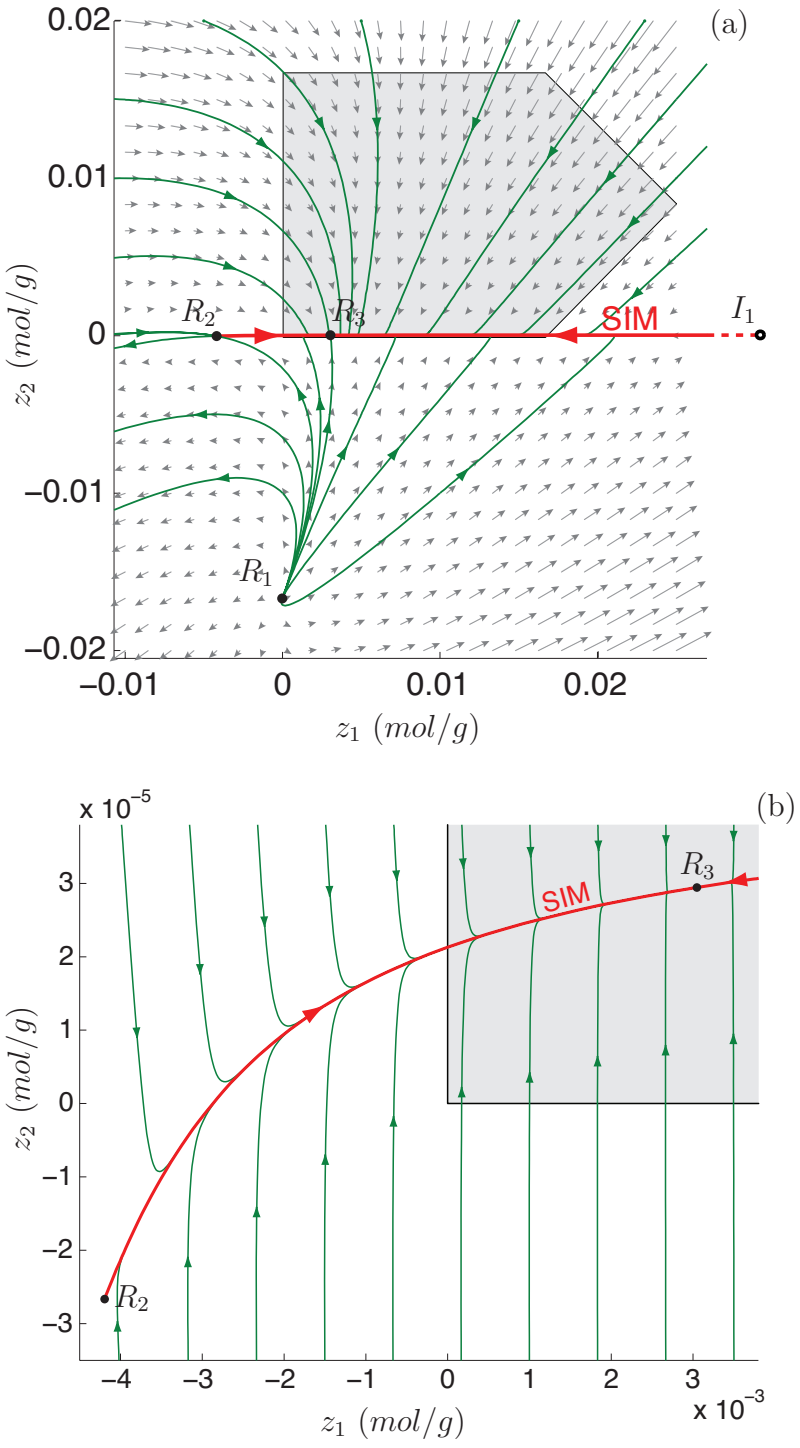

Figure 4.15. The spatially homogeneous SIM for the Zel'dovich mechanism.

This critical length scale is the domain length at which the $m = 1$ diffusion time scale equals the unstable reaction time scales at R_2; this once again demonstrates that diffusion processes can couple chemical time scales to length scales: $\ell_c = \pi\sqrt{\mathcal{D}\tau_0}$. The bifurcations at ℓ_c are of supercritical pitchfork type, where $\hat{R}_{2,m}$ are only real for domain lengths longer than $m\ell_c$. Linear analysis in the neighborhood of $\hat{R}_{2,m}$ reveals each equilibrium has m positive eigenvalues; in the neighborhood of R_2 there are m positive eigenvalues when the domain length is between $(m-1)\ell_c < \ell < m\ell_c$. We note that R_2 will have a zero eigenvalue for domains that are an integer multiple of ℓ_c as an eigenvalue changes from negative to positive; these zero eigenvalues correspond to the bifurcations. This can be seen for $m = 1$ in Figure 4.16, which shows the time scales in the neighborhoods of R_2 and R_3 as a function of domain length, for the $m = 0$ and $m = 1$ modes. For the $m = 1$ time scales,

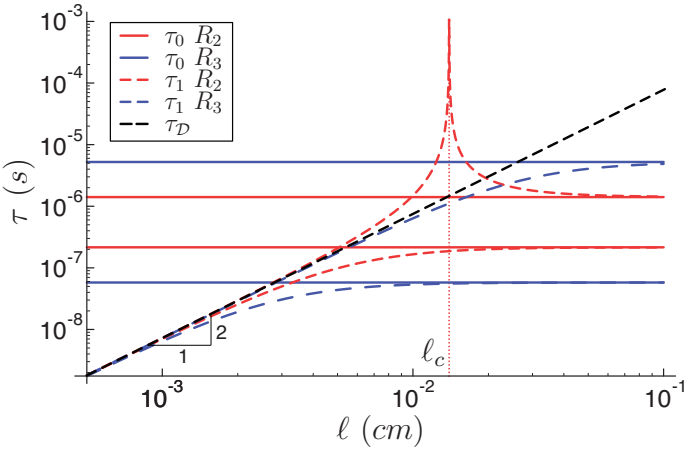

Figure 4.16. Local time scales of R_2 and R_3 for the Zel'dovich mechanism.

we see that short domain lengths are dominated by the diffusion contribution, while long domain lengths are dominated by the reaction contribution. Where the transition occurs, there is a singularity associated with the zero eigenvalue and the bifurcation at R_2; this occurs at $\ell = \ell_c$. Similar results for larger values of m occur at subsequent bifurcations. To evaluate the quality of the Galerkin projection, a convergence study was performed. The convergence rates for the $\hat{R}_{2,1}$ equilibria are similar to those shown in Figure 4.3: for short domain lengths, $\ell \sim \mathcal{O}(\ell_c)$, the approximation converges rapidly, while for longer domain lengths, $\ell > \ell_c$, it converges more slowly.

We now examine the dynamics of the reaction-diffusion system at five length scales, $\ell = 8.96\ \mu m$, $22.4\ \mu m$, $56\ \mu m$, $140\ \mu m$, and $350\ \mu m$, in the $M = 1$ truncation of the Galerkin projection. For $\ell = 8.96\ \mu m$, which is significantly less than ℓ_c, the diffusion time scales are much faster than all of the reaction time scales. This is seen when we examine the eigenvalues in the neighborhood of R_2, $\lambda = \{7.1039 \times 10^5, -4.6413 \times 10^6, -1.7140 \times 10^8, -1.7675 \times 10^8\}\ s^{-1}$. This leads to a system that essentially behaves like a spatially homogeneous system, which is demonstrated in Figure 4.17(a), where the initial spatial inhomogeneities decay rapidly, resulting in the spatially homogeneous reaction which dictates the long time dynamics.

For $\ell = 22.4\ \mu m$, which is still much less than ℓ_c, the diffusion time scales are still faster than all of the reaction time scales, which is evident when examining the eigenvalues in the neighborhood of R_2, $\lambda = \{7.1039 \times 10^5, -4.6413 \times 10^6, -2.6828 \times 10^7, -3.2179 \times 10^7\}\ s^{-1}$. Diffusion causes the spatial inhomogeneities to decay before substantial reaction occurs; however, as seen in Figure 4.17(b), some reaction processes occur before diffusion has removed the majority of the spatial

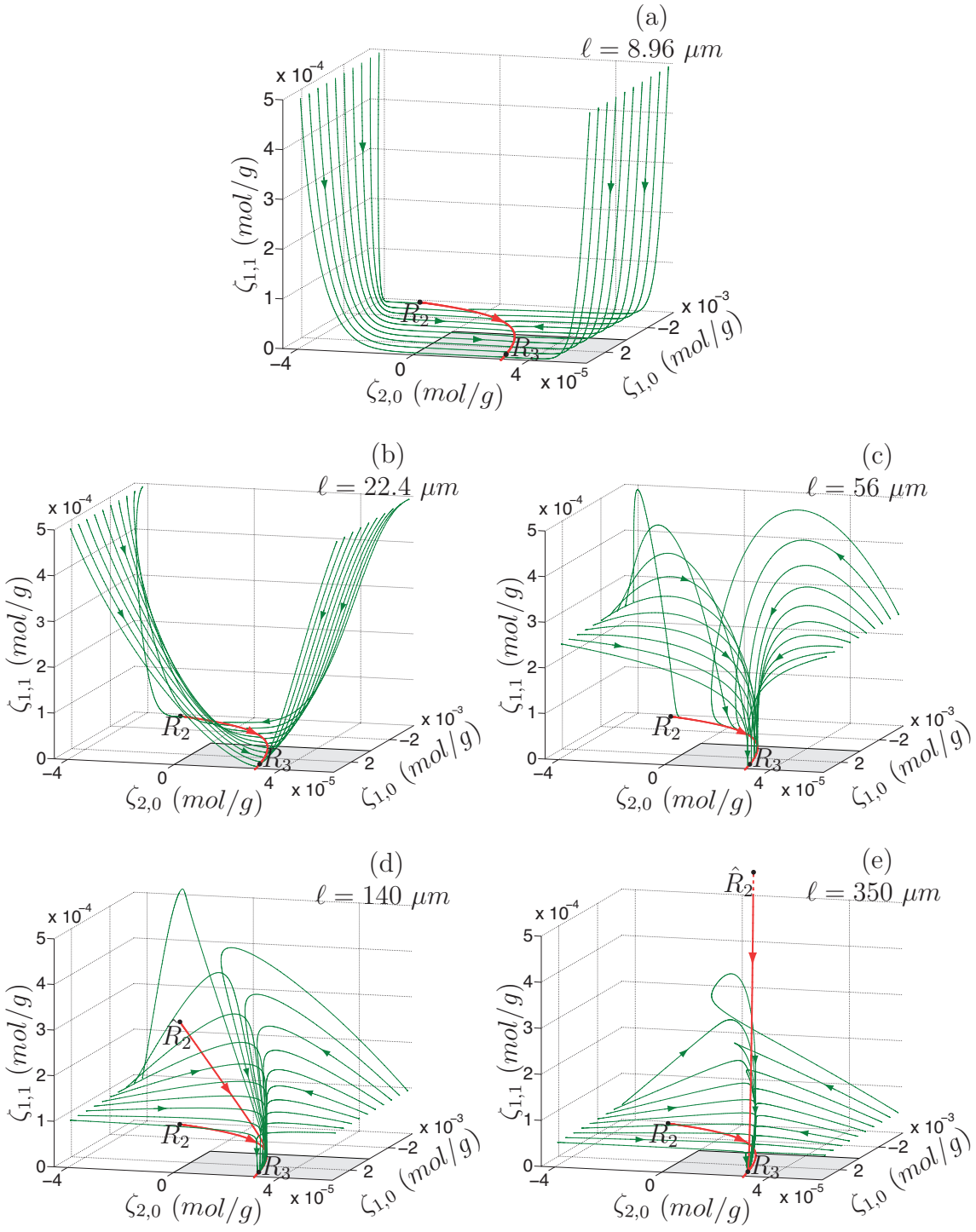

Figure 4.17. $M = 1$ Galerkin projection phase space for the Zel'dovich mechanism at various ℓ.

inhomogeneities. While the reaction mechanism and spatially homogeneous SIM dictate the long time dynamics, diffusion plays a bigger role in the approach to the SIM.

The next length scale, $\ell = 56\ \mu m$, is still less than ℓ_c; however, the fundamental diffusion time scale is now marginally slower than the fast reaction time scales in the neighborhoods of the R_2 and R_3 equilibria; the eigenvalues at R_2 are $\lambda = \{7.1039 \times 10^5,\ -4.6413 \times 10^6,\ -3.6957 \times 10^6,\ -9.0474 \times 10^6\}\ s^{-1}$. This system no longer behaves like a spatially homogeneous system since both reaction and diffusion are acting on the same time scales; however, the slowest dynamics are still captured by the spatially homogeneous SIM since reaction remains the slowest time scale. This is seen in Figure 4.17(c), where the initial spatial inhomogeneities do not decay onto the spatially homogeneous subspace, yet the long time dynamics do collapse onto the spatially homogeneous SIM.

Consider $\ell = 140\ \mu m$, which is just slightly longer than ℓ_c; therefore, at R_2 there are now two positive eigenvalues, $\lambda = \{7.1039 \times 10^5,\ -4.6413 \times 10^6,\ 5418.9,\ -5.3463 \times 10^6\}\ s^{-1}$. The bifurcated equilibrium, $\hat{R}_{2,1}$, is now real and has only one positive eigenvalue, $\lambda = \{7.2371 \times 10^5,\ -4.6078 \times 10^6,\ -10540,\ -5.4259 \times 10^6\}\ s^{-1}$. We predict changes in the slow dynamics of the system, as is evident in Figure 4.17(d). For each of the shorter domain lengths, the fast diffusion causes the spatial inhomogeneities to decay rapidly enough that the spatially homogeneous SIM dictates the long time dynamics of the system; however, at $\ell = \ell_3$, the spatial inhomogeneities persist through the duration of both reaction time scales. The diffusion-modified one-dimensional SIM for this length scale is shown in Figure 4.17(c); however, due to the similarities of the slow reaction and slow diffusion time scales, the long time dynamics of the system are likely better captured by

a two-dimensional manifold. As the amplitudes of modes with fast time scales decay, the trajectories relax onto a vertical sheet, where slow reaction and slow diffusion both dictate the dynamics as the trajectory proceeds toward equilibrium.

For the longest length scale considered, $\ell = 350\ \mu m$, the diffusion time scale of the fundamental Fourier mode is significantly slower than both reaction time scales. We see in Figure 4.17(e) that the bifurcated equilibrium, $\hat{R}_{2,1}$, has become more spatially inhomogeneous, and the system's dynamics reflect this change in trajectories with spatial variations that persist longer in the approach to equilibrium. There are still two unstable eigenvalues at R_2, $\lambda = \{7.1039 \times 10^5, -4.6413 \times 10^6, 5.9760 \times 10^5, -4.7541 \times 10^6\}\ s^{-1}$, and one unstable eigenvalue at $\hat{R}_{2,1}$, $\lambda = \{9.3244 \times 10^5, -4.2979 \times 10^6, -2.1765 \times 10^5, -1.3993 \times 10^7\}\ s^{-1}$. Similar to the simple reaction mechanism, the diffusion-modified SIM appears to have the trajectories collapse onto it more than in the $\ell = 140\ \mu m$ case, but again requires more Galerkin modes to provide enough spatial resolution.

In Figure 4.18 we see the evolution of the amplitudes at two extreme domain lengths, $\ell = 8.96\ \mu m$ (a,b) and $\ell = 350\ \mu m$ (c,d), calculated in the $M = 25$ Galerkin projection.

The initial conditions for each are polynomials scaled to each domain length: $z_1^*(x) = (1.6 \times 10^{-2} mol/g)(2(x/\ell)^3 - (x/\ell)^6)$ and $z_2^*(x) = (1.6 \times 10^{-2} mol/g)(2(1 - x/\ell)^3 - (1 - x/\ell)^6)$. On the left, Figure 4.18(a,c) shows the evolution of the amplitudes of NO (red lines) and N (blue lines), both spatially homogeneous (bold lines) and inhomogeneous (dashed lines). The spatial approximations of NO evolution, reconstructed from Eq. (3.4), are shown on the right, Figure 4.18(b,d). Changes in the spatially homogeneous amplitudes in Figure 4.18(a,c) show the fast and slow reaction time scales, which occur at approximately $\tau_{1,0} = 5.8 \times 10^{-8}\ s$

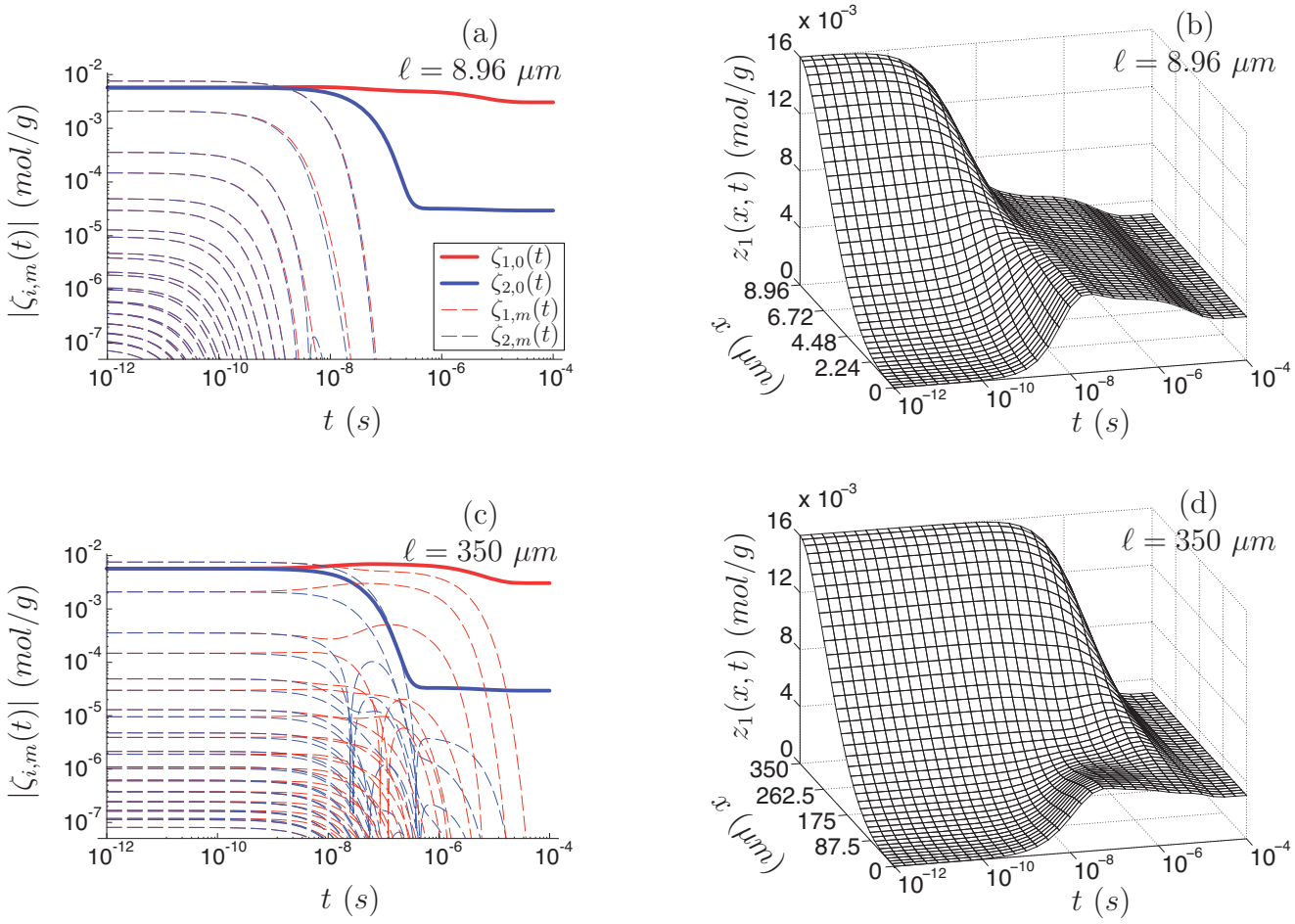

Figure 4.18: Amplitudes and spatial reconstruction of Zel'dovich mechanism species evolution

and $\tau_{2,0} = 5.2 \times 10^{-6}\ s$. The diffusion time scales have drastic changes on the decay rate of the spatial inhomogeneity that is dependent on length: in the $\ell = 8.96\ \mu m$ case, the diffusion time scale of the $m = 1$ mode, $\tau_{\mathcal{D},1} = 5.8 \times 10^{-9}\ s$, is the fastest, which causes all spatial inhomogeneities to decay before either reaction time scale; in the $\ell = 350\ \mu m$ case, the $m = 1$ diffusion time scale, $\tau_{\mathcal{D},1} = 8.9 \times 10^{-6}\ s$, is the slowest, and large spatial inhomogeneities persist until the slow reaction commences. The effects of the various diffusion time scales are also apparent in the spatial reconstruction: for $\ell = 8.96\ \mu m$, diffusion causes the spatial inhomogeneities to decay rapidly, and the long time dynamics are governed by reaction only; for $\ell = 350\ \mu m$, the long time dynamics display both reaction and diffusion processes.

We see that for domains that are shorter than the critical length scale, spatial inhomogeneities decay more rapidly than the amplitude of the spatially homogeneous mode with slow reaction time scale, and the spatially homogeneous SIM describes the long time dynamics. For domains that are longer than the critical length scale, diffusion time scales are slower than the slow reaction time scale; therefore, in these longer domains, the long time dynamics display spatial inhomogeneities, and the spatially homogeneous SIM is no longer appropriate to use as a reduction method.

4.1.3.2 Adiabatic

In this section we examine the closed Zel'dovich reaction mechanism of Section 4.1.3 in the adiabatic isobaric limit. The species evolution equation for this system is

$$\rho \frac{\partial Y_i}{\partial t} = \bar{\mathsf{M}}_i \dot{\omega}_i(Y_n, T) - \frac{\partial j_i}{\partial x}, \text{ for } i, n \in [1, N], \tag{4.50}$$

where we allow temperature, T, to vary such that there is no heat flux into or out of the system (the enthalpy of the system remains constant). The energy equation is

$$\rho \frac{\partial h}{\partial t} + \frac{\partial j^q}{\partial x} = 0, \tag{4.51}$$

where h is the enthalpy and j^q is the diffusive energy flux. We model homogeneous Neumann boundary conditions for the species,

$$\left.\frac{\partial Y_i}{\partial x}\right|_{x=0} = \left.\frac{\partial Y_i}{\partial x}\right|_{x=\ell} = 0, \quad \text{for } i = 1, \ldots, N, \tag{4.52}$$

and the temperature,

$$\left.\frac{\partial T}{\partial x}\right|_{x=0} = \left.\frac{\partial T}{\partial x}\right|_{x=\ell} = 0. \tag{4.53}$$

The constitutive equation for the heat flux is

$$j^q = -k \frac{\partial T}{\partial x} + \sum_{i=1}^{N} h_i^f j_i^m, \tag{4.54}$$

where k is the constant thermal conductivity and h_i^f is the enthalpy of formation of species i. Thus, our homogeneous boundary conditions result in no energy flux at either boundary. The enthalpy is given by the caloric equation of state,

$$h = \sum_{i=1}^{N} Y_i \left(c_{Pi}(T - T^o) + h_i^f \right), \tag{4.55}$$

where c_{Pi} is the constant specific heat at constant pressure of species i, and $T^o = 300\ K$ is the reference temperature.

Following Lam and Bellan [101], we extend the Shvab-Zel'dovich reduction from Section 3.1.3.1 for adiabatic systems. For this reduction, we assume our

system has a constant mixture specific heat,

$$c_P = \sum_{i=1}^{N} Y_i c_{Pi}. \tag{4.56}$$

A constant mixture specific heat is typically the result of the assumption of a single temperature-independent constant specific heat for all species; however, in systems with only bimolecular reactions, a constant mixture specific heat can also be realized. We evaluate the limit where the Lewis number is unity,

$$Le \equiv \frac{k}{\rho c_P \mathcal{D}} = 1. \tag{4.57}$$

This demands that mass and energy diffuse at the same rate, which is a reasonable assumption since both are driven by molecular collisions in gas flames.

Evaluating the time derivative of enthalpy from Eq. (4.55) yields

$$\rho \frac{\partial h}{\partial t} = \rho c_P \frac{\partial T}{\partial t} + \rho \sum_{i=1}^{N} h_i^f \frac{\partial Y_i}{\partial t}, \tag{4.58}$$

and taking the spatial derivative of the diffusive energy flux term from Eq. (4.54) gives

$$\frac{\partial j^q}{\partial x} = -k \frac{\partial^2 T}{\partial x^2} - \rho \mathcal{D} \sum_{i=1}^{N} h_i^f \frac{\partial^2 Y_i}{\partial x^2}. \tag{4.59}$$

We can insert Eqs. (4.58) and (4.59) into Eq. (4.51), cancel like terms, substitute $\mathcal{D} = k/(\rho c_P)$, and collect the spatial and temporal derivatives to reduce the energy equation to a heat equation in enthalpy:

$$\frac{\partial}{\partial t} \underbrace{\left(c_P (T - T^o) + \sum_{i=1}^{N} h_i^f Y_i \right)}_{h} = \mathcal{D} \frac{\partial^2}{\partial x^2} \underbrace{\left(c_P (T - T^o) + \sum_{i=1}^{N} h_i^f T_i \right)}_{h}. \tag{4.60}$$

If the enthalpy is initially spatially homogeneous, and there are no perturbations at the boundary, then Eq. (4.60) can be integrated to form an adiabatic algebraic relation: enthalpy remains constant in both space and time. This constraint can be simplified to yield temperature as a function of the mass fractions of the species,

$$T = \frac{h - \sum_{i=1}^{N} Y_i h_i^f}{c_P} + T^o. \tag{4.61}$$

For this adiabatic system, we shift to a model for Gibbs free energy with a constant specific heat assumption,

$$\bar{\mu}_i^o = \underbrace{\bar{h}_i^f + \bar{c}_{Pi}(T - T^o)}_{\bar{h}_i} - \underbrace{\left(\bar{s}_i^f + \bar{c}_{Pi} \ln\left(\frac{T}{T^o}\right)\right)}_{\bar{s}_i^o} T, \text{ for } i = 1, \ldots, N, \tag{4.62}$$

where $\bar{h}_i$, $\bar{s}_i^f$, and $\bar{s}_i^o$ are the enthalpy, entropy at reference temperature and pressure, and the entropy at reference pressure for species i, respectively. This change is made in order to maintain linear thermodynamic properties outside of the temperature range of the `CHEMKIN` polynomial fit from the thermodynamic database [104]. The values of $\bar{c}_{Pi}$, $\bar{h}_i^f$ and $\bar{s}_i^f$ are calculated using a least squares fit of the `CHEMKIN` polynomial fits and are listed in Table 4.4. Following Section 4.1.3, $i = 1, \ldots, 5$ correspond to the species $\{NO, N, O, O_2, N_2\}$.

The enthalpy is chosen to be $h = 9.0376 \times 10^{10}\ erg/g$, such that the physical equilibrium remains at $T = 4000\ K$ and $\rho = 1.2024 \times 10^{-}4\ g/cm^3$; however, this system is not isochoric, and the density changes as the system evolves.

From the adiabatic constraint we find the temperature to be a rational function

TABLE 4.4

THERMODYNAMIC DATA FOR THE ADIABATIC ZEL'DOVICH MECHANISM

i	$\bar{c}_{Pi}$ $[erg/(mol\ K)]$	$\bar{h}_i^f$ $[erg/mol]$	$\bar{s}_i^f$ $[erg/(mol\ K)]$
1	3.6774×10^8	8.6712×10^{11}	2.0399×10^9
2	2.1120×10^8	4.7223×10^{12}	1.5274×10^9
3	2.1002×10^8	2.4922×10^{12}	1.6130×10^9
4	3.8825×10^8	-5.1316×10^{10}	1.9599×10^9
5	3.6167×10^8	-4.0402×10^{10}	1.8421×10^9

of the reduced specific moles,

$$T = \frac{4214.26 + 71715.0\ z_1 + 173993\ z_2}{1 - 0.565793\ z_1 + 1.13394\ z_2}. \tag{4.63}$$

The numerator defines a line in phase space where the temperature is zero, while the denominator defines a line where temperature is infinite. The temperature profile is shown in Figure 4.19.

With this temperature variation, the exponential terms in $\dot{\omega}_i$ are no longer constant. The reaction source term can be shown to be a polynomial of infinite degree, which admits an infinite number of equilibria and renders simple algebraic techniques and homotopy continuation techniques of `BERTINI` [109] unable to find all roots of the system. This presents a problem, since in order to construct the SIM, we must find the saddle equilibria that connect by heteroclinic

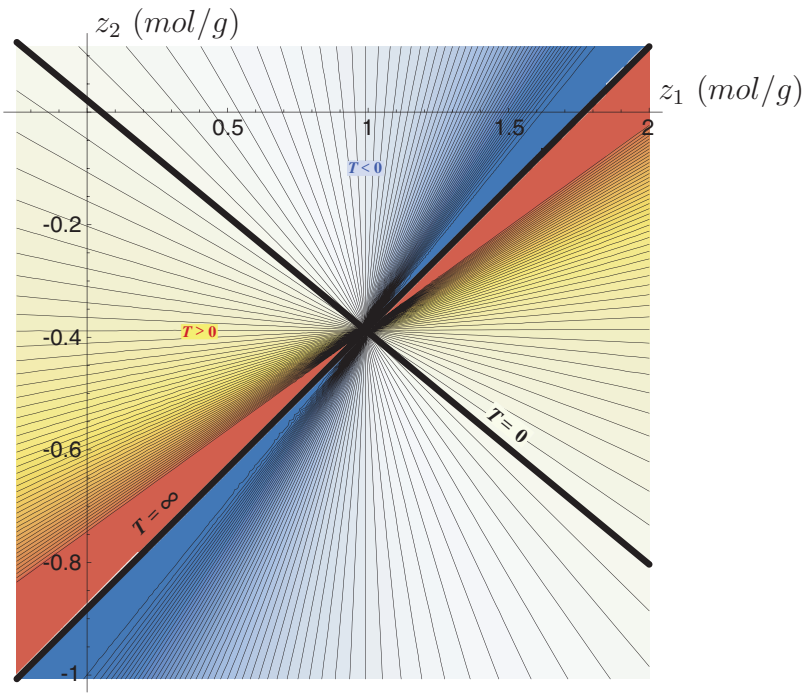

Figure 4.19. Constant enthalpy isotherms in phase space.

orbit to the physical equilibrium sink. The physical equilibrium can be located by a minimization of thermodynamic potentials, among other methods; the system's other equilibria are more difficult to find. The method we employ is to vary the temperature incrementally and solve for the equilibrium of the isothermal system at each temperature. We then check the enthalpy of the isothermal equilibria at each temperature to see if it matches the adiabatic constraint. This is shown graphically in Figure 4.20. Figure 4.20(a) shows the locus of the isothermal equilibria at various temperatures, while Figure 4.20(b) shows the enthalpy of each isothermal equilibrium as a function of temperature. We see in Figure 4.20(a) the equilibria R_1' and R_2' have shifted from their locations in the isothermal system to new locations in the adiabatic system, where we distinguish between the equilibria of the two systems by labeling the adiabatic equilibria with an apostrophe. Notice in Figure 4.20(b) that the enthalpy of the isothermal equilibria does not monotonically increase with temperature. This highlights the fact that additional equilibria are admitted, because the path of each isothermal equilibria could cross the specified enthalpy many more times, yielding additional adiabatic equilibria. Therefore, this technique fails to yield all equilibria of the system; however, for the systems we have examined, the isothermal SIM-BIC at R_2' migrates only a small distance in phase space and remains a SIM-BIC.

For our system the physical equilibrium is located at

$$z_{i,R_3'} = \left\{3.0054 \times 10^{-3}, 2.9862 \times 10^{-5}\right\} \ mol/g. \tag{4.64}$$

There is a shift of approximately 1.4% in the location of the physical equilibrium from the isothermal case. This is due to the change in the equilibrium constants from a different modeling of the Gibbs free energy. The dynamics in the neigh-

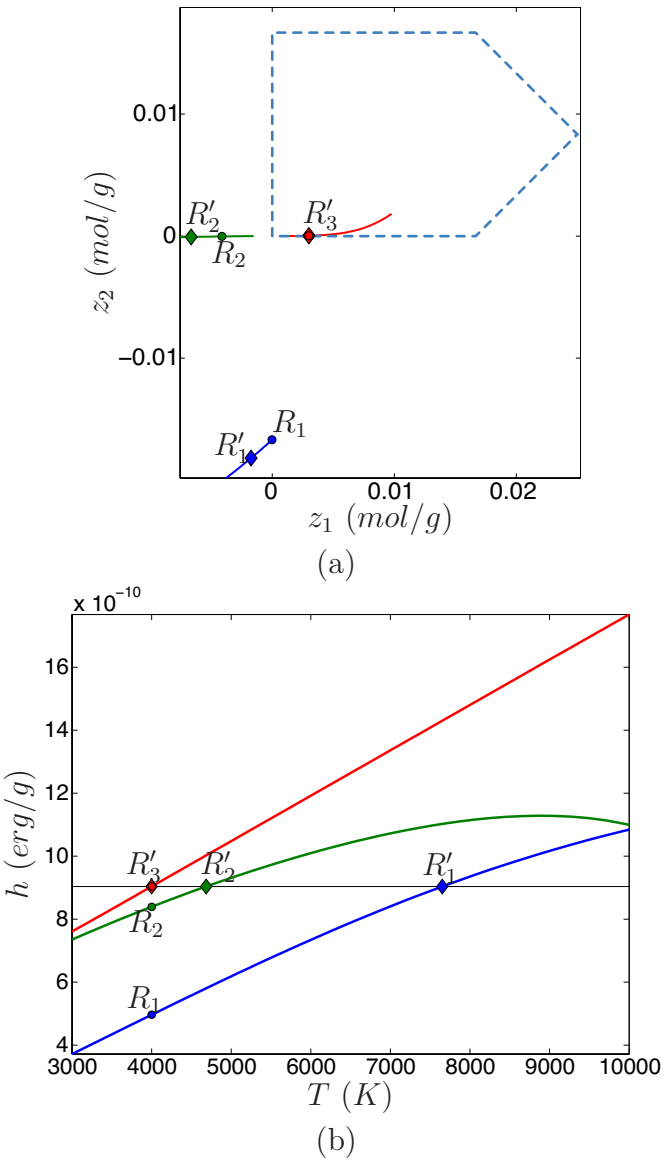

Figure 4.20. Isothermal equilibria for varying temperatures.

borhood of the equilibrium also change slightly. This can be seen by evaluating the eigenvalues of the Jacobian matrix, which are now

$$\lambda_{i,R_3'} = \left\{-1.7628 \times 10^7, -2.2181 \times 10^5\right\} \ 1/s. \tag{4.65}$$

When we evaluate the eigenvalues of the Jacobian of the other adiabatic equilibria, we find that R_1' and R_2' retain their characters as source and saddle, respectively. Also, the heteroclinic orbit from R_2' along the unstable eigenvector still connects to R_3' along its slow eigenvector, making it one branch of the SIM. The other SIM-BIC is no longer infinite, but has shifted to the pole P_1', which is a first order pole. This pole is located where the $z_2 = 0$ axis crosses the line at $T = 0$. We also identify a third SIM-BIC at another first order pole, P_2', which is located where the $z_1 = 0$ axis crosses the $T = 0$ line. A sketch of these poles is provided in Figure 4.21.

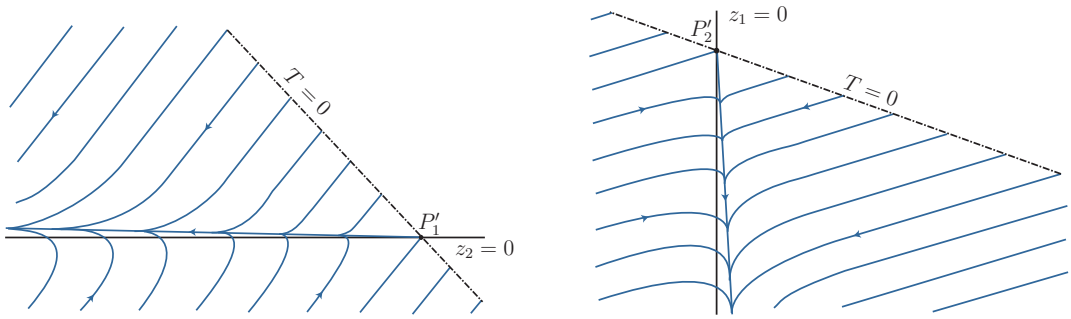

Figure 4.21. Sketches of the dynamics of the system in the positive T neighborhood of poles $P1$ and $P2$.

In Figure 4.22 we see the phase space that includes the entire physical domain. Here we see the shifted equilibria and the SIM branches, which are the heteroclinic

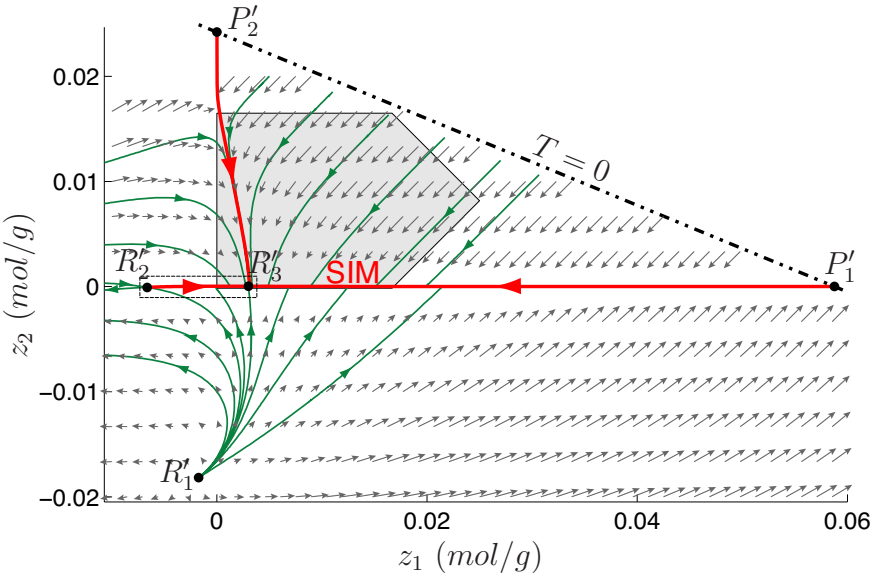

Figure 4.22. The spatially homogeneous SIM branches for the adiabatic Zel'dovich mechanism.

orbits that connect R_2', P_1', and P_2' to R_3'. The dash-dot line identified as $T = 0$ in the upper right corner of the phase space is the location where the enthalpy constraint yields a zero temperature. To the upper right past this line, the temperatures are negative, and the time rate of change of the species mole fraction becomes imaginary; because of this we restrict our evaluation to regions of phase space where $T \geq 0$. In Figure 4.23 we see an expanded view of the branch of the SIM that connects R_2' to R_3.

All three of these SIM branches have negative normal stretching rates and are

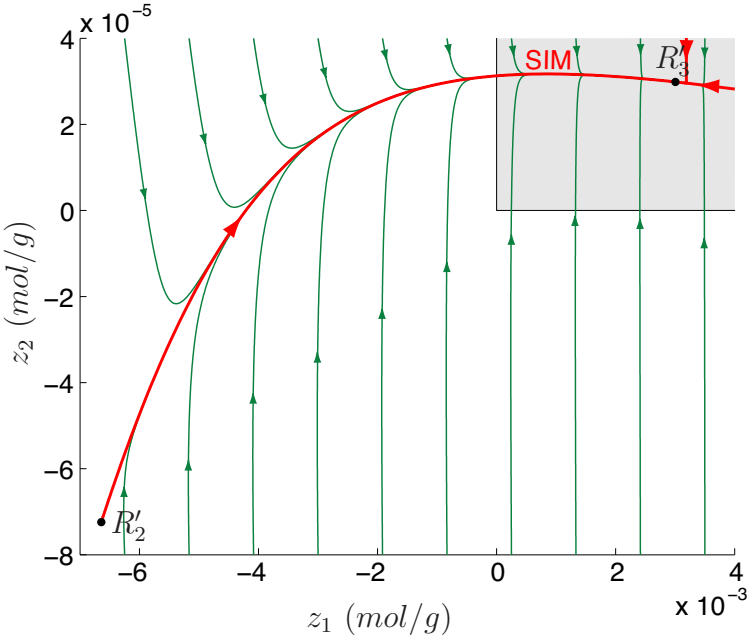

Figure 4.23. The R_2' to R_3' branch of the SIM for the adiabatic Zel'dovich mechanism.

therefore attractive. They are also all in the basin of attraction for the physical equilibrium, R_3'. However, projection onto one of these branches may or may not yield accurate prediction of the system's dynamics, depending on the initial condition and the method used to select which branch to project onto. This example has not only shown the novelty of constructing the SIM for an adiabatic system, but it has also highlighted some of the problems of that arise when systems have multiple SIM branches.

4.2 Summary and conclusions

We have extended the robust method of SIM construction presented by Davis and Skodje [5] to reaction-diffusion systems. Through the use of a Galerkin projection, we analytically isolated the reaction and diffusion contributions to a modified time scale associated with each mode of a particular wavelength. We found a critical length scale at which the slowest diffusion time scale is equal to an unstable reaction time scale of the spatially homogeneous problem. At this critical length scale, a pitchfork bifurcation was predicted. When modeling any system with length longer than the critical value, the canonical slow manifold is no longer the spatially homogeneous SIM. While a one-dimensional diffusion-modified SIM was constructed, it was not endowed with a wide spectral gap in its slowest time scales, thus rendering its utility to be of limited value in a reduction strategy for large scale realistic systems of engineering relevance. We have only examined small reaction mechanisms with a limited number of spatial modes. However, we believe our conclusions will extend to arbitrarily sized systems. When so done, be it via addition of more detailed reactions or more spatial modes, the complexity of the manifold topologies in high-dimensional phase space will rapidly overwhelm

most present analysis strategies. This presents a daunting challenge for rational reduction of realistic combustion systems.

CHAPTER 5

OPEN REACTION-DIFFUSION SYSTEMS

We consider open chemical systems to evaluate the SIM for more diverse systems. Open chemical systems allow for interesting dynamics which most closed systems do not; in open systems there is the possibility of multiple physical equilibria, limit cycles, or chaotic behavior [85], all of which are important for implementing a reduction technique such as the SIM. To consider systems open, we model them as continuously stirred tank reactors (CSTR), where, in addition to reaction and diffusion, there is a feed flow which provides additional reactants and removes products from the system. In this chapter we will evaluate two reaction mechanisms in CSTRs: i) the Gray-Scott reaction mechanism and ii) a hydrogen-air reaction mechanism. Both of these systems display limit cycle behavior when modeled as spatially homogeneous. The Gray-Scott mechanism also displays interesting pattern formation in one- and two-dimensional reaction-diffusion systems.

5.1 Gray-Scott reaction mechanism

We examine the limit cycle behavior of a Gray-Scott reaction-diffusion mechanism [90–92] in a CSTR that has been studied in the literature [12, 81, 93–95].

The Gray-Scott reaction mechanism consists of $J = 2$ irreversible reactions,

$$U + 2V \rightarrow 3V, \tag{5.1a}$$

$$V \rightarrow P, \tag{5.1b}$$

where U, V, and P are the $N = 3$ species. The Arrhenius kinetic reaction rates are:

$$r_1 = k_1 \left(\frac{\rho Y_U}{\bar{\mathsf{M}}_U}\right) \left(\frac{\rho Y_V}{\bar{\mathsf{M}}_V}\right)^2, \tag{5.2a}$$

$$r_2 = k_2 \left(\frac{\rho Y_V}{\bar{\mathsf{M}}_V}\right). \tag{5.2b}$$

We employ Fick's law of diffusion in two spatial dimensions with non-equal diffusion coefficients for each species. Since the system is modeled as a spatially inhomogeneous CSTR, the evolution of species depends on reaction, feed flow, and diffusion,

$$\rho \frac{\partial Y_U}{\partial t} = -\bar{\mathsf{M}}_U r_1 + \frac{\dot{m}}{V}\left(Y_U^f - Y_U\right) - \nabla \cdot \mathbf{j}_U, \tag{5.3a}$$

$$\rho \frac{\partial Y_V}{\partial t} = \bar{\mathsf{M}}_V (r_1 - r_2) + \frac{\dot{m}}{V}\left(Y_V^f - Y_V\right) - \nabla \cdot \mathbf{j}_V, \tag{5.3b}$$

$$\rho \frac{\partial Y_P}{\partial t} = \bar{\mathsf{M}}_P r_2 + \frac{\dot{m}}{V}\left(Y_P^f - Y_P\right) - \nabla \cdot \mathbf{j}_P, \tag{5.3c}$$

where $\dot{m}$ is the mass feed flow rate and V is the volume of the CSTR. The diffusive flux for each species is given by

$$\mathbf{j}_i = -\rho \mathcal{D}_i \nabla Y_i, \text{ for } i = U, V, \tag{5.4a}$$

$$\mathbf{j}_P = -\mathbf{j}_U - \mathbf{j}_V \tag{5.4b}$$

where $\mathcal{D}_i$ are the constant mass diffusivities of species i. We evaluate periodic boundary conditions for each species on a domain length ℓ in both spatial dimensions,

$$Y_i(0,y) = Y_i(\ell,y), \quad \text{and } Y_i(x,0) = Y_i(x,\ell), \text{ for } i = U,V,P, \tag{5.5a}$$

$$\left.\frac{\partial Y_i}{\partial x}\right|_{x=0} = \left.\frac{\partial Y_i}{\partial x}\right|_{x=\ell} \quad \text{and} \quad \left.\frac{\partial Y_i}{\partial y}\right|_{y=0} = \left.\frac{\partial Y_i}{\partial y}\right|_{y=\ell}, \text{ for } i = U,V,P. \tag{5.5b}$$

The mass fractions must sum to unity, $Y_U + Y_V + Y_P = 1$, and each species' molecular mass is identical, $\bar{\mathsf{M}} \equiv \bar{\mathsf{M}}_U = \bar{\mathsf{M}}_V = \bar{\mathsf{M}}_P$. With the assumption that the diffusive flux of the three species sums to zero, $\mathbf{j}_U + \mathbf{j}_V + \mathbf{j}_P = 0$, this system has $\hat{L} = 1$ algebraic constraint that can replace the evolution of Y_P, resulting in $R = N - \hat{L} = 2$ reduced variables: Y_U and Y_V.

We now scale the evolution equations to be dimensionless. Three useful time scales of this problem are the residence time, $\tau_{\mathcal{R}} = V\rho/\dot{m}$, the time scale of the first reaction, $\tau_{k1} = \bar{\mathsf{M}}^2/k_1\rho^2$, and the time scale of the second reaction, $\tau_{k2} = 1/k_2$. There is also a characteristic length which is yet to be determined; we therefore use ℓ/L as a length scale to transform our equations to a domain with dimensionless length L. The diffusion time scales across the domain length are $\tau_{\mathcal{D}U} = \ell^2/\mathcal{D}_U\mathsf{L}^2$ and $\tau_{\mathcal{D}V} = \ell^2/\mathcal{D}_V\mathsf{L}^2$. Using these time scales, we can transform Eqs. (5.3) into dimensionless equations in terms of the parameters: dimensionless feed rate, $\mathsf{F} = \tau_{k1}/\tau_{\mathcal{R}}$; ratio of reaction time scales, $\mathsf{k} = \tau_{k1}/\tau_{k2}$; and dimensionless diffusion coefficients, $\mathsf{D}_U = \tau_{k1}/\tau_{\mathcal{D}U}$ and $\mathsf{D}_V = \tau_{k1}/\tau_{\mathcal{D}V}$. We can also use the time and length scales to transform the coordinates to be dimensionless: $\mathsf{t} = t/\tau_{k1}$, $\mathsf{x} = \mathsf{L}x/\ell$, and $\mathsf{y} = \mathsf{L}y/\ell$. Assuming the inflow conditions of $Y_U^f = 1$, $Y_V^f = 0$, and

$Y_P^f = 0$, Eqs. (5.3) become

$$\frac{\partial Y_U}{\partial \mathsf{t}} = -Y_U Y_V^2 + \mathsf{F}\,(1 - Y_U) + \mathsf{D}_U \left(\frac{\partial^2 Y_U}{\partial \mathsf{x}^2} + \frac{\partial^2 Y_U}{\partial \mathsf{y}^2} \right), \tag{5.6a}$$

$$\frac{\partial Y_V}{\partial \mathsf{t}} = Y_U Y_V^2 - (\mathsf{F} + \mathsf{k})\, Y_V + \mathsf{D}_V \left(\frac{\partial^2 Y_V}{\partial \mathsf{x}^2} + \frac{\partial^2 Y_V}{\partial \mathsf{y}^2} \right), \tag{5.6b}$$

with boundary conditions

$$Y_i(\mathsf{x}, \mathsf{y}) = Y_i(\mathsf{x} + \mathsf{L}, \mathsf{y}) \;\text{ and }\; Y_i(\mathsf{x}, \mathsf{y}) = Y_i(\mathsf{x}, \mathsf{y} + \mathsf{L}), \;\text{ for } i = U, V, \tag{5.7}$$

where $\mathsf{x} \in [0, \mathsf{L})$ and $\mathsf{y} \in [0, \mathsf{L})$, which is the same form that has been studied by others [12, 81, 93, 95].

5.1.1 Spatially homogeneous

We first study the dimensionless Gray-Scott CSTR system from Eqs. (5.6) in the spatially homogeneous limit,

$$\frac{dY_U}{d\mathsf{t}} = -Y_U Y_V^2 + \mathsf{F}\,(1 - Y_U), \tag{5.8a}$$

$$\frac{dY_V}{d\mathsf{t}} = Y_U Y_V^2 - (\mathsf{F} + \mathsf{k})\, Y_V. \tag{5.8b}$$

Varying the dimensionless parameters F and k results in different dynamics in the CSTR. We limit our study to $\mathsf{F} > 0$ and $\mathsf{k} > 0$ for positive feed flow and reaction rates.

By inspection, we find an equilibrium to Eqs. (5.8) at $Y_U = 1$ and $Y_V = 0$,

which we label R_1. By evaluating the Jacobian of the system,

$$J = \begin{bmatrix} -Y_V^2 - \mathsf{F} & -2Y_U Y_V \\ Y_V^2 & 2Y_U Y_V - \mathsf{F} - \mathsf{k} \end{bmatrix}, \tag{5.9}$$

we find eigenvalues in the neighborhood of R_1 to be $\lambda = \{-\mathsf{F}, -\mathsf{F} - \mathsf{k}\}$, which are negative since $\mathsf{F} > 0$ and $\mathsf{k} > 0$. Therefore, R_1 is a real sink for the range of parameters in which we are interested.

We find two additional finite equilibria for Eqs. (5.8): R_2 at

$$Y_U = \frac{\mathsf{F} + \sqrt{\mathsf{F}(\mathsf{F} - 4(\mathsf{F}+\mathsf{k})^2)}}{2\mathsf{F}}, \tag{5.10a}$$

$$Y_V = \frac{\mathsf{F} - \sqrt{\mathsf{F}(\mathsf{F} - 4(\mathsf{F}+\mathsf{k})^2)}}{2(\mathsf{F}+\mathsf{k})}, \tag{5.10b}$$

and R_3 at

$$Y_U = \frac{\mathsf{F} - \sqrt{\mathsf{F}(\mathsf{F} - 4(\mathsf{F}+\mathsf{k})^2)}}{2\mathsf{F}}, \tag{5.11a}$$

$$Y_V = \frac{\mathsf{F} + \sqrt{\mathsf{F}(\mathsf{F} - 4(\mathsf{F}+\mathsf{k})^2)}}{2(\mathsf{F}+\mathsf{k})}. \tag{5.11b}$$

If the value of the argument of the square root in Eqs. (5.10-5.11) is positive, $\mathsf{F}(\mathsf{F} - 4(\mathsf{F}+\mathsf{k})^2) > 0$, then R_2 and R_3 are real; otherwise, they are complex. This indicates a saddle-node bifurcation, which occurs where $\mathsf{F} - 4(\mathsf{F}+\mathsf{k})^2 = 0$ (since we have demanded $\mathsf{F} > 0$). The range of parameters for which R_2 and R_3 are real is shown in gray in Figure 5.1.

The character of the equilibria R_2 and R_3 can change depending on the values of the parameters F and k. Therefore, we evaluate the eigenvalues of the Jacobian

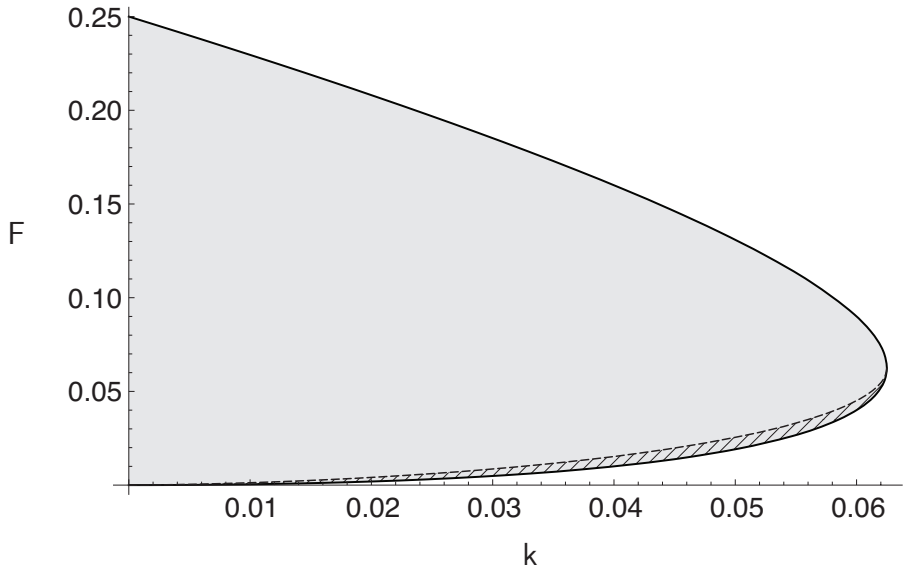

Figure 5.1. Bifurcation locations in the parameter space of the spatially homogeneous Gray-Scott CSTR.

in Eq. (5.9) in terms of the dependent variables and parameters:

$$\lambda = \frac{1}{2}\left(-2\mathsf{F} - \mathsf{k} + 2Y_U Y_V - Y_V^2 \pm \sqrt{\mathsf{k}^2 + Y_V^2(-2Y_U + Y_V)^2 - 2\mathsf{k}Y_V(2Y_U + Y_V)}\right). \tag{5.12}$$

In the neighborhood of the equilibrium R_2, we find that both eigenvalues are real (one is negative and one is positive) for the entire range of parameter space where R_2 is real. This means that R_2 has the character of a saddle with one positive eigenvalue. In the neighborhood of the equilibrium R_3, we find that the real parts of both eigenvalues have the same sign throughout the parameter space where R_3 is real. We find a Hopf bifurcation where the real parts of R_3's complex conjugate pair of eigenvalues change sign; this occurs at $\mathsf{F} = \frac{1}{2}\left(\sqrt{\mathsf{k}} - 2\mathsf{k} - \sqrt{\mathsf{k} - 4\mathsf{k}^{3/2}}\right)$, which is shown as a dashed line in Figure 5.1. In the parameter space where $\mathsf{F} < \frac{1}{2}\left(\sqrt{\mathsf{k}} - 2\mathsf{k} - \sqrt{\mathsf{k} - 4\mathsf{k}^{3/2}}\right)$ (shown as a hatched area in Figure 5.1), R_3 is a

source; in the remainder of the parameter space where R_3 is real, it is a sink. While R_3 is a real spiral source there is no guarantee of a stable limit cycle. Pearson [93] finds this to occur only for $\mathsf{k} < 0.035$ for values of F that are marginally less than $\frac{1}{2}\left(\sqrt{\mathsf{k}} - 2\mathsf{k} - \sqrt{\mathsf{k} - 4\mathsf{k}^{3/2}}\right)$, while for $\mathsf{k} > 0.035$, there are unstable limit cycles for values of F that are marginally greater than $\frac{1}{2}\left(\sqrt{\mathsf{k}} - 2\mathsf{k} - \sqrt{\mathsf{k} - 4\mathsf{k}^{3/2}}\right)$. Therefore, this Hopf bifurcation can be either supercritical for $\mathsf{k} < 0.035$ or subcritical for $\mathsf{k} > 0.035$.

We examine the dynamics of the spatially homogeneous Gray-Scott mechanism for three sets of parameters: a) $\mathsf{F} = 2.5{\times}10^{-2}$ and $\mathsf{k} = 5.5{\times}10^{-2}$, b) $\mathsf{F} = 9.16{\times}10^{-3}$ and $\mathsf{k} = 3.1 \times 10^{-2}$, and c) $\mathsf{F} = 4.1 \times 10^{-3}$ and $\mathsf{k} = 2.0 \times 10^{-2}$. Pattern formation in case (a) is described by Pearson [93]. We use the Poincaré sphere projection,

$$\eta_1 = \frac{Y_U}{\sqrt{1 + Y_U^2 + Y_V^2}}, \tag{5.13a}$$

$$\eta_2 = \frac{Y_V}{\sqrt{1 + Y_U^2 + Y_V^2}}, \tag{5.13b}$$

to display the dynamics at infinity; further details on this mapping are found in Appendix E. We identify six equilibria at infinity, which are independent of the parameters F and k. These equilibria's coordinates in the Poincaré sphere mapping and corresponding mass fractions are shown in Table 5.1. The equilibria I_3 and I_6 are both found along the line $Y_V = -Y_U$ in mass fraction space as $Y_U \to +\infty$ and $Y_U \to -\infty$, respectively. Evaluating the character of the infinite equilibria, we find that I_1 and I_4 are saddle-node non-hyperbolic equilibria, I_2 and I_5 are saddles with one positive eigenvalue, and I_3 and I_6 are sources; I_1, I_2, I_4, and I_5 are SIM-BIC candidates.

We show the dynamics for these three sets of parameters in Figure 5.2. The

TABLE 5.1

GRAY-SCOTT INFINITE EQUILIBRIA IN THE POINCARÉ SPHERE MAPPING

	η_1	η_2	Y_U	Y_V
I_1	1	0	$+\infty$	0
I_2	0	1	0	$+\infty$
I_3	$-\sqrt{2}/2$	$\sqrt{2}/2$	$-\infty$	$+\infty$
I_4	-1	0	$-\infty$	0
I_5	0	-1	0	$-\infty$
I_6	$\sqrt{2}/2$	$-\sqrt{2}/2$	$+\infty$	$-\infty$

left column shows the Poincaré sphere mapping of the phase space, and the right column shows the mass fraction phase space. Similar to previous phase space figures, the physical domain is shaded in gray, SIM branches are bold red, additional heteroclinic orbits are bold blue, and other trajectories are thin green; additionally, stable limit cycles are shown in magenta and unstable limit cycles are shown in cyan.

For case (a), the only physical equilibrium is R_1. For this case there are four branches of the SIM, one starting at each I_1, I_2, I_4, and I_5, which are shown in Figure 5.2(a). The SIMs which originate at I_1 and I_5 are never physical, so they can be disregarded when implementing a reduction technique. The SIMs originating from I_2 and I_4 both have regions which are physical and must be considered to obtain an accurate reduction technique. Neighboring trajectories collapse onto both of these branches of the SIM.

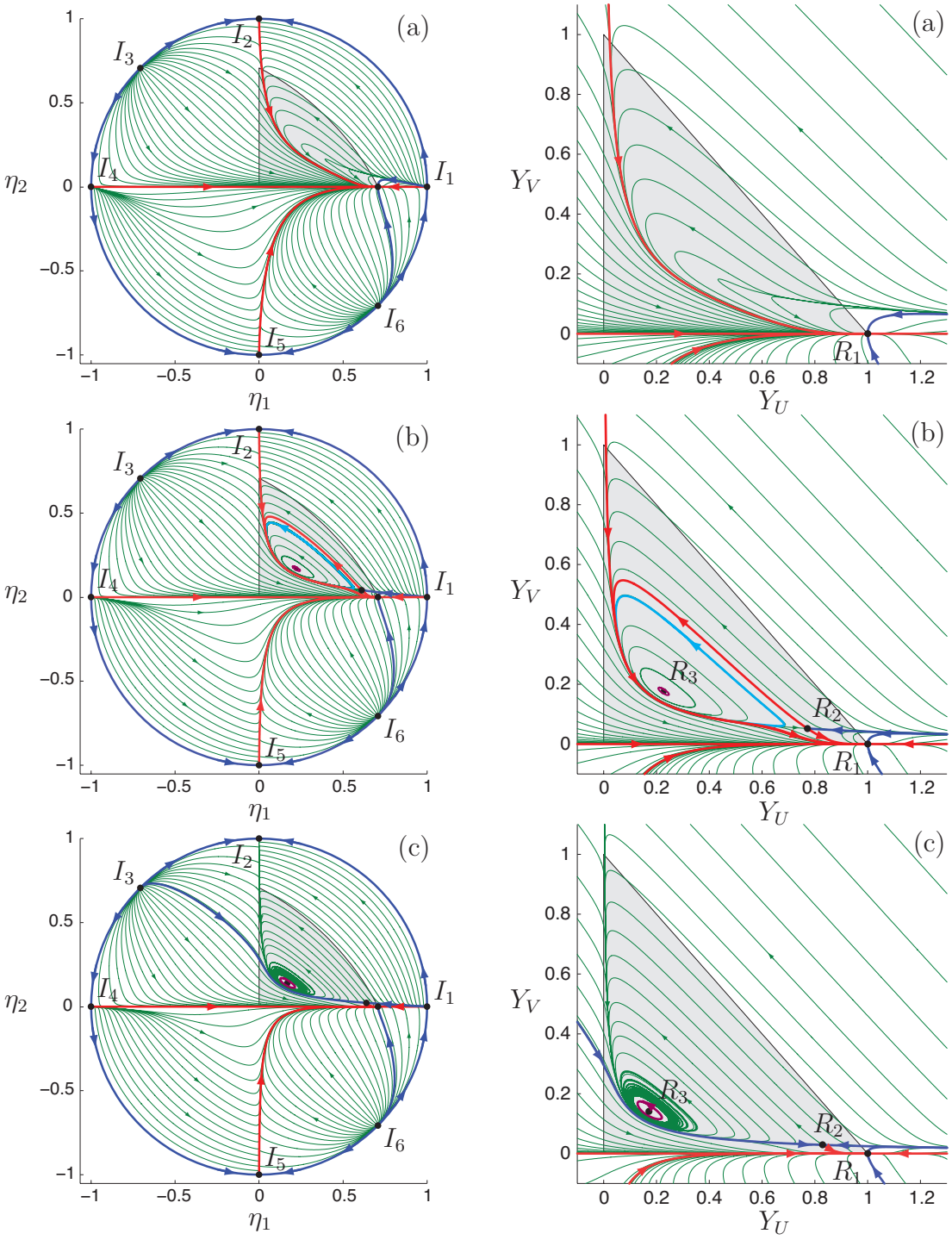

Figure 5.2. Poincaré sphere projection and mass fraction phase spaces of the spatially homogeneous Gray-Scott system.

Figure 5.2(b) shows there are now three physical equilibria, R_1, R_2, and R_3. Again, the SIMs which originate at I_1 and I_5 are never physical and can be disregarded. We identify another SIM-BIC at R_2, and we find two additional branches of the SIM; these branches originate along the unstable eigenvector of R_2 in either direction. Along one SIM branch from R_2, whose initial rate of change has Y_U increasing and Y_V decreasing, the species follow a direct path through phase space to R_1. Along the other branch from R_2, the species evolve further away from R_1, and approach the SIM branch between I_2 and R_1 before decaying to the physical equilibrium, R_1. For the set of parameters in case (b), we find four heteroclinic orbits that meet our criteria to be SIM branches and have portions in the physical domain; they all must be considered.

For the parameters of case (b), there are also two limit cycles: an inner stable limit cycle encompassing the spiral source at R_3, and an outer unstable limit cycle encompassing the stable limit cycle. The unstable limit cycle can be identified by integrating backward in time, since it stable in reverse time. The outer unstable limit cycle defines the boundary of the basin of attraction of the inner limit cycle. A sketch of these limit cycles is provided in Figure 5.3, where the growth and decay away from and toward the limit cycles is exaggerated for clarity.

When we evaluate the system with the parameters from case (b) and initial conditions $Y_U = 0.325$ and $Y_V = 0.290$, we predict the long time limit of the mass fractions will display oscillations, since the initial conditions are within the basin of attraction of the stable limit cycle; however, if we use a projector onto any of the branches of the SIM, $\mathcal{P}(Y_i)$, the long time dynamics will not be accurately predicted. This is shown in Figure 5.4, with a phase space plot on the left and a time evolution plot on the right. In the phase space, the initial conditions are

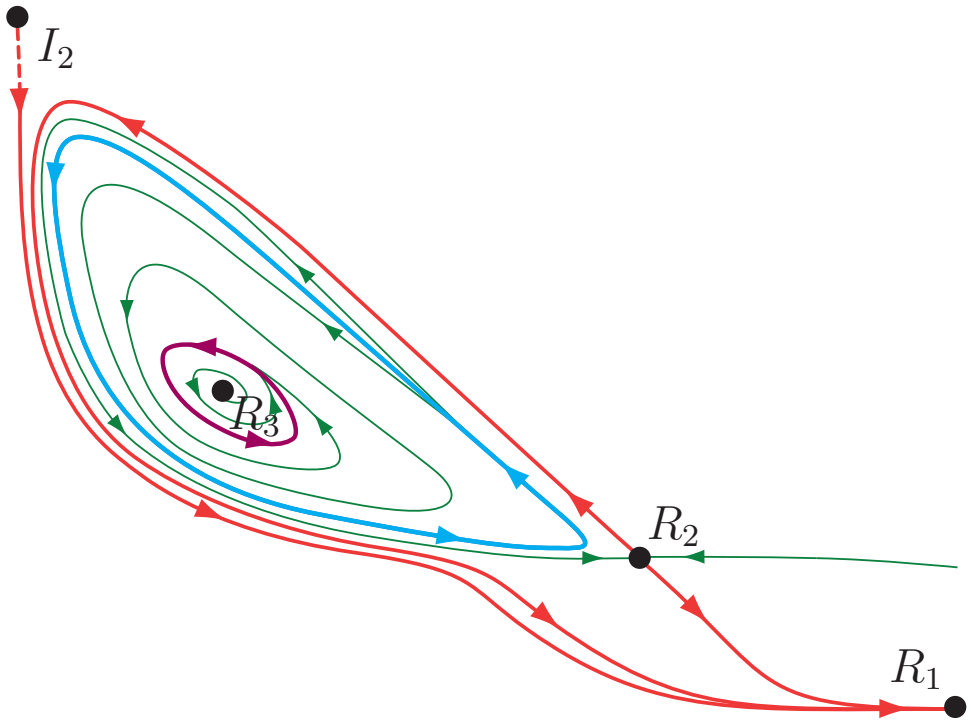

Figure 5.3. Sketch of the stable and unstable limit cycles in the spatially homogeneous Gray-Scott system with $\mathsf{F} = 9.16 \times 10^{-3}$ and $\mathsf{k} = 3.1 \times 10^{-2}$.

indicated with a cross, the time integrated solution is shown as a green line, the projection onto the SIM branch that connects I_2 to R_1 is shown as a black dashed line, the SIM is shown as a red line, and the basin of attraction of the stable limit cycle is shown as an area hatched with gray lines. Figure 5.4 shows the error incurred from projecting the dynamics across the boundary of the basin of attraction. In the time evolution plot, we see the governing equations predict a solution that decays to a stable limit cycle; however, the solution projected onto the SIM, while initially relatively accurate, does not capture the limit cycle behavior, erroneously predicting a decay to the stable equilibrium, R_1. Any initial conditions within the basin of attraction of the limit cycle projected to a SIM that is found using the heteroclinic orbit construction technique will result in an inaccurate prediction; however, a projection onto the attractive limit cycle will accurately predict the long time dynamics of the system. For this reason we consider stable limit cycles to be branches of the SIM, meaning that case (b) has five physical SIM branches for consideration in a reduction technique.

In case (c), shown in Figure 5.2(c), there are still the three physical equilibria, R_1, R_2, and R_3, and R_2 is again a SIM-BIC. For these parameters, however, I_2 is no longer a SIM-BIC, since the trajectory whose initial conditions are along I_2's unstable eigenvector converges to a stable limit cycle, not R_1. This is also the case for one of the trajectories that originates along the unstable eigenvector at R_2; however, the other trajectory from R_2 is still a SIM branch since it connects to R_1 along its slow eigenvector. This SIM branch and the branch that originates from I_4 are the only two physical SIM branches that are constructed using the method of connecting heteroclinic orbits.

Case (c) has one limit cycle, which is stable and encompasses R_3. The bound-

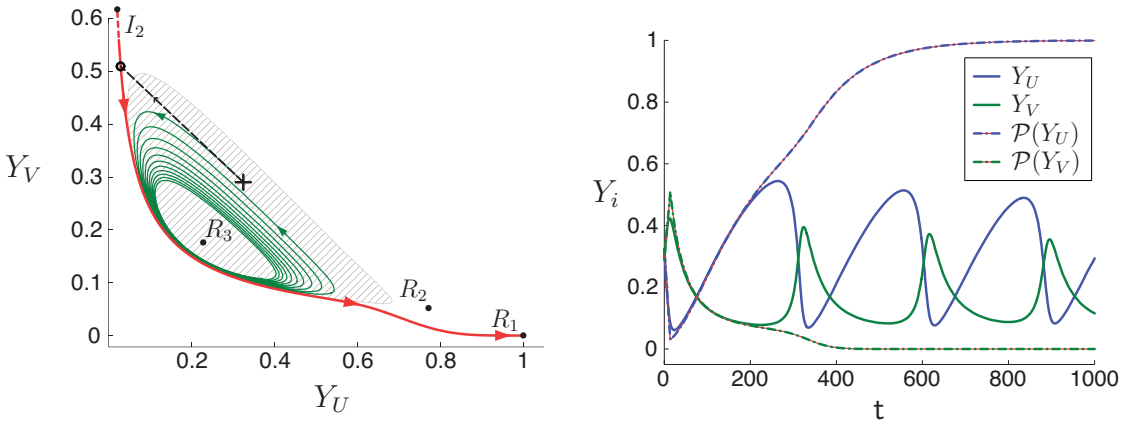

Figure 5.4. Naïve projection onto the SIM in the Gray-Scott system with $\mathsf{F} = 9.16 \times 10^{-3}$ and $\mathsf{k} = 3.1 \times 10^{-2}$.

ary of the basin of attraction for this limit cycle is defined by the two heteroclinic orbits that connect R_2's stable eigenvectors to the infinite equilibria I_1 and I_3 and heteroclinic orbits at infinity from I_1 to I_2 and I_2 to I_3. The long time dynamics of all initial conditions within this boundary will result in oscillatory behavior described by the stable limit cycle encompassing R_3.

This result of having multiple physical SIM branches is not unique to the Gray-Scott CSTR; another simple reaction mechanism in which multiple SIM branches were found is the adiabatic Zel'dovich mechanism, shown in Section 4.1.3.2.

The conclusion from Al-Khateeb et al. [49] that in the $A+A \leftrightharpoons B \leftrightharpoons C$ system (originally presented by Lebiedz [57]), one approach to the physical equilibrium has no unique branch of the SIM, presents a similar issue. This is yet another system that does not have the previously expected two one-dimensional SIM branches, one for each approach to the physical equilibrium along its slow eigenvector.

Having identified multiple branches of the SIM indicates that implementation of a reduction technique using these manifolds will require additional analysis.

In addition to constructing the manifolds, an accurate technique to project onto the various SIMs is necessary. Further analysis would need to identify basins of attraction and could perhaps incorporate a manifold attractiveness metric such as the stretching based metric described by Adrover et al. [10], which is shown in further detail in Appendix F. However, the ability to identify basins of attraction is a daunting task when considering realistic chemical systems whose phase spaces are typically much greater than two-dimensional.

5.1.2 Spatial variations and pattern formation

We return to the full reaction-diffusion system from Eqs. (5.6-5.7), and following Pearson [93], we solve the system on a domain $\mathsf{x} \in [0, \mathsf{L})$ and $\mathsf{y} \in [0, \mathsf{L})$ with periodic boundary conditions, where the dimensionless length and diffusion coefficients are $\mathsf{L} = 2.5$, $\mathsf{D}_U = 2 \times 10^{-5}$, and $\mathsf{D}_V = 10^{-5}$. The governing equations are evaluated on a discrete spatial grid of 256×256 uniformly spaced points; the diffusion operator is modeled using a second order central finite difference operator, and the time evolution is evaluated using the algorithm embodied in `LSODE` [105]. We choose to examine the parameters from case (a) in Section 5.1.1, $\mathsf{F} = 2.5 \times 10^{-2}$ and $\mathsf{k} = 5.5 \times 10^{-2}$. For this set of parameters, our results show pattern formation which is similar to the pattern label as 'γ' in Ref. [93]. We did not find any pattern formation behavior for the other two sets of parameters in Section 5.1.1, which exhibited limit cycles in the spatially homogeneous system.

The mass fraction evolution for this system is shown in Figure 5.5 at six dimensionless times. The initial conditions are $Y_U = 1$ and $Y_V = 0$ for the entire domain, except a small region, $0.3125 \leq \mathsf{x} \leq 0.9375$ and $0.3125 \leq \mathsf{y} \leq 0.9375$, which has the concentration $Y_U = 0.5$ and $Y_V = 0.25$. To break the symmetry of

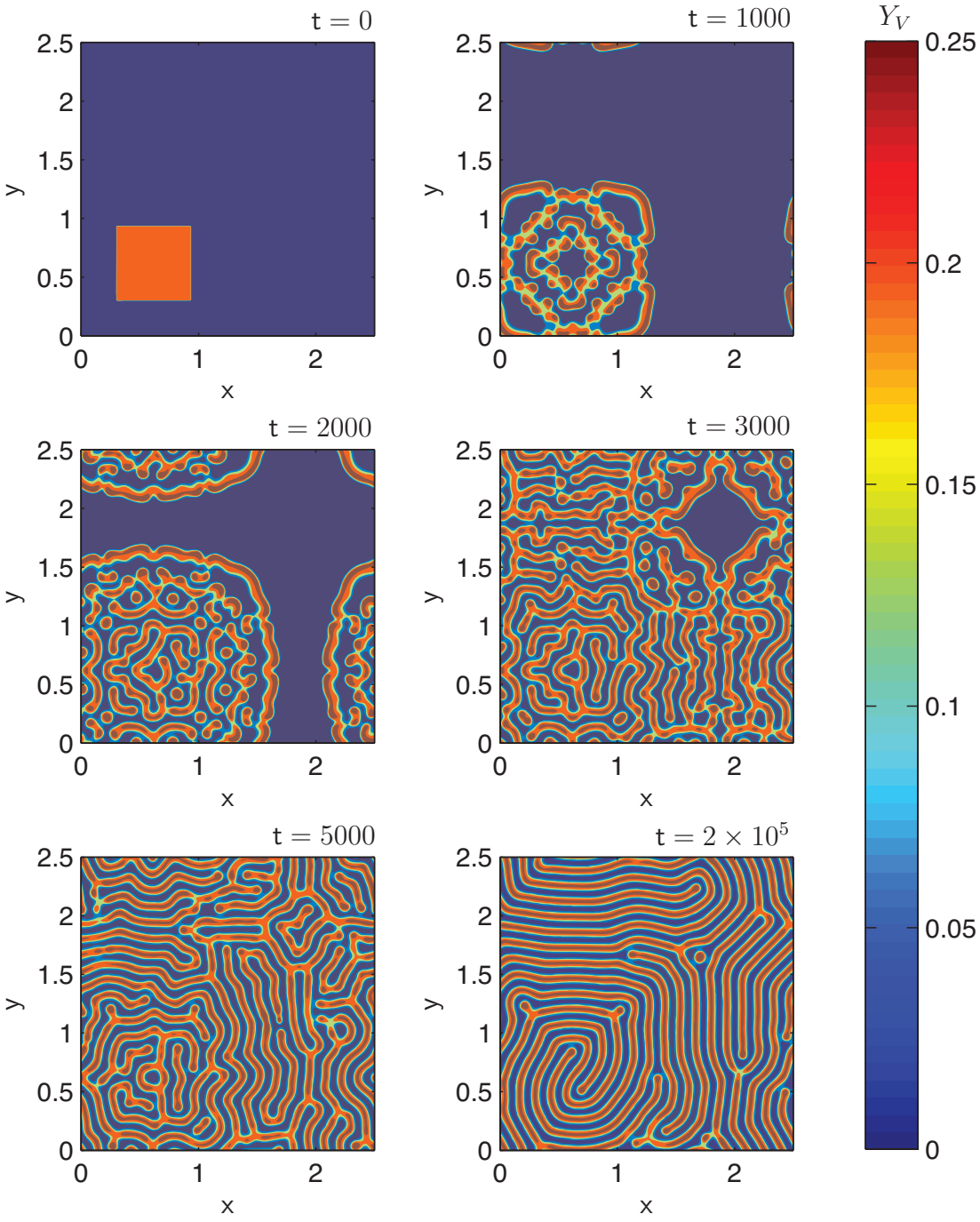

Figure 5.5. Patterns of Gray-Scott system.

the system, the initial conditions at each grid point are perturbed by a random amount, ϵ, which is uniformly distributed between the values of -0.01 and 0.01. As the system evolves, we see predominately striped pattern formation which propagates outward throughout the domain. These patterns encompass the entire domain by $\mathsf{t} = 5000$. The solution at $\mathsf{t} = 5000$ still shows symmetries from the initial condition; as the solution evolves further (by $\mathsf{t} = 2 \times 10^5$), the perturbations in the initial conditions have broken most of those symmetries, and the solution appears more isotropic.

For this analysis we define isotropy in the same sense as isotropic turbulence [106, pp. 89], that is, we call a pattern isotropic if it has global properties (such as amplitudes of directional basis functions), which are essentially invariant under a rotation of coordinate system. So, despite having local structures that display preferred directions, we can still discuss whether the global structure of the pattern has any preferred directions or not.

We analyze the Fourier spectrum of these spatial solutions, which are shown in Figure 5.6. In the right column are contour plots of the amplitudes associated with the corresponding spatial basis functions, labeled by wave number. The amplitudes are the result of a discrete Fourier transform that calculates

$$\zeta_{i,m,n} = \frac{\langle \phi_m(\mathsf{x})\phi_n(\mathsf{y}), Y_i(\mathsf{x},\mathsf{y}) \rangle}{\langle \phi_m(\mathsf{x})\phi_n(\mathsf{y}), \phi_m(\mathsf{x})\phi_n(\mathsf{y}) \rangle}, \text{ for } i = U, V \text{ and } m, n = 0, \ldots, M-1, \quad (5.14)$$

where $\phi_m(\mathsf{x})$ are sine and cosine functions, as we have defined in Appendix A, and M is equal to the number of finite difference points in each direction, which corresponds to the largest basis function that can be resolved in each spatial dimension. Note that the resolved modes do not necessarily correspond to our basis function numbering convention: finite difference schemes with an odd number of points,

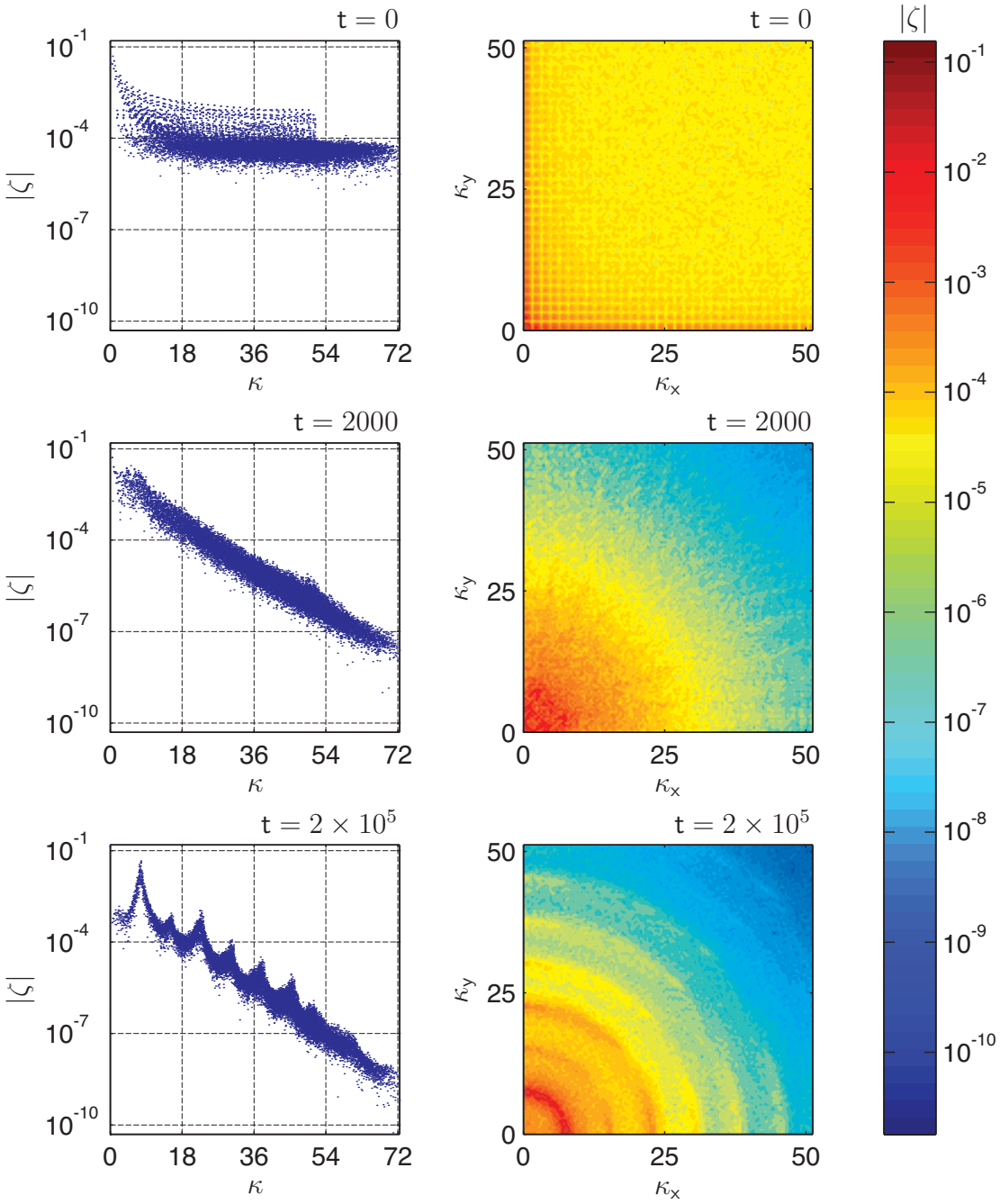

Figure 5.6. Amplitudes as a function of wave number for the Gray-Scott system.

M, will resolve modes $0, \ldots, M-1$; however, finite difference schemes with an even number of points, M, will resolve modes $0, \ldots, M-2, M$. This is because of how the sine and cosine basis functions are evaluated on a discrete evenly spaced grid. Also note that resolving M basis functions only resolves $M/2$ wave numbers since the discrete Fourier transform also contains phase information. The result of the discrete Fourier transform is a set of complex numbers which correspond to the amplitudes of basis functions: the real component corresponds to the cosine functions, and the imaginary component corresponds to the sine functions. The discrete Fourier transform is subject to the aliasing phenomena: higher frequencies' spatial oscillations are represented on the discrete grid as amplitudes of their corresponding lower frequency basis functions, and vice versa. To obtain the final value of amplitudes, the aliased amplitudes of modes above the resolution threshold must be filtered to their corresponding lower frequency. This filtering process can be used to identify directional phase information about the amplitudes of multiple-dimensional discrete Fourier transforms.

The amplitudes displayed in Figure 5.6 ignore phase variations and are shown as the magnitude of the amplitudes for both the sine and cosine basis functions with identical wave numbers, where the wave numbers are defined as

$$\kappa_{\mathsf{x}} = \begin{cases} \frac{m+1}{2\mathsf{L}} & m \in \text{odds} \\ \frac{m}{2\mathsf{L}} & m \in \text{evens}; \end{cases} \tag{5.15}$$

there is an identical relation for the wave numbers of the basis functions in the y-dimension. The contour plots in the right column of Figure 5.6 make the isotropy of the solution at different times noticeable. This is because variations in the amplitudes of each spatial dimension are displayed separately. These spatial wave

number contour plots, however, do not facilitate the identification of a fundamental wave number and higher harmonic modes. We therefore seek to combine the spatial wave numbers into one combined wave number.

Each amplitude of the discrete Fourier transform is associated with the product of a basis function from each spatial direction. The directional basis functions each have a corresponding spectrum of wave numbers given in Eq. (5.15); however, the product of the spatial basis functions (excluding the spatially homogeneous basis functions) have a higher wave number than the wave number from the basis functions in either direction. An example of this is shown graphically in Figure 5.7. The product of two spatial basis functions with wave numbers $\kappa_x = 1/L$ and

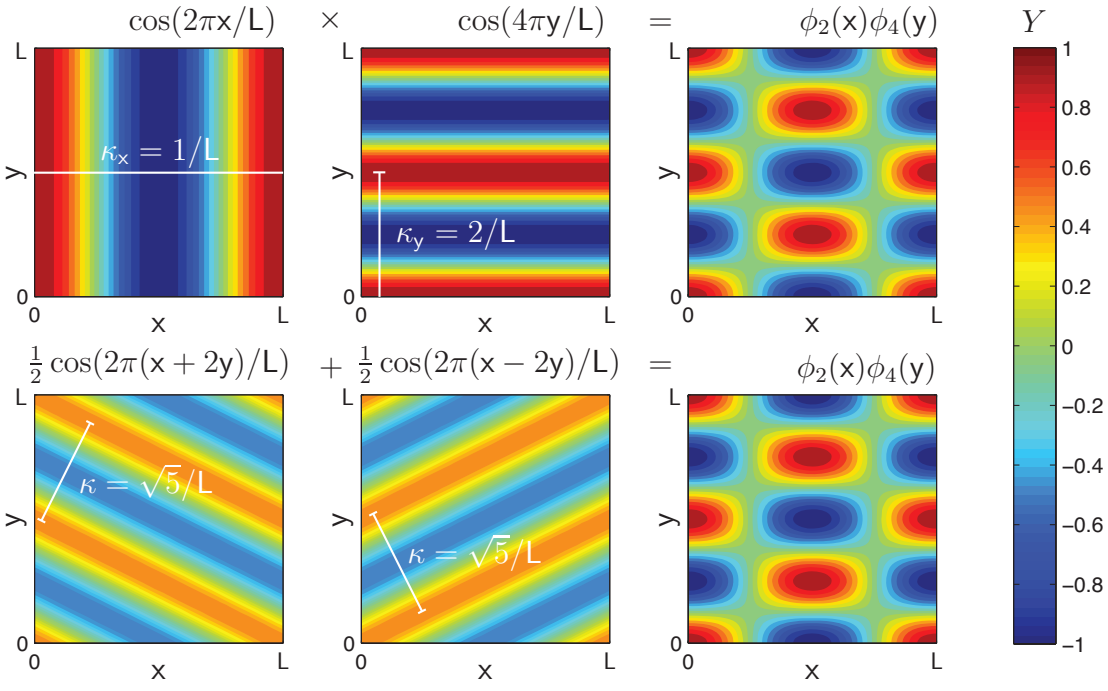

Figure 5.7. Example of isotropic wave numbers.

$\kappa_y = 2/L$, $\cos(2\pi x/L)\cos(4\pi y/L)$, is identical to the sum of cosine functions, each with a wave number of $\kappa = \sqrt{5}/L$, $(\cos(2\pi(x+2y)/L) + \cos(2\pi(x-2y)/L))/2$. The original basis functions are oriented to the orthogonal coordinate system, which makes them an ideal basis; however, the summed cosine functions, despite not being oriented to the coordinate system, show the underlying wave number that is not immediately apparent in the original basis functions. Using this analysis, we find many identical wave numbers that correspond to various directions; therefore, we define an isotropic wave number as $\kappa^2 = \kappa_x^2 + \kappa_y^2$. This allows us to analyze the contour plots of spatial Fourier amplitudes in Figure 5.6 as polar plots, where the angular coordinate corresponds to isotropic patterns, and any radial variations indicates anisotropy.

The initial condition has a highly concentrated spatial structure which gives it high wave numbers throughout κ-space, and high anisotropy. This is particularly noticeable with large amplitudes along the κ_x and κ_y axes. Most of the concentrated spatial structure in the initial condition has decayed by $t = 2000$, and preferred wave numbers are beginning to coalesce into peaks; however, there is still a large amount of anisotropy which can be seen as peaks in the radial lines in the contour plot and as a broad range of amplitudes for each isotropic κ value. Similar to the mass fraction plot, by $t = 2 \times 10^5$ the wave number plot shows a nearly isotropic solution since the contour plot of amplitudes in wave number space for this time has only moderate radial variation. At this large time, the pattern is well formed enough to identify a fundamental wave number of $\kappa = 7.5$, with peaks in the amplitudes at higher mode harmonics of the fundamental wave number also apparent at $\kappa = 15$, 22.5, 30, 37.5, and 45. These wave numbers correspond to periodicity over a dimensionless length of 0.133. This length scale

corresponds to diffusion time scales of $\tau_{\mathcal{D}} = \{45,\ 22.5\}$ for species U and V, respectively. The reaction time scales are dependent on the species concentrations and vary throughout the domain; the reaction time scales at the spatially homogeneous equilibrium, $Y_U = 1$ and Y_V, are $\tau_{R1} = \{12.5,\ 40\}$, which are on the same order of magnitude as the diffusion time scales of the fundamental length scale.

5.1.3 One-dimensional analysis

With the fundamental length of this two-dimensional system identified, we now turn our attention to solutions with diffusion across one dimension. Focusing on one dimension allows us to more easily examine the reaction-diffusion system using the Galerkin projection. Similar to our discussion in Chapter 4, we evaluate a simple Galerkin projection to identify phenomena in the system, and then evaluate a more complex Galerkin projection to evaluate the fidelity of the analysis in the lower-dimensional system. In the simple $M = 1$ projection, we find results that are similar to Marchant [81].

By using this two-term projection, we demand that the solutions have no phase variations. We implement a modified $M = 1$ truncation where our two basis functions are

$$Y_U(x,t) = \zeta_{U,0}(t) + \zeta_{U,2}(t)\cos\left(\frac{2\pi x}{\mathsf{L}}\right), \tag{5.16a}$$

$$Y_V(x,t) = \zeta_{V,0}(t) + \zeta_{V,2}(t)\cos\left(\frac{2\pi x}{\mathsf{L}}\right). \tag{5.16b}$$

We keep the basis function numbering convention from the periodic boundary conditions, but omit the $m = 1$ sine terms in favor of the $m = 2$ cosine terms. In

this projection the evolution of the amplitudes is governed by

$$\frac{d\zeta_{U,0}}{dt} = -\frac{\langle\phi_0, Y_U Y_V^2\rangle}{\langle\phi_0,\phi_0\rangle} + \mathsf{F}(1-\zeta_{U,0}), \tag{5.17a}$$

$$\frac{d\zeta_{U,2}}{dt} = -\frac{\langle\phi_2, Y_U Y_V^2\rangle}{\langle\phi_2,\phi_2\rangle} - \mathsf{F}\zeta_{U,2} + \mathsf{D}_U\left(\frac{2\pi}{\mathsf{L}}\right)^2\zeta_{U,2}, \tag{5.17b}$$

$$\frac{d\zeta_{V,0}}{dt} = \frac{\langle\phi_0, Y_U Y_V^2\rangle}{\langle\phi_0,\phi_0\rangle} - (\mathsf{F}+\mathsf{k})\zeta_{V,0}, \tag{5.17c}$$

$$\frac{d\zeta_{V,2}}{dt} = \frac{\langle\phi_2, Y_U Y_V^2\rangle}{\langle\phi_2,\phi_2\rangle} - (\mathsf{F}+\mathsf{k})\zeta_{V,2} + \mathsf{D}_V\left(\frac{2\pi}{\mathsf{L}}\right)^2\zeta_{V,2}, \tag{5.17d}$$

where the inner products of the cubic terms are derived using the technique described in Appendix B and are given by

$$\frac{\langle\phi_0, Y_U Y_V^2\rangle}{\langle\phi_0,\phi_0\rangle} = \zeta_{U,0}\zeta_{V,0}^2 + \zeta_{U,2}\zeta_{V,0}\zeta_{V,2} + \frac{\zeta_{U,0}\zeta_{V,2}^2}{2}, \tag{5.18a}$$

$$\frac{\langle\phi_2, Y_U Y_V^2\rangle}{\langle\phi_2,\phi_2\rangle} = \zeta_{U,2}\zeta_{V,0}^2 + 2\zeta_{U,0}\zeta_{V,0}\zeta_{V,2} + \frac{3\zeta_{U,2}\zeta_{V,2}^2}{4}. \tag{5.18b}$$

For parameters $\mathsf{F} = 2.5\times10^{-2}$ and $\mathsf{k} = 5.5\times10^{-2}$, Eqs. (5.17) have three spatially homogeneous equilibria that are independent of the domain length: $R_1 = \{1,0,0,0\}$, and the complex conjugate pair R_2 and $R_3 = \{0.5\pm0.07746\mathbf{i}, 0, 0.15625\mp 0.02420\mathbf{i}, 0\}$. We also find six additional spatially inhomogeneous finite equilibria that vary with the domain length; four of these are real for a range of domain lengths. These four equilibria consist of two symmetric pairs; we name them $\hat{R}_4^+$, $\hat{R}_4^-$, $\hat{R}_5^+$, and $\hat{R}_5^-$ since they do not correlate to any spatially homogeneous equilibria. Again, we focus our analysis on $\hat{R}_4^+$ and $\hat{R}_5^+$ and drop the superscript for convenience. There are two saddle node bifurcations, one that occurs at $\mathsf{L} = 0.08674$ and another at $\mathsf{L} = 0.3424$, between which $\hat{R}_4$ and $\hat{R}_5$ are real and non-singular. Their amplitudes are shown in Figure 5.8 as a function of domain length.

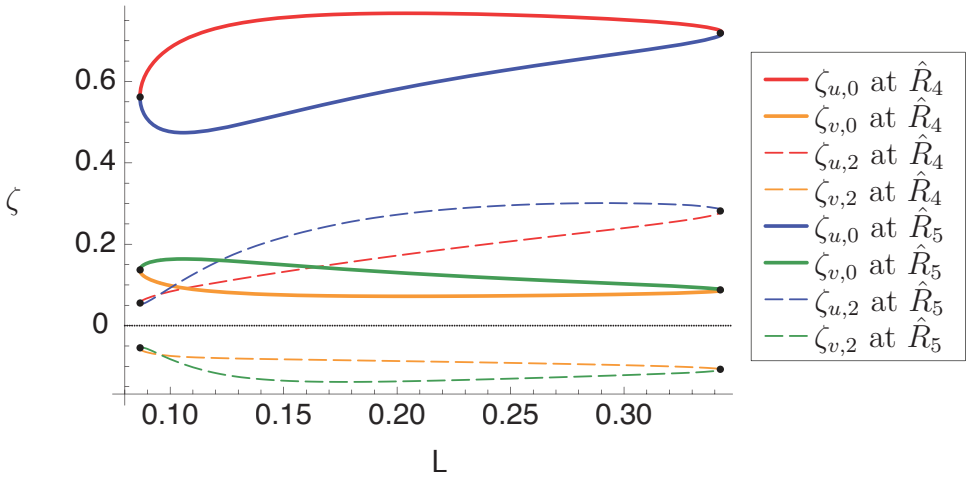

Figure 5.8. Amplitudes of equilibria at the fundamental saddle node bifurcation in $M = 1$ Galerkin projection of the Gray-Scott system.

We analyze the stability of each equilibrium by calculating the eigenvalues of the Jacobian matrix from Eq. (3.51). We find that $\hat{R}_4$ has either one or two unstable eigenvalues, and $\hat{R}_5$ has either zero, one, or two unstable eigenvalues, depending on the domain length.

In the neighborhood of $\hat{R}_5$ for the domain lengths where it is real, all eigenvalues have negative real parts except for one complex conjugate pair. The real part of this complex conjugate pair of eigenvalues changes from positive to negative for a set of domain lengths as shown in Figure 5.9. This indicates the system has two Hopf bifurcations, one at $\mathsf{L} = 0.138$ and the other at $\mathsf{L} = 0.188$.

The fundamental wave formation of the pattern formed in Figure 5.5 can be approximated by the amplitudes of $\hat{R}_5$; however, $\hat{R}_5$ at $\mathsf{L} = 0.133$ is not stable in the $M = 1$ Galerkin projection, indicating that this simple analysis would not accurately predict the structure of a fundamental wave in the pattern shown in Figure 5.5.

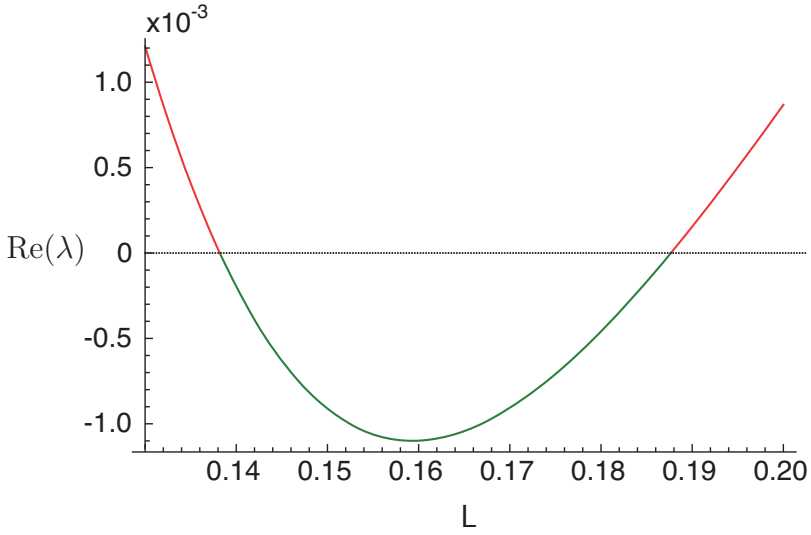

Figure 5.9. Hopf bifurcations of $\hat{R}_5$ in the Gray-Scott $M = 1$ Galerkin projection.

We now examine a larger truncation of the Galerkin projection at $M = 30$ and seek the higher resolution solutions for $\hat{R}_4$ and $\hat{R}_5$ to see if they converge to non-singular equilibria in a system that is spatially resolved.

This truncation includes both sine and cosine terms and therefore allows phase difference in the solutions; this means that any spatially inhomogeneous equilibrium will reside on a one-dimensional manifold of equilibria which have identical amplitudes, but are out of phase with each other. We focus our analysis on the equilibrium solution with $\zeta_{U,1} = 0$ and $\zeta_{U,2} > 0$.

To find $\hat{R}_4$ and $\hat{R}_5$ in this well-resolved truncation, we use their analytical solutions found in the $M = 1$ Galerkin projection as an initial guess at each domain length and use a Newton-Raphson root finder to identify the analogous equilibria. This method yields the equilibria amplitudes for $\hat{R}_4$ and $\hat{R}_5$ which are shown in Figure 5.10.

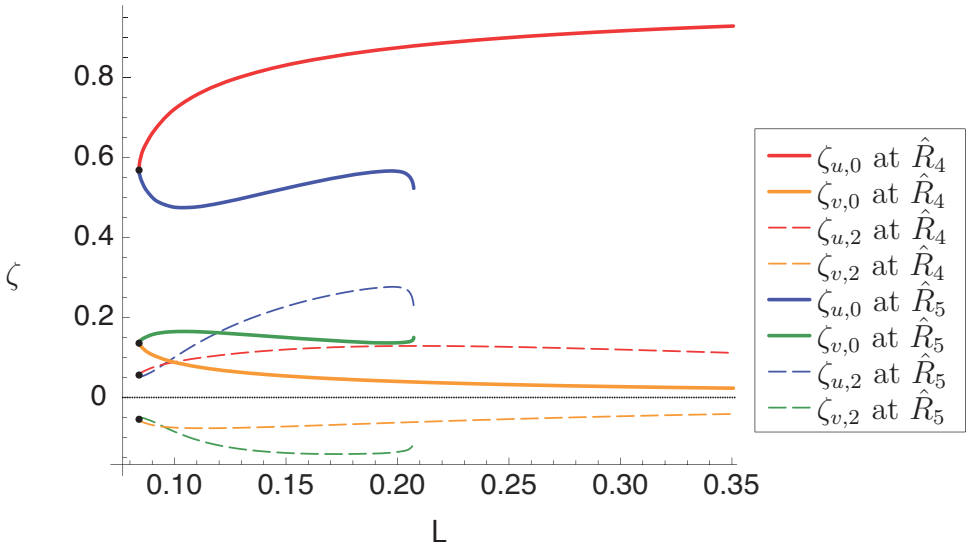

Figure 5.10. Amplitudes of equilibria at the fundamental saddle node bifurcation in $M = 30$ Galerkin projection of the Gray-Scott system.

We see that the saddle node bifurcation near $\mathsf{L} = 0.08674$ remains in this well resolved projection, and is qualitatively identical to the bifurcation in the $M = 1$ projection; however, the $\mathsf{L} = 0.3424$ saddle node bifurcation is no longer present since $\hat{R}_4$ has an analogous equilibrium at longer domain lengths. Instead, there is another bifurcation near $\mathsf{L} = 0.2075$, past which $\hat{R}_5$ does not converge to an analogous equilibrium using a Newton-Raphson root finder with our initial guess.

In this higher truncation, we also model shorter wavelengths, and, following the analysis in Appendix D, we predict higher modes of the $\hat{R}_4$ and $\hat{R}_5$ equilibria, which also display a saddle node bifurcation at integer multiples of $\mathsf{L} = 0.08674$. A Newton-Raphson root finder identifies these subsequent $\hat{R}_{4,m}$ and $\hat{R}_{5,m}$ equilibria, whose amplitudes are shown in Figure 5.11.

Since the $\hat{R}_{4,m}$ and $\hat{R}_{5,m}$ equilibria are analogous to the fundamental $\hat{R}_{4,1}$ and $\hat{R}_{5,1}$ equilibria, we only analyze the stability of $\hat{R}_4$ and $\hat{R}_5$, dropping the second

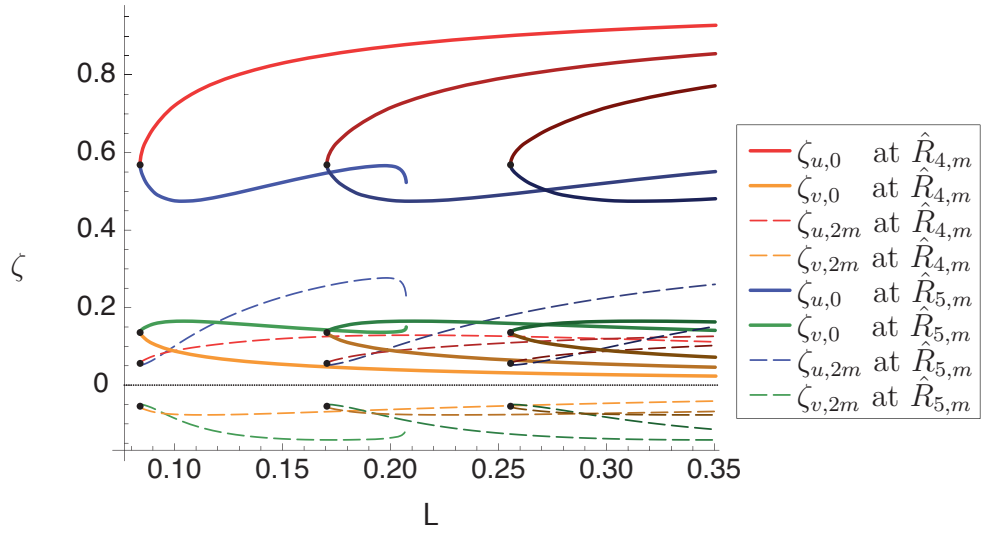

Figure 5.11. Amplitudes of equilibria at additional saddle node bifurcations in $M = 30$ Galerkin projection of the Gray-Scott system.

subscript for simplicity. In the $M = 30$ Galerkin projection, each equilibrium has one zero eigenvalue, which is a result of the one-dimensional manifold of phase shifted equilibria. Similar to the $M = 1$ truncation, we find that $\hat{R}_4$ has a positive eigenvalue for all domain lengths, so it is not a stable equilibrium. Again, we find that $\hat{R}_5$ has all negative eigenvalues for a region of domain lengths from $0.133 < \mathsf{L} < 0.205$, which is shown in Figure 5.12.

The lower stability limit at $\mathsf{L} = 0.133$ corresponds to a Hopf bifurcation, as the real part of a complex conjugate pair of eigenvalues has a sign change. This value also corresponds to the wave number, $\kappa = 7.5$, that was found from the Fourier analysis of the finite difference solution in Section 5.1.2. The upper stability limit occurs at approximately the length where we are unable to converge $\hat{R}_5$ to a fundamental equilibrium solution using the Newton-Raphson technique. These eigenvalues are no longer a complex conjugate pair, and one eigenvalue becomes

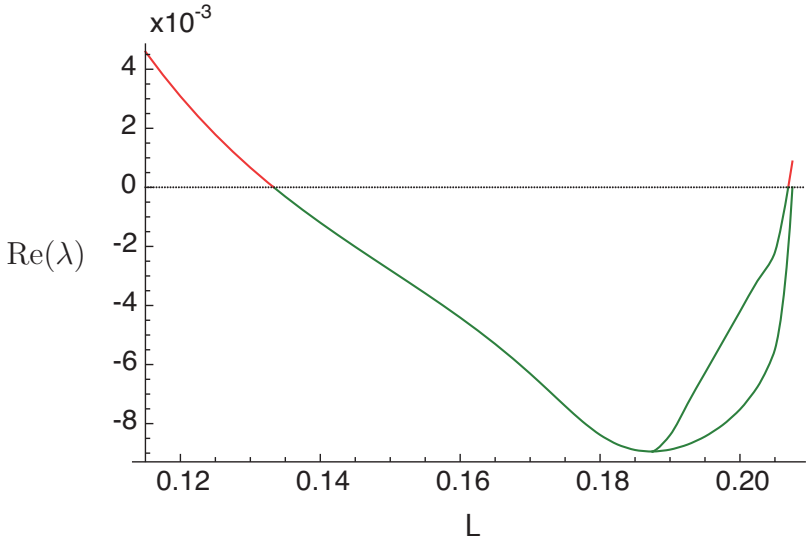

Figure 5.12. Hopf bifurcation of $\hat{R}_5$ in the Gray-Scott $M = 30$ Galerkin projection.

positive at a slightly shorter length scale than the other. We predict that the higher frequency mode equilibria, $\hat{R}_{5,m}$, will become stable at integer multiples of the Hopf bifurcation, $\mathsf{L} = m \times 0.133$. The two-dimensional solution from Section 5.1.2 on an $\mathsf{L} = 2.5$ square domain displays one of these higher frequency mode equilibria, approximately $\hat{R}_{5,18.8}$, where the $m = 18.8$ mode is not required to be an integer due to the combination of integer valued spatial modes in each dimension.

Now that we have found a stable equilibrium that represents the fundamental wave structure of the patterns, we examine the eigenvalues of the Jacobian from the spatially homogeneous system to evaluate the importance of the reaction and diffusion time scales coupling for this stable solution. Since the equilibrium at $\hat{R}_5$ has a spatial structure, the reaction eigenvalues are functions of position, whose real parts are shown in blue on the left of Figure 5.13. The red lines are the diffusion eigenvalues across the domain length of the fundamental wave structure,

$\mathsf{L} = 0.133$, and the dotted black line indicates $\mathrm{Re}(\lambda) = 0$. On the right of Figure 5.13, the reaction and diffusion time scales are shown in blue and red, respectively. From this figure we see that reaction and diffusion have similar time scales across the fundamental wavelength of the pattern. We analyze these time scales to test for consistency with the order of magnitude of the length scales in the problem. The diffusion coefficient, $\mathcal{D} = \mathcal{O}(1 \times 10^{-5})$, and the reaction time scales, $\tau_{\hat{R}5} = \mathcal{O}(100)$, give us the right order of magnitude for our length scale, $\mathsf{L} \sim 2\pi\sqrt{\mathcal{D}\tau} = \mathcal{O}(0.2)$. While this simple time scale analysis yields the right order of magnitude, it is not sufficient to identify the fundamental wavelength of the pattern or the shape of each fundamental wave.

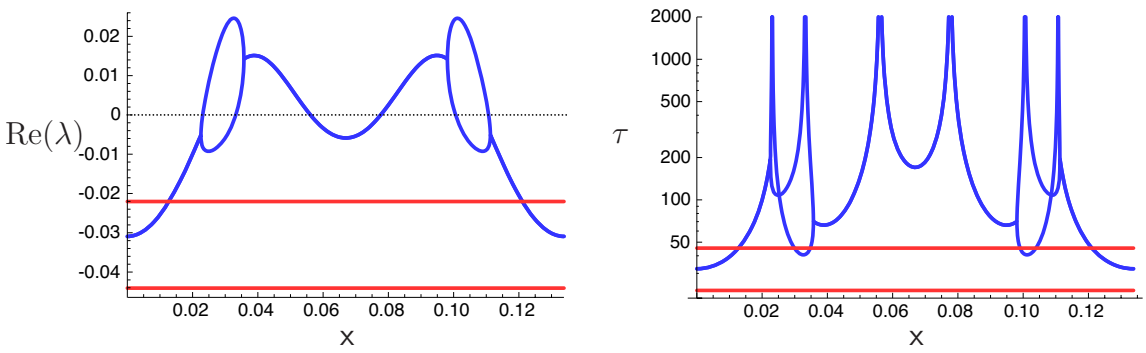

Figure 5.13. Eigenvalues and time scales of $\hat{R}_5$ in the Gray-Scott $M = 30$ Galerkin projection.

Using the fundamental stable solution from the $M = 30$ Galerkin projection, we can construct stable two-dimensional solutions to Eqs. (5.6) on an $\mathsf{L} = 2.5$ periodic domain. We identify the product of basis functions $\phi_{10}(\mathsf{x})\phi_{36}(\mathsf{y})$ as having

the isotropic wave number of $\kappa = \sqrt{5^2 + 18^2}/2.5 = 7.4726$, which is close to the predicted stable solution of $\kappa = 7.5$ from the finite difference results in Section 5.1.2. We use this as our fundamental basis function to construct a stable solution. We find the amplitudes of $\hat{R}_5$ in the one-dimensional solution for the corresponding fundamental length of $\mathsf{L} = 0.133822$. We then construct the initial conditions,

$$Y_i^* = \sum_{i=0}^{M=30} \zeta_i \phi_i \left(\frac{5\mathsf{x} + 18\mathsf{y}}{2.5} \right), \text{ for } i = U, V, \tag{5.19}$$

which we perturb by a uniformly distributed random amount between -0.01 and 0.01 at each grid point to evaluate the stability of our initial conditions. We solve for the time evolution using the same finite difference integration as was described in Section 5.1.2. The results are shown in Figure 5.14, with the initial conditions shown in the top row and a long time solution at $\mathsf{t} = 1 \times 10^4$ shown in the bottom row. A spatial contour plot of mass fraction, Y_V, is in the left column, a contour plot of amplitudes as a function of spatial wave number is shown in the center column, and the amplitudes of the isotropic wave numbers are shown in the right column. The initial and final mass fraction contour plots are nearly identical as we see that the initial conditions found from the one dimensional Galerkin projection are an accurate predication of a stable equilibrium in the two dimensional finite difference method. The wave number plots in Figure 5.14 are more descriptive of the differences between the initial conditions and long time solution. In the initial conditions the random perturbations induce amplitudes of $\mathcal{O}(10^{-5})$ across the spectrum of wave numbers, where peaks in the amplitude are noticeable for the fundamental mode and its next four higher harmonics in both wave number plots. In the long time limit, the perturbations have decayed, and the spatial structure is represented as a series of peaks in the amplitudes isolated

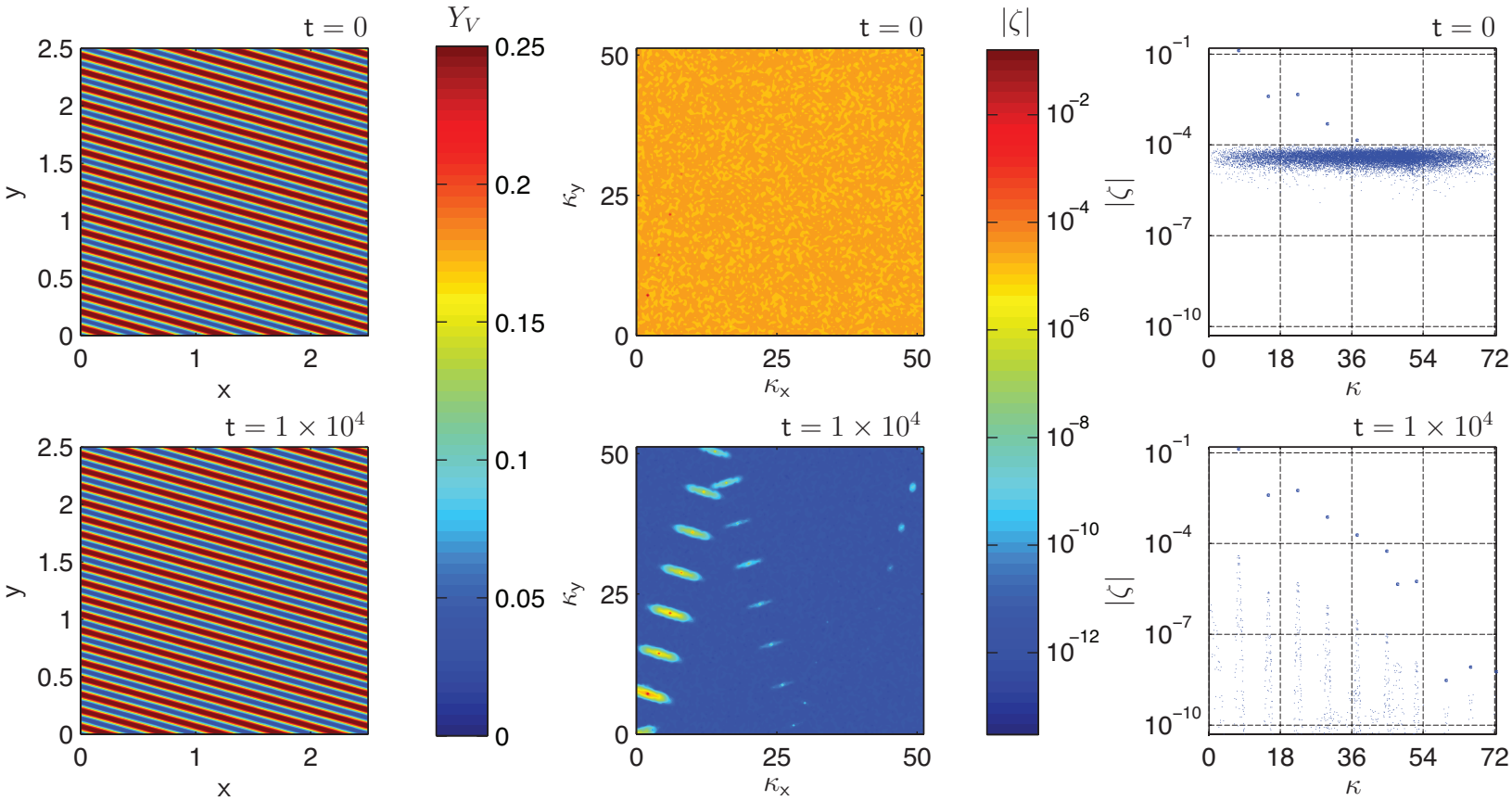

Figure 5.14: Anisotropic mass fraction pattern and amplitudes of the finite difference Gray-Scott system.

at specific wave numbers. In the spatial wave number contour plot, the peaks have a clear radial direction, which indicate the anisotropy in this long time limit. What appears as reflections in the wave number contour plot is a result of the aliasing of higher harmonic frequencies on a discrete grid.

We also construct a solution that is more isotropic, using a concentric circular pattern with waves spaced at $\mathsf{L} = 0.133822$, whose initial conditions are given as,

$$Y_i^* = \sum_{i=0}^{M=30} \zeta_i \phi_i \left(\frac{\sqrt{18^2 + 5^2}}{2.5} \sqrt{(\mathsf{x} - 1.25)^2 + (\mathsf{y} - 1.25)^2} \right), \text{ for } i = U, V. \quad (5.20)$$

We note that while this solution is periodic, there are steep gradients where the concentric circles intersect at the boundaries of the periodic domain, which do not have spatial structures similar to $\hat{R}_{5,m}$. These initial conditions are also perturbed by a uniformly distributed random amount between -0.01 and 0.01 at each grid point to identify their stability. The results are shown in Figure 5.15; again, the initial conditions are shown on the top row, and the long time solution is shown in the bottom row, at $\mathsf{t} = 1 \times 10^4$. In the mass fraction plot on the left, there is a larger difference between the initial condition and the long time limit than was seen in Figure 5.14. The mass fractions with initial steep gradients at the boundaries have reorganized into a spatial structure with patterns that are similar to the $\hat{R}_5$ solution. Also, the innermost circular pattern in the initial conditions has evolved into three spots, bringing into question the stability of stripes with higher curvature. The remaining circular patterns have become more faceted, appearing more octagonal than circular in the long time solution; this could be the result of the interactions at the boundaries on a periodic square grid, or might be a result of preference to the x and y dimensions of the imposed grid and finite difference operators. The wave number plots in Figure 5.15 again give a good description

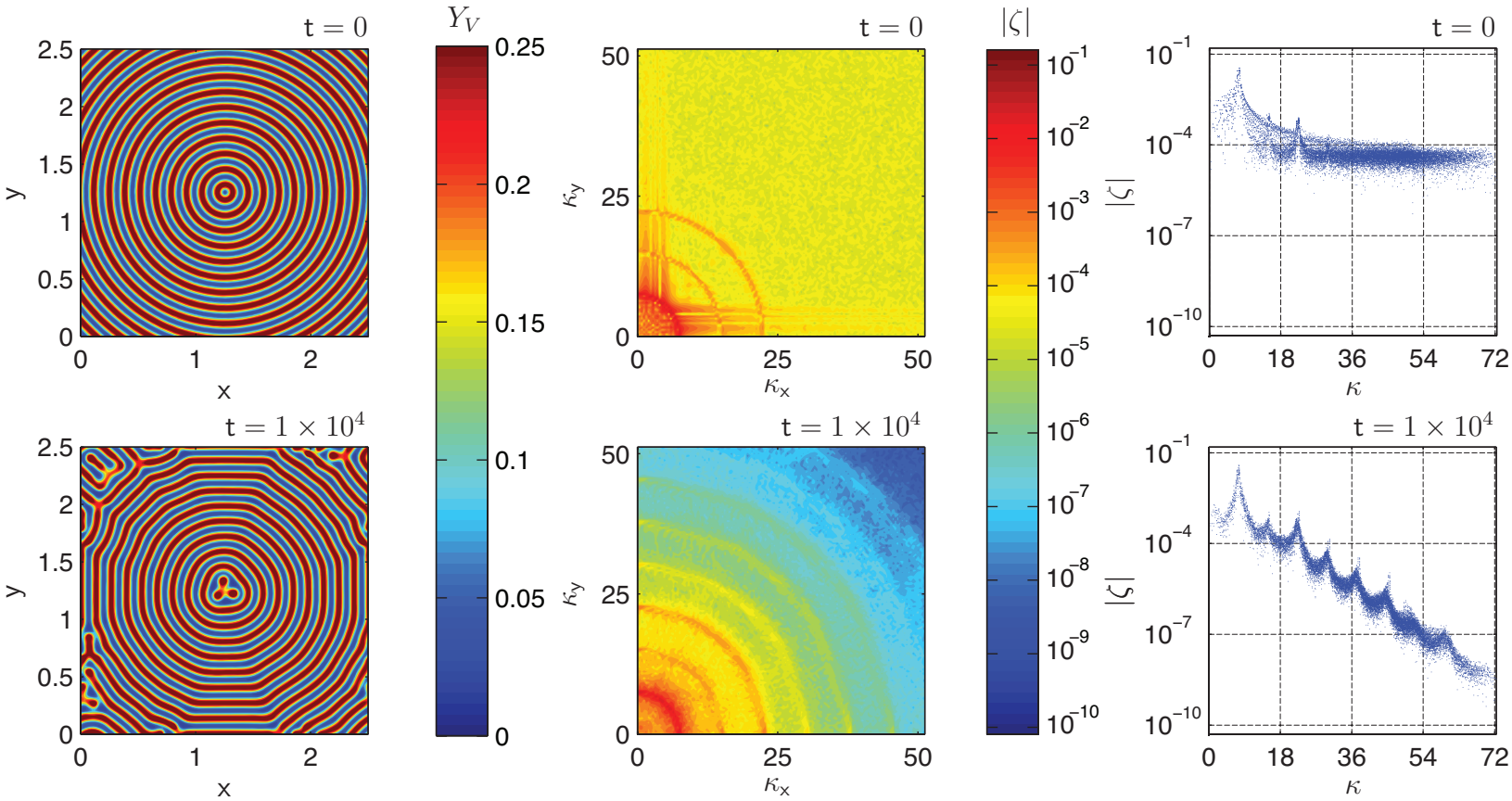

Figure 5.15: Circular mass fraction pattern and amplitudes of the finite difference Gray-Scott system.

of the differences between the initial conditions and long time limit. In the initial conditions the random perturbations again induce amplitudes of $\mathcal{O}(10^{-5})$ across the spectrum of wave numbers. The isotropic fundamental wave number and next two higher harmonics are shown as peaks in the amplitudes in both the spatial wave number contour plot and isotropic wave number plot. The imposed spatial structure of concentric circles has generated peaks in the amplitudes of low spatial wave numbers for each dimension, which are shown as red horizontal and vertical stripes in the spatial wave number contour plot. In wave number space, the long time limit for this initial condition appears similar to the long time limit for the initial condition of the problem in Section 5.1.2, which is shown at the bottom of Figure 5.6. In both of these figures, the peaks in the amplitudes appear at integer multiples of the fundamental wave number, $\kappa = 7.5$, with very few radial variations in the spatial contour plot, indicating an isotropic solution. For this solution, the amplitudes of spatial basis functions appear invariant under a rotation to other Cartesian coordinate systems, thus meeting our qualification for isotropy; however, anisotropy would likely be revealed in a transformation to a polar coordinate system.

As a third example, we construct a solution that is more isotropic than the first example, but that still shows a preference to one spatial direction. This is accomplished by solving for the long time limit of the initial conditions

$$Y_i^* = \sum_{i=0}^{M=30} \zeta_i \phi_i \left(\frac{18\mathsf{x} - 5\mathsf{y}}{2.5} + \sin\left(\frac{2\pi \mathsf{y}}{2.5} \right) \right), \text{ for } i = U, V, \tag{5.21}$$

which are periodic lines that have a small amplitude sinusoidal wave added. The results for this system are shown in Figure 5.16. These initial conditions again have random perturbations which induce $\mathcal{O}(10^{-5})$ amplitudes across the spectrum of

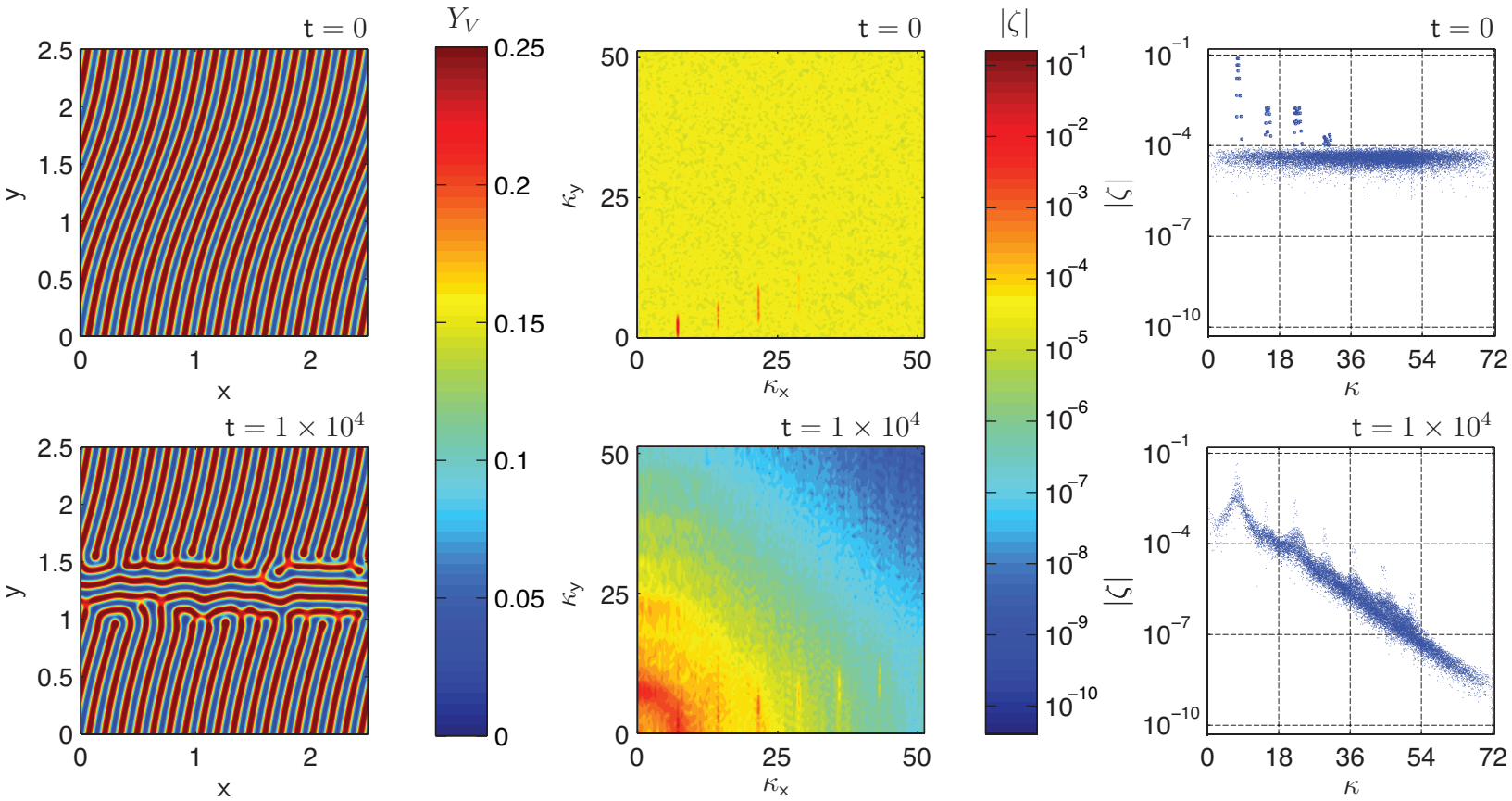

Figure 5.16: Sinusoidal mass fraction pattern and amplitudes of the finite difference Gray-Scott system.

wave numbers. There are also peaks along a specific axial direction in the spatial wave number contour plot. These peaks are broader than the peaks in Figure 5.14 since there are additional preferred directions in the initial conditions due to the sinusoidal wave in the stripes. The long time solution of mass fraction did not retain the periodic wave structure of the initial conditions. Where the wave had the greatest slope, $\mathsf{x} \in [1, 1.5]$, the curvature and reduced length between fundamental waves caused an instability; the structure from the initial conditions decayed, and a new spatial structure, which is primarily oriented in the x-direction, replaced it. For the long time limit, the amplitudes in the spatial wave number plot still show the broad peaks from the initial anisotropy, but they also show some additional peaks with low κ_{x} and high κ_{y} that come from the new horizontal structure.

From this analysis, we see that reaction time scales provide an accurate prediction for the order of magnitude of a fundamental length scale by using the diffusion coupling found from the Galerkin analysis, $\ell = 2\pi\sqrt{\mathcal{D}\tau}$. We also see that the $M = 1$ Galerkin projection provides a good estimate for the system's spatial structure near the fundamental length scale. However, the $M = 1$ truncation does not accurately predict the stability region of the solutions and is qualitatively incorrect for longer domain lengths. These shortcomings indicate the need for a spatially resolved approximation. We demonstrated that the spatially resolved $M = 30$ truncation accurately predicted the stable fundamental pattern of the Gray-Scott system.

5.2 Hydrogen-air mechanism

We evaluate the $N = 9$ species, $J = 20$ reaction, $L = 3$ element hydrogen-air mechanism of Miller and Bowman [108], which is shown in Table 5.2. In this table we use the forward stoichiometric constant of a third body molecule, $\nu'_{M,j}$ (which is one for reactions with a third body, and zero otherwise), to obtain the correct units for a_j. We choose to order the species $\{O_2,\ H_2,\ H_2O,\ N_2,\ OH,\ H,\ O,\ HO_2,\ H_2O_2\}$

as $i = 1, \ldots, 9$, yielding the species-reaction matrix as

$$\nu_{ij} = \begin{bmatrix} -1 & -1 & 0 & 0 & 2 & 0 & 0 & 0 & 0 \\ 0 & -1 & 1 & 0 & -1 & 1 & 0 & 0 & 0 \\ 1 & 0 & 0 & 0 & -1 & 1 & -1 & 0 & 0 \\ 0 & -1 & 0 & 0 & 1 & 1 & -1 & 0 & 0 \\ -1 & 0 & 0 & 0 & 0 & -1 & 0 & 1 & 0 \\ 1 & 0 & 1 & 0 & -1 & 0 & 0 & -1 & 0 \\ 0 & 0 & 0 & 0 & 2 & -1 & 0 & -1 & 0 \\ 1 & 0 & 0 & 0 & 1 & 0 & -1 & -1 & 0 \\ 0 & 0 & 1 & 0 & -2 & 0 & 1 & 0 & 0 \\ 0 & 1 & 0 & 0 & 0 & -2 & 0 & 0 & 0 \\ 0 & 1 & 0 & 0 & 0 & -2 & 0 & 0 & 0 \\ 0 & 1 & 0 & 0 & 0 & -2 & 0 & 0 & 0 \\ 0 & 0 & 1 & 0 & -1 & -1 & 0 & 0 & 0 \\ 0 & 0 & 0 & 0 & 1 & -1 & -1 & 0 & 0 \\ 1 & 0 & 0 & 0 & 0 & 0 & -2 & 0 & 0 \\ 1 & 1 & 0 & 0 & 0 & -1 & 0 & -1 & 0 \\ 1 & 0 & 0 & 0 & 0 & 0 & 0 & -2 & 1 \\ 0 & 0 & 0 & 0 & 2 & 0 & 0 & 0 & -1 \\ 0 & 1 & 0 & 0 & 0 & -1 & 0 & 1 & -1 \\ 0 & 0 & 1 & 0 & -1 & 0 & 0 & 1 & -1 \end{bmatrix}', \tag{5.22}$$

and the species-element matrix as

$$\varphi_{li} = \begin{bmatrix} 0 & 2 & 2 & 0 & 1 & 1 & 0 & 1 & 2 \\ 2 & 0 & 1 & 0 & 1 & 0 & 1 & 2 & 2 \\ 0 & 0 & 0 & 2 & 0 & 0 & 0 & 0 & 0 \end{bmatrix}. \tag{5.23}$$

We examine conditions a similar to a lean isothermal isobaric system that Kalamatianos and Vlachos [107] show to have a limit cycle. While we also evaluate this mechanism as isothermal, $T = 993\ K$, we consider it isochoric, $\rho = 9.25 \times 10^{-4}\ g/cm^3$, to simplify our method of isolating equilibria using `BERTINI` [109]. To exhibit a similar limit cycle in the modified system, we consider a feed flow rate with a corresponding to a residence time of $\tau_{\mathcal{R}} = V\rho/\dot{m} = 1.1 \times 10^{-3}\ s$; this feed flow rate is decreased slightly from the one considered in Kalamatianos and Vlachos [107] with a residence time of $\tau_{\mathcal{R}} = 1 \times 10^{-3}\ s$. The inflow is a hydrogen-air mixture with an equivalence ratio of $\Phi = 0.5$: for every 1 mol of O_2, there will be $2\Phi = 1\ mol$ of H_2 and 3.67 mol of N_2. For these parameters the inflow in specific moles is $z_1 = 7.3087 \times 10^{-3}\ mol/g$, $z_2 = 7.3087 \times 10^{-3}\ mol/g$, and $z_4 = 2.6823 \times 10^{-2}\ mol/g$, which has a pressure of $P = 3.1648 \times 10^6\ dyne/cm^2$; the complete combustion has a pressure of $P = 2.6066 \times 10^6\ dyne/cm^2$. Again, we use the `CHEMKIN` thermodynamic database [104] to find the species' thermodynamic data and the `CHEMKIN TRANSPORT` database [103] to approximate a diffusion coefficient of $\mathcal{D} = 21.2\ cm^2/s$.

By demanding that the initial conditions' concentrations have the same elemental composition as the inflow, this system has $\hat{L} = 3$ algebraic constraints: conservation of each element, H, O, and N; therefore, the system has $R = N - \hat{L} = 6$ dimensions. We model species $i = \{1, 2, 3, 5, 6, 7\}$ and use the algebraic constraints

TABLE 5.2

HYDROGEN-AIR REACTION MECHANISM

j	Reaction	a_j $[\frac{(\frac{mol}{cm^3})^{(1-\nu'_{M,j}-\sum_{i=1}^{N}\nu'_{i,j})}}{s\ K^{\beta_j}}]$	β_j	$\bar{E}_j$ $[\frac{erg}{mol}]$
1	$H_2 + O_2 \leftrightharpoons 2OH$	0.170×10^{14}	0.000	47780
2	$H_2 + OH \leftrightharpoons H_2O + H$	0.117×10^{10}	1.300	3626
3	$OH + O \leftrightharpoons O_2 + H$	0.400×10^{15}	−0.500	0
4	$H_2 + O \leftrightharpoons OH + H$	0.506×10^{5}	2.670	6290
5	$O_2 + H + M \leftrightharpoons HO_2 + M^a$	0.361×10^{18}	−0.720	0
6	$OH + HO_2 \leftrightharpoons O_2 + H_2O$	0.750×10^{13}	0.000	0
7	$H + HO_2 \leftrightharpoons 2OH$	0.140×10^{15}	0.000	1073
8	$O + HO_2 \leftrightharpoons O_2 + OH$	0.140×10^{14}	0.000	1073
9	$2OH \leftrightharpoons H_2O + O$	0.600×10^{9}	1.300	0
10	$2H + M \leftrightharpoons H_2 + M^b$	0.100×10^{19}	−1.000	0
11	$2H + H_2 \leftrightharpoons 2H_2$	0.920×10^{17}	−0.600	0
12	$2H + H_2O \leftrightharpoons H_2 + H_2O$	0.600×10^{20}	−1.250	0
13	$OH + H + M \leftrightharpoons H_2O + M^c$	0.160×10^{23}	−2.000	0
14	$H + O + M \leftrightharpoons OH + M^c$	0.620×10^{17}	−0.600	0
15	$2O + M \leftrightharpoons O_2 + M$	0.189×10^{14}	0.000	−1788
16	$H + HO_2 \leftrightharpoons H_2 + O_2$	0.125×10^{14}	0.000	0
17	$2HO_2 \leftrightharpoons O_2 + H_2O_2$	0.200×10^{13}	0.000	0
18	$H_2O_2 + M \leftrightharpoons 2OH + M$	0.130×10^{18}	0.000	45500
19	$H + H_2O_2 \leftrightharpoons H_2 + HO_2$	0.160×10^{13}	0.000	3800
20	$OH + H_2O_2 \leftrightharpoons H_2O + HO_2$	0.100×10^{14}	0.000	1800

All third body molecule collision coefficients are one except where noted.

[a]Reaction 5: $M_{H_2} = 2.86$, $M_{H_2O} = 18.6$, $M_{N_2} = 1.26$

[b]Reaction 10: $M_{H_2} = 0.0$, $M_{H_2O} = 0.0$

[c]Reaction 13 and 14: $M_{H_2O} = 5.0$

to solve for the concentrations of species $i = \{4, 8, 9\}$. Following the reduction technique showed in Section 3.1.3, we identify the algebraic constraints as

$$\begin{aligned}
\hat{z}_4 &= \hat{z}_4^* && (5.24a)\\
\hat{z}_8 &= \hat{z}_8^* - 2(z_1 - z_1^*) + 2(z_2 - z_2^*) + (z_3 - z_3^*) \\
&\qquad +(z_6 - z_6^*) - (z_7 - z_7^*), && (5.24b)\\
\hat{z}_9 &= \hat{z}_9^* + (z_1 - z_1^*) - 2(z_2 - z_2^*) - \frac{3}{2}(z_3 - z_3^*) \\
&\qquad -\frac{1}{2}(z_5 - z_5^*) - (z_6 - z_6^*) + \frac{1}{2}(z_7 - z_7^*). && (5.24c)
\end{aligned}$$

These algebraic constraints require that the concentration of $z_4 = 2.6823 \times 10^{-2}\ mol/g$ remain constant and

$$\begin{aligned}
z_8 &= -2z_1 + 2z_2 + z_3 + z_6 - z_7, && (5.25a)\\
z_9 &= z_1 - 2z_2 - \frac{3}{2}z_3 - \frac{1}{2}z_5 - z_6 + \frac{1}{2}z_7 + 7.3086 \times 10^{-3}\ mol/g. && (5.25b)
\end{aligned}$$

We model the hydrogen-air reaction-diffusion system in the $M = 0$ spatially homogeneous limit and seek to construct the branches of the spatially homogeneous SIM. Using `BERTINI`, with the input file described in Appendix G, we identify 97 real finite equilibria of this system. Of these equilibria, three have positive concentrations for all nine species, making them physical, and 13 have one positive eigenvalue, making them candidates for the SIM-BIC; the physical equilibria and SIM-BIC candidates are listed in Table 5.3.

We evaluate the character of the physical equilibria: R_4 has all negative real eigenvalues and is a physical sink; R_{69} has one positive real eigenvalue, making it both a physical equilibrium and a SIM-BIC candidate; and R_1 has four negative real eigenvalues and one complex conjugate pair of eigenvalues with positive real

TABLE 5.3:

HYDROGEN-AIR CSTR EQUILIBRIA

R_n	z_1 $[mol/g]$	z_2 $[mol/g]$	z_3 $[mol/g]$	z_5 $[mol/g]$	z_6 $[mol/g]$	z_7 $[mol/g]$
			Physical equilibria			
1	0.0067874	0.0063370	0.00090796	9.4755×10^{-8}	4.4741×10^{-7}	1.0672×10^{-7}
4	0.0073082	0.0073081	4.2541×10^{-7}	3.9643×10^{-11}	4.0545×10^{-10}	9.5066×10^{-11}
69	0.0072984	0.0072930	0.000012184	1.1357×10^{-9}	1.0111×10^{-8}	2.3570×10^{-9}
			SIM-BIC candidates			
3	−206.82	9.5363×10^{-7}	−414.26	0.00068782	-7.6532×10^{-10}	−0.32575
9	−0.0017378	0.0021354	0.0052458	0.00025751	−0.0010971	0.012353
15	27.605	−375.19	97.278	−13.033	20.643	−137.20
17	0.81348	−0.63533	0.078878	0.0028641	1.1263	−1.6909
30	0.00040481	−0.057763	−0.013044	−0.000073990	0.15631	0.026929
43	0.025791	0.040608	−0.0078804	0.0013074	−0.022876	−0.0011160
53	0.0073054	0.0073024	4.56975×10^{-6}	4.2629×10^{-10}	4.7038×10^{-9}	1.1126×10^{-9}
56	−0.021759	−0.037950	0.033021	0.000031592	-1.1130×10^{-6}	−0.00022778
69	0.0072984	0.0072930	0.000012184	1.1357×10^{-9}	1.0111×10^{-8}	2.3570×10^{-9}
78	0.0036823	0.000017510	0.0077738	−0.00012919	-2.148×10^{-6}	0.000048179
86	−0.0013668	7.0010×10^{-6}	−0.00031425	-2.2173×10^{-7}	-2.1200×10^{-6}	0.0024318
91	0.0033886	−0.34619	0.54825	−0.0027026	0.046812	−0.10504
97	105.31	67.005	−8.0934	0.0028924	−7.5207	−85.546

part, making it a saddle. The long time dynamics of systems with initial conditions in the neighborhood of R_1 exhibit limit cycle behavior. The eigenvalues of the physical equilibria are given in Table 5.4

We integrate the system with initial conditions perturbed along R_{69}'s unstable eigenvector in either direction. In one direction, the trajectory approaches R_4 along its slowest eigenvector; this heteroclinic orbit is a branch of the SIM. In the other direction, the trajectory collapses onto the stable limit cycle. These trajectories are shown in a projection of phase space in Figure 5.17, where the branch of the SIM is in red and the trajectory that collapses onto the stable limit cycle is in blue.

The time evolution of these trajectories is shown in Figure 5.18, where on the left is the evolution along the branch of the SIM, and on the right is the stable limit cycle. In these plots, the evolution of O_2 is shown in a blue solid line, H_2, red solid, H_2O, green solid, N_2, black solid, OH, green dashed, H, red dashed, O, blue dashed, HO_2, magenta dashed, and H_2O_2, cyan dashed. The concentrations of O_2 and H_2 nearly overlap in both plots, as the concentration of O_2 for both of these solutions remains only marginally higher than the concentration of H_2.

From this analysis we deduce that R_{69} lies on the boundary of the basin of attraction between the stable limit cycle and the steady state equilibrium, R_4. Integrating trajectories in reverse time with initial conditions that span the five stable eigenvectors of the equilibrium R_{69}, will construct a five-dimensional manifold which will define this boundary between the basins of attraction; however, the computational costs associated with this method and the logistics of sorting, storage, and retrieval of the data render it impractical.

We now seek other branches of the SIM, examining the heteroclinic orbits from

TABLE 5.4:

EIGENVALUES OF SELECTED HYDROGEN-AIR CSTR EQUILIBRIA

R_n	λ_1 $[s^{-1}]$	λ_2 $[s^{-1}]$	λ_3 $[s^{-1}]$	λ_4 $[s^{-1}]$	λ_5 $[s^{-1}]$	λ_6 $[s^{-1}]$
			Physical equilibria			
1	(2056.51	$\pm$ 5313.49i)	-1874.69	-166528	-1.81496×10^6	-1.01916×10^7
4	-250.238	-908.984	-3427.75	-196629	-2.16140×10^6	-1.00969×10^7
69	153.805	-906.041	-11365.6	-157177	-2.12071×10^6	-1.02875×10^7
			SIM-BIC equilibria			
9	2.77204×10^7	-263460	(-683877	$\pm$ 154582i)	-4.15025×10^7	-9.51795×10^7
17	1.97984×10^{10}	-8.80067×10^7	(-9.39869×10^7	$\pm$ 2.29324×10^9i)	-2.50445×10^8	-8.54337×10^{10}
30	8.95079×10^6	(-2.39043×10^7	$\pm$ 1.24066×10^7i)	-3.32513×10^7	-3.90786×10^8	-1.37204×10^{10}
53	8196.73	-201.422	-908.072	-254141	-2.21784×10^6	-9.82894×10^6

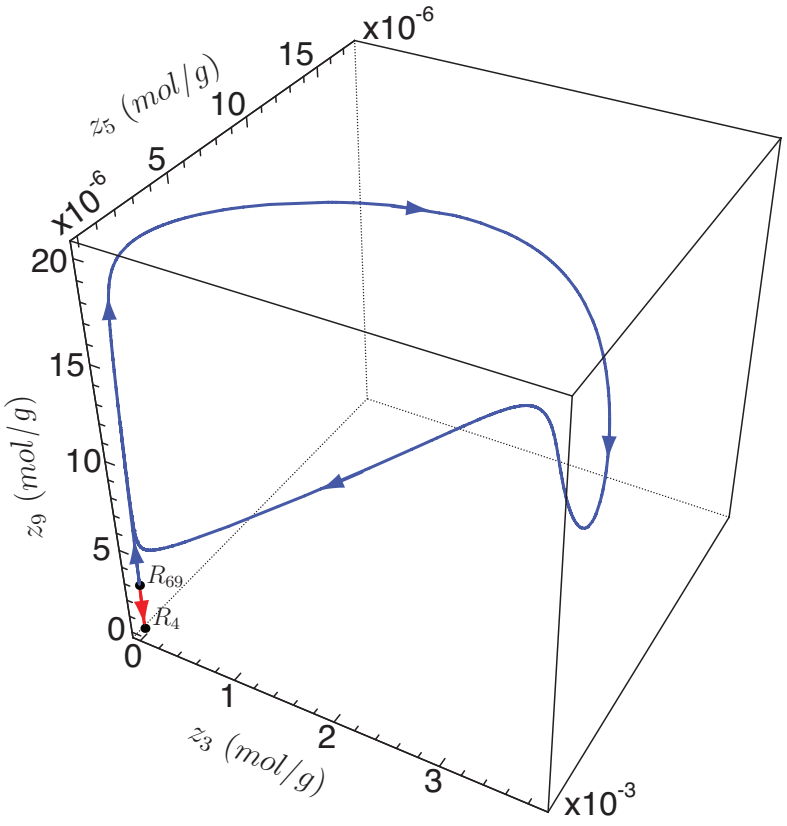

Figure 5.17. The limit cycle and a branch of the SIM in the hydrogen-air mechanism.

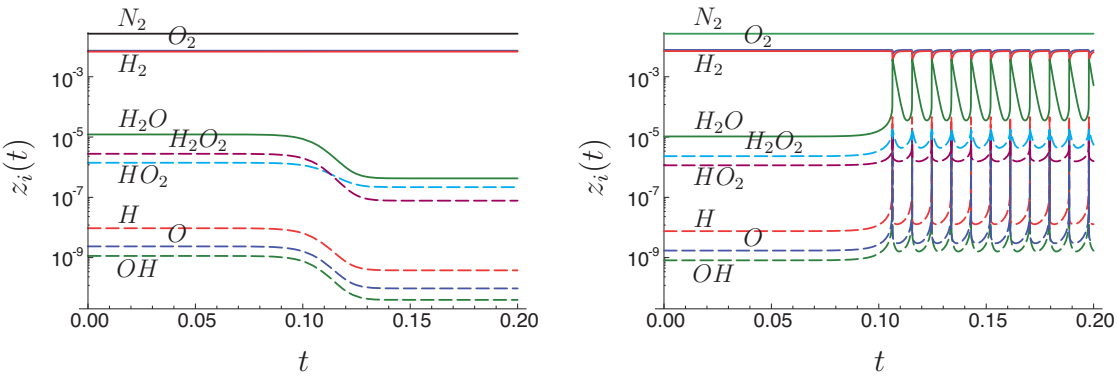

Figure 5.18. Evolution of hydrogen-air mechanism along either direction of the R_{69} unstable eigenvector.

the other SIM-BIC candidate equilibria. We find four additional branches of the SIM, one from each equilibria: R_9, R_{17}, R_{30}, and R_{53}; their eigenvalues are given in Table 5.4. A phase space projection of these SIM branches' approach to the physical equilibrium sink, R_4, is shown in Figure 5.19. In this figure, the red and blue lines are the same trajectories shown in Figure 5.17 and the green lines are the additional branches of the SIM. Note that all of the SIM branches approach R_4 from the same direction. We have not necessarily found all of the SIM branches since we have not considered equilibria at infinity. The dashed lines that connect the SIM branches to their SIM-BICs outside of the region plotted in Figure 5.19 are only sketches and do not accurately represent the paths of the trajectories though phase space.

To evaluate the attractiveness of these branches of the SIM, we calculate the normal stretching ratio, $r(\mathbf{z}_{\mathscr{M}})$, along each manifold, as is described in Appendix F. The stretching ratios along the SIM branches from R_{69}, R_{53}, and R_9 are shown in Figure 5.20 as a function of normalized manifold distance, $s(\mathbf{z}_{\mathscr{M}})$. In these figures, green lines indicate negative normal stretching rates, which are attractive in the corresponding normal direction, while red lines indicate positive normal stretching ratios, which are repulsive in the corresponding normal direction. There are five normal stretching ratios which each correspond to one of the orthogonal unit vectors that span the normal space.

In Figures 5.20(a) and 5.20(b) we see that all five of the stretching ratios remain negative along the entire length of both the R_{69} and R_{53} SIM branches; however, in Figure 5.20(c) we see there are positive stretching ratios in multiple normal directions for a large portion of the SIM branch near the R_9 SIM-BIC. This indicates nearby trajectories in these normal directions will diverge from the

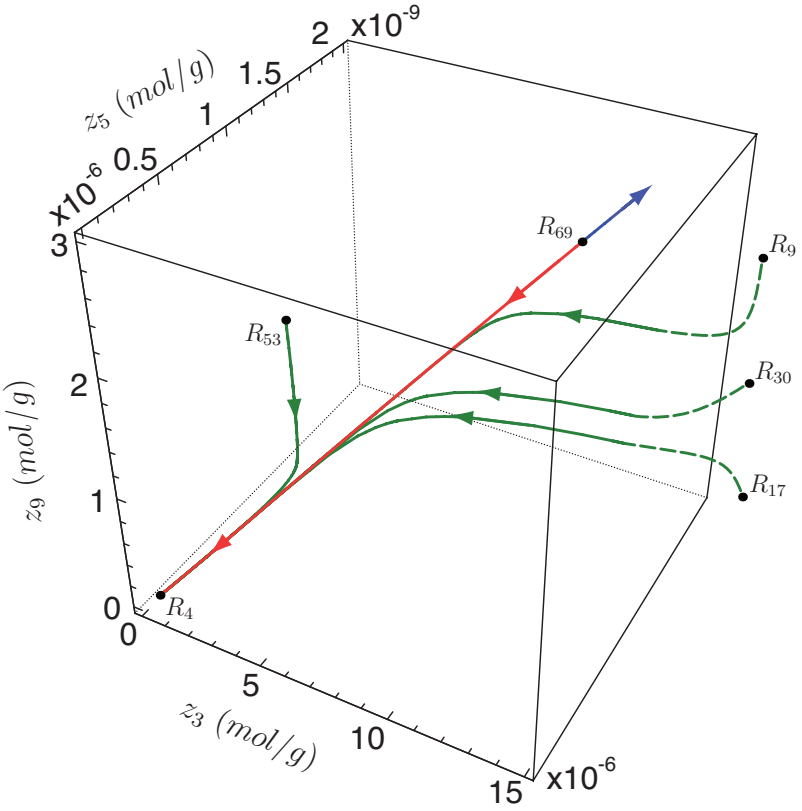

Figure 5.19. Multiple branches of the SIM in the hydrogen-air mechanism.

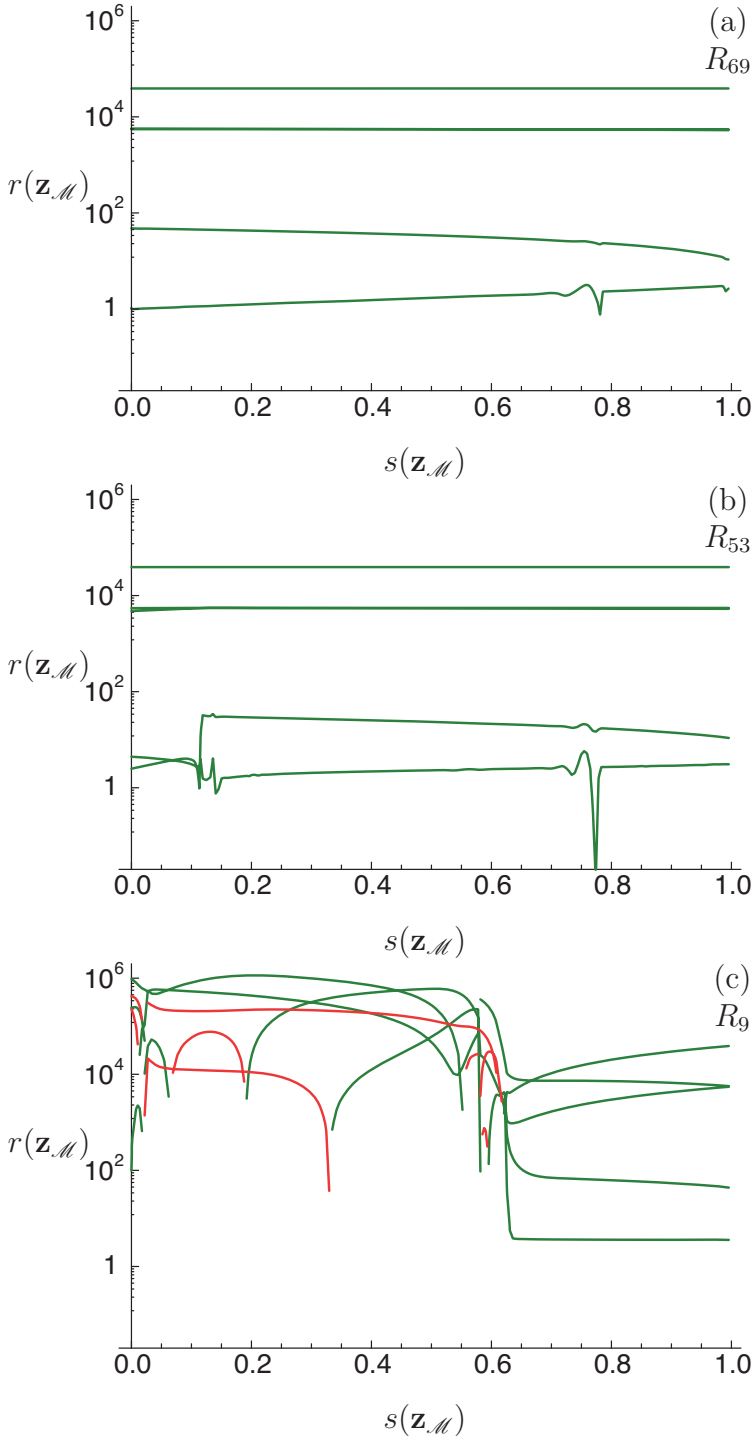

Figure 5.20. Stretching ratios of SIM branches in the hydrogen-air mechanism.

manifold, a trait that is not desirable in a manifold used in a reduction technique. Analysis along the R_{17} and R_{30} SIM branches yields similar results to the R_9 SIM branch, where both of those branches have positive normal stretching rates, which all become negative for the region of the manifold near R_4.

These results raise some concerns about heteroclinic orbit SIM construction technique. In addition to identifying multiple SIM branches that require subsequent analysis to implement an accurate reduction technique, the branches that this method identifies are not necessarily attractive, despite meeting the other qualifications to be a SIM. This brings into question the robustness of connecting heteroclinic orbits to construct SIMs.

5.3 Summary and conclusions

In this chapter, we have examined two different open systems: the Gray-Scott and hydrogen-air reaction mechanisms. For each system we constructed the spatially homogeneous SIM and found there to be multiple branches. This result is not unique to open reaction systems; a similar result was found for the closed adiabatic Zel'dovich mechanism shown in Section 4.1.3.2. Having multiple branches raises concerns about the implementation of the SIM as a reduction technique. While all the SIM branches we found were within the same basin of attraction, projecting onto various branches potentially leads to erroneous predictions if the projector is not carefully selected. Additionally, not all SIM branches identified by selecting heteroclinic orbits that meet our criteria were found to be attractive when evaluating their stretching ratios. Another issue which must be addressed is identifying basins of attraction for various long time dynamics. As was seen in the Gray-Scott example, if a projection crosses a boundary of a basin of attrac-

tion, there will be large errors in the resulting prediction. These concerns identify many issues that must be addressed before the SIM can be used as a robust and accurate reduction technique.

We also examined pattern formation in reaction-diffusion equations. From this analysis we found that a low dimensional approximation using the Galerkin projection qualitatively identified the structure of patterns predicted with better resolved simulations. We also found that the coupling of reaction and diffusion scales accurately predicted the order of magnitude of the pattern's length scales, while a higher resolution approximation was required to predict the actual length scale.

CHAPTER 6

DISCUSSION AND FUTURE WORK

This chapter contains additional discussion about the methods and results shown in the previous chapters, and also outlines future work required.

6.1 Discussion

The methods discussed in this dissertation have extended the SIM construction technique of connecting heteroclinic orbits to reaction-diffusion systems. This analysis identified a length scale at which the spatially homogeneous SIM accurately describes the slowest dynamics of the system. This length scale is typically on the order of micrometers for reactions at atmospheric pressure. When domains are considered that are longer than this length scale, diffusion will become the slowest process for long wavelengths, and the spatially homogeneous SIM will no longer capture the slowest dynamics of the system. Furthermore, the spectral gap between the first two eigenvalues shrinks in systems with domains longer than the critical length scale, indicating a need for a SIM of greater-than-one dimension.

When considering open reaction-diffusion systems, we found systems that displayed limit cycle behavior and pattern formation. In a Gray-Scott system that displayed limit cycle behavior, we demonstrated one of the pitfalls in using a manifold method: if a reduction technique projects the solution across the boundary of a basin of attraction, the predicted solution will incur large errors. We

have also identified systems which have multiple SIM branches that vary in their attractiveness. These multiple branches identify a concern about implementing the SIM as a reduction technique: the projection onto a specific SIM branch requires additional analysis. We also find that some of the SIM branches identified by connecting heteroclinic orbits have positive normal stretching rates, bringing into question the foundation of our manifold construction technique. Lastly, we use the Galerkin projection to analyze the pattern formation found in Gray-Scott systems.

6.2 Future work

We have identified some open questions for the applications of SIMs to both spatially homogeneous and reaction-diffusion systems. For example, how does one select which branch of the SIM will accurately describe the dynamics of a trajectory with specific initial conditions? A metric such as the normal stretching ratio could prove useful in this analysis. Are there additional criteria to be used in selecting heteroclinic orbits as branches of the SIM such that the selected orbits are attracting manifolds? Is there a different technique that is more robust to calculate the SIM branches?

An additional topic that is worthy of future pursuit is identifying a construction technique for higher-dimensional manifolds in Galerkin projections of reaction-diffusion equations. With an adequate technique of higher-dimensional manifold construction, a multiple dimensional SIM would be able to span the additional slow time scales on longer domain lengths up to the spectral gap. This construction technique may prove to be generalizable because of the physical coupling of reaction and diffusion scales. Further examinations of length scales where reac-

tion and diffusion have similar time scales might prove insightful to identifying an adequate correction to add to spatially homogeneous manifold methods when implemented in reaction-diffusion systems.

More generally, the field of combustion is still in need of adequate rational reduction techniques. The examples provided in this dissertation were extremely simple, yet identified a plethora of challenges in identifying a method that can substantially reduce computational costs while providing accurate predictions.

Realistic DNS simulations are still intractable for engineering scale geometries, and other reduction methods are still prone to error; however, our society is not going to stop turning to chemical reactions to meet our energy needs. Therefore, we must continue to seek improvements to methods we use to simulate combustion.

APPENDIX A

PERIODIC BOUNDARY CONDITIONS BASIS FUNCTION ANALYSIS

This appendix details the the Galerkin projection for domains with periodic boundary conditions. The eigenfunctions of the diffusion operator that match the periodic boundary conditions,

$$\mathcal{D}\frac{d^2\phi_m}{dx^2} = -\mu_m\phi_m(x), \text{ for } m = 0, \ldots, \infty \tag{A.1}$$

$$\phi_m(0) = \phi_m(\ell), \text{ and } \left.\frac{\partial\phi_m}{\partial x}\right|_{x=0} = \left.\frac{\partial\phi_m}{\partial x}\right|_{x=\ell}, \text{ for } m = 0, \ldots, \infty, \tag{A.2}$$

are both the sine and cosine functions whose arguments are integer multiples of $2\pi x/\ell$. We choose to order this basis as

$$\phi_m(x) = \begin{cases} 1 & \text{for } m = 0, \\ \sin\left((m+1)\pi\frac{x}{\ell}\right) & \text{for odd } m, \\ \cos\left(m\pi\frac{x}{\ell}\right) & \text{for even } m. \end{cases} \tag{A.3}$$

This is a complete orthogonal basis on the domain $x \in [0, \ell)$, and the $m = 0$ mode is spatially homogeneous. The eigenvalues of these basis functions are real and non-negative:

$$\mu_m = \frac{\mathcal{D}\pi^2\left(m + \bmod [m, 2]\right)^2}{\ell^2}. \tag{A.4}$$

We see that two eigenfunctions each have the same eigenvalue for all $m > 0$. This allows for functions with the same period to have an arbitrary phase shift, which was prohibited by homogeneous Neumann boundary conditions, but is admitted for periodic boundary conditions.

When truncated at a finite M, the Galerkin method projects the infinite-dimensional dynamics of the governing PDE onto a finite-dimensional AIM with dynamics governed by an ODE in the form of Eq. (3.15),

$$\frac{d\zeta_{i,m}}{dt} = \dot{\Omega}_{i,m}(\zeta_{j,n}) - \frac{\mathcal{D}\pi^2 \left(m + \text{ mod } [m, 2]\right)^2}{\ell^2}\zeta_{i,m}, \tag{A.5}$$

for $i, j = 1, \ldots, R$ and $m, n = 0, \ldots, M$.

Trigonometric identities and the orthogonality of these basis functions can again be used to analytically solve for the inner product of low-order polynomials to yield $\dot{\Omega}_{i,m}(\zeta_{j,n})$ without numerical integration; more detail is provided in Section B.2.

APPENDIX B

GALERKIN PROJECTION OF LOW-ORDER POLYNOMIALS

We seek an analytic reduction of the inner products in the Galerkin projection to allow for root finding techniques such as algebraic methods and homotopy continuation used by `BERTINI` [109]. The technique described in this appendix details the analytical reduction of low order polynomials (such as those in isothermal Arrhenius kinetics) into their Galerkin projection components.

B.1 Cosine basis functions: homogeneous Neumann boundary conditions

To reduce computational costs as well as simplify the analysis, the inner product of arbitrary low-order monomials are analytically simplified into their respective Galerkin projection amplitudes for cosine basis functions. This is relevant since our reaction source terms in isothermal Arrhenius kinetics are low-order polynomial systems, and the inner product distributes to each monomial as a linear operator. Here we examine up to third-order monomial expansions of arbitrary species labeled with subscripts a, b, and c.

In the following derivations, we take advantage of the fact that cosine is an even function,

$$\cos\left(\frac{m\pi x}{\ell}\right) = \cos\left(-\frac{m\pi x}{\ell}\right). \tag{B.1}$$

We apply the normalized inner product for our orthogonal basis functions with

arbitrarily signed arguments by using the Kronecker delta function for both the positive and negative of our function's argument.

Since the inner product is a linear operator and can be distributed to each term of a polynomial, we examine each order of monomial individually. For constants, we see that the normalized inner product results in the constant appearing only in the $m = 0$ term of the Galerkin projection, and in no other term. When $\phi_0 = 1$, as it does in our Galerkin projection, the constant remains unchanged,

$$\frac{\langle \phi_m, c \rangle}{\langle \phi_m, \phi_m \rangle} = c\delta_{m,0}. \tag{B.2}$$

Single variables are expanded into a summation of their amplitudes and basis functions,

$$z_a = \sum_{i=0}^{M} \zeta_{a,i} \cos\left(\frac{i\pi x}{\ell}\right); \tag{B.3}$$

we clarify that i is an integer counter, not the imaginary number. The normalized inner product can be distributed into this summation, and the orthogonality of basis functions yields each amplitude of that variable appearing in its respective term in the Galerkin expansion with unchanged coefficients,

$$\frac{\langle \phi_m, z_a \rangle}{\langle \phi_m, \phi_m \rangle} = \sum_{i=0}^{M} \frac{\zeta_{a,i}}{1 + \delta_{m,0}} \left(\delta_{m,i} + \delta_{m,-i}\right) = \zeta_{a,m}. \tag{B.4}$$

Higher order terms require a reduction using the trigonometric identity to reduce products of cosines into sums of cosines,

$$\cos\left(\frac{i\pi x}{\ell}\right)\cos\left(\frac{j\pi x}{\ell}\right) = \frac{1}{2}\left(\cos\left(\frac{(i+j)\pi x}{\ell}\right) + \cos\left(\frac{(i-j)\pi x}{\ell}\right)\right). \tag{B.5}$$

An arbitrary second order monomial expands into,

$$z_a z_b = \left(\sum_{i=0}^{M} \zeta_{a,i} \cos\left(\frac{i\pi x}{\ell}\right)\right)\left(\sum_{j=0}^{M} \zeta_{b,j} \cos\left(\frac{j\pi x}{\ell}\right)\right), \tag{B.6a}$$

$$= \sum_{i=0}^{M}\sum_{j=0}^{M} \zeta_{a,i}\zeta_{b,j} \cos\left(\frac{i\pi x}{\ell}\right)\cos\left(\frac{j\pi x}{\ell}\right), \tag{B.6b}$$

$$= \sum_{i=0}^{M}\sum_{j=0}^{M} \frac{\zeta_{a,i}\zeta_{b,j}}{2}\left(\cos\left(\frac{(i+j)\pi x}{\ell}\right) + \cos\left(\frac{(i-j)\pi x}{\ell}\right)\right). \tag{B.6c}$$

Here the normalized inner product again distributes to each term in the series, yielding

$$\frac{\langle \phi_m, z_a z_b\rangle}{\langle \phi_m, \phi_m\rangle} = \sum_{i=0}^{M}\sum_{j=0}^{M} \frac{\zeta_{a,i}\ \zeta_{b,j}}{2\left(1+\delta_{m,0}\right)}\left(\delta_{m,i+j} + \delta_{m,i-j} + \delta_{m,-i+j} + \delta_{m,-i-j}\right). \tag{B.7}$$

Third order monomials are expanded in a similar fashion to second order monomials,

$$z_a z_b z_c = \left(\sum_{i=0}^{M} \zeta_{a,i} \cos\left(\frac{i\pi x}{\ell}\right)\right)\left(\sum_{j=0}^{M} \zeta_{b,j} \cos\left(\frac{j\pi x}{\ell}\right)\right) \left(\sum_{k=0}^{M} \zeta_{c,k} \cos\left(\frac{k\pi x}{\ell}\right)\right), \tag{B.8a}$$

$$= \sum_{i=0}^{M}\sum_{j=0}^{M}\sum_{k=0}^{M} \zeta_{a,i}\zeta_{b,j}\zeta_{c,k} \cos\left(\frac{i\pi x}{\ell}\right)\cos\left(\frac{j\pi x}{\ell}\right)\cos\left(\frac{k\pi x}{\ell}\right), \tag{B.8b}$$

$$= \sum_{i=0}^{M}\sum_{j=0}^{M}\sum_{k=0}^{M} \frac{\zeta_{a,i}\zeta_{b,j}\zeta_{c,k}}{4}\left(\cos\left(\frac{(i+j+k)\pi x}{\ell}\right) + \cos\left(\frac{(i+j-k)\pi x}{\ell}\right) + \cos\left(\frac{(i-j+k)\pi x}{\ell}\right) + \cos\left(\frac{(-i+j+k)\pi x}{\ell}\right)\right). \tag{B.8c}$$

Once more, the normalized inner product distributes to each term in the series,

yielding

$$\frac{\langle \phi_m, z_a z_b z_c \rangle}{\langle \phi_m, \phi_m \rangle} = \sum_{i=0}^{M}\sum_{j=0}^{M}\sum_{k=0}^{M} \frac{\zeta_{a,i}\ \zeta_{b,j}\ \zeta_{c,k}}{4\,(1+\delta_{m,0})}(\delta_{m,i+j+k} + \delta_{m,i+j-k} + \delta_{m,i-j+k} + \delta_{m,-i+j+k} + \delta_{m,i-j-k} + \delta_{m,-i+j-k} + \delta_{m,-i-j+k} + \delta_{m,-i-j-k}) . \quad \text{(B.9)}$$

This pattern continues for higher order polynomials and provides a computationally efficient method of solving for and analyzing the Galerkin projection ODEs for the low order polynomial systems that we find in isothermal Arrhenius kinetics.

B.2 Sine and cosine basis functions: periodic boundary conditions

We extend the analysis from Section B.1 to consider a basis consisting of both sine and cosine functions, used for domains with periodic boundary conditions.

Since our basis functions are orthogonal and $\phi_0 = 1$, constants and first order monomials expand in the same manor as shown in Eqs. (B.2-B.4), while higher order terms require additional analysis.

Sine and cosine terms must be considered independently. The main reason for this is the differences in the trigonometric identities, which, in addition to Eq. (B.5), are,

$$\cos\left(\frac{i\pi x}{\ell}\right)\sin\left(\frac{j\pi x}{\ell}\right) = \frac{1}{2}\left(\sin\left(\frac{(i+j)\pi x}{\ell}\right) - \sin\left(\frac{(i-j)\pi x}{\ell}\right)\right), \quad \text{(B.10)}$$

$$\sin\left(\frac{i\pi x}{\ell}\right)\sin\left(\frac{j\pi x}{\ell}\right) = \frac{1}{2}\left(\cos\left(\frac{(i-j)\pi x}{\ell}\right) - \cos\left(\frac{(i-j)\pi x}{\ell}\right)\right). \quad \text{(B.11)}$$

We therefore segregate our series solution for z_a into the sum of a cosine series and the sum of a sine series:

$$z_a = z_a^c + z_a^s, \quad \text{(B.12)}$$

where

$$z_a^c = \sum_{\substack{i=0 \\ i\in\text{evens}}}^{M} \zeta_{a,i} \cos\left(\frac{i\pi x}{\ell}\right), \tag{B.13}$$

$$z_a^s = \sum_{\substack{i=1 \\ i\in\text{odds}}}^{M} \zeta_{a,i} \sin\left(\frac{(i+1)\pi x}{\ell}\right). \tag{B.14}$$

Using this segregation, second order monomials have three cases that need to be considered: i) $z_a^c z_b^c$, ii) $z_a^c z_b^s$, and iii) $z_a^s z_b^s$. Case i) yields a result similar to Eq. (B.7), where explicitly stating the index numbering for periodic basis functions yields,

$$\frac{\langle \phi_m, z_a^c z_b^c \rangle}{\langle \phi_m, \phi_m \rangle} = \sum_{\substack{i=0 \\ i\in\text{evens}}}^{M} \sum_{\substack{j=0 \\ j\in\text{evens}}}^{M} \frac{\zeta_{a,i}\ \zeta_{b,j}}{2\left(1+\delta_{m,0}\right)} \left(\delta_{m,i+j} + \delta_{m,i-j} + \delta_{m,-i+j} + \delta_{m,-i-j}\right), \tag{B.15a}$$

for $m \in$ evens. Cases ii) and iii) have similar results,

$$\frac{\langle \phi_m, z_a^c z_b^s \rangle}{\langle \phi_m, \phi_m \rangle} = \sum_{\substack{i=0 \\ i\in\text{evens}}}^{M} \sum_{\substack{j=1 \\ j\in\text{odds}}}^{M} \frac{\zeta_{a,i}\ \zeta_{b,j}}{2\left(1+\delta_{m,0}\right)} \left(\delta_{m,i+j} - \delta_{m,i-j-2} + \delta_{m,-i+j} - \delta_{m,-i-j-2}\right), \tag{B.15b}$$

for $m \in$ odds, and

$$\frac{\langle \phi_m, z_a^s z_b^s \rangle}{\langle \phi_m, \phi_m \rangle} = \sum_{\substack{i=1 \\ i\in\text{odds}}}^{M} \sum_{\substack{j=1 \\ j\in\text{odds}}}^{M} \frac{\zeta_{a,i}\ \zeta_{b,j}}{2\left(1+\delta_{m,0}\right)} \left(-\delta_{m,2+i+j} + \delta_{m,i-j} + \delta_{m,-i+j} - \delta_{m,-i-j-2}\right), \tag{B.15c}$$

for $m \in$ evens.

Combining Eqs. (B.15) yields the full summation which is used in the evolution

of amplitudes:

$$\frac{\langle \phi_m, z_a z_b \rangle}{\langle \phi_m, \phi_m \rangle} = \frac{\langle \phi_m, z_a^c z_b^c \rangle}{\langle \phi_m, \phi_m \rangle} + \frac{\langle \phi_m, z_a^s z_b^s \rangle}{\langle \phi_m, \phi_m \rangle}, \tag{B.16}$$

for $m \in$ evens and

$$\frac{\langle \phi_m, z_a z_b \rangle}{\langle \phi_m, \phi_m \rangle} = \frac{\langle \phi_m, z_a^c z_b^s \rangle}{\langle \phi_m, \phi_m \rangle} + \frac{\langle \phi_m, z_b^c z_a^s \rangle}{\langle \phi_m, \phi_m \rangle}, \tag{B.17}$$

for $m \in$ odds, where the $z_b^c z_a^s$ term comes from Eq. (B.15b), with the indices switched.

We consider sine and cosine terms separately in third order monomials again, yielding four different cases: i) $z_a^c z_b^c z_c^c$, ii) $z_a^c z_b^c z_c^s$, iii) $z_a^c z_b^s z_c^s$, and iv) $z_a^s z_b^s z_c^s$. Case i) is similar to Eq. (B.9), where explicitly stating the index numbering for periodic basis functions yields:

$$\begin{aligned}\frac{\langle \phi_m, z_a^c\ z_b^c\ z_c^c \rangle}{\langle \phi_m, \phi_m \rangle} \;=\; & \sum_{\substack{i=0 \\ i\in\text{evens}}}^{M} \sum_{\substack{j=0 \\ j\in\text{evens}}}^{M} \sum_{\substack{k=0 \\ k\in\text{evens}}}^{M} \frac{\zeta_{a,i}\ \zeta_{b,j}\ \zeta_{c,k}}{4\,(1+\delta_{m,0})} (\delta_{m,i+j+k} + \delta_{m,i+j-k} \\ & + \delta_{m,i-j+k} + \delta_{m,-i+j+k} + \delta_{m,i-j-k} + \\ & \delta_{m,-i+j-k} + \delta_{m,-i-j+k} + \delta_{m,-i-j-k}) \,,\end{aligned} \tag{B.18a}$$

for $m \in$ evens.

Cases ii), iii), and iv) have similar results,

$$\begin{aligned}\frac{\langle \phi_m, z_a^c\ z_b^c\ z_c^s \rangle}{\langle \phi_m, \phi_m \rangle} \;=\; & \sum_{\substack{i=0 \\ i\in\text{evens}}}^{M} \sum_{\substack{j=0 \\ j\in\text{evens}}}^{M} \sum_{\substack{k=1 \\ k\in\text{odds}}}^{M} \frac{\zeta_{a,i}\ \zeta_{b,j}\ \zeta_{c,k}}{4\,(1+\delta_{m,0})} (\delta_{m,i+j+k} + \delta_{m,-i-j+k} \\ & + \delta_{m,i-j+k} + \delta_{m,-i+j+k} - \delta_{m,-i-j-k-2} \\ & - \delta_{m,i+j-k-2} - \delta_{m,-i+j-k-2} - \delta_{m,i-j-k-2}) \,,\end{aligned} \tag{B.18b}$$

for $m \in$ odds,

$$\frac{\langle \phi_m, z_a^c\ z_b^s\ z_c^s \rangle}{\langle \phi_m, \phi_m \rangle} = \sum_{\substack{i=0 \\ i\in\text{evens}}}^{M} \sum_{\substack{j=1 \\ j\in\text{odds}}}^{M} \sum_{\substack{k=1 \\ k\in\text{odds}}}^{M} \frac{\zeta_{a,i}\ \zeta_{b,j}\ \zeta_{c,k}}{4\,(1+\delta_{m,0})} (\delta_{m,i+j-k} + \delta_{m,i-j+k} + \delta_{m,-i-j+k} + \delta_{m,-i+j-k} - \delta_{m,i+j+k+2} - \delta_{m,-i+j+k+2} - \delta_{m,-i-j-k-2} - \delta_{m,i-j-k-2}), \quad \text{(B.18c)}$$

for $m \in$ evens, and

$$\frac{\langle \phi_m, z_a^s\ z_b^s\ z_c^s \rangle}{\langle \phi_m, \phi_m \rangle} = \sum_{\substack{i=1 \\ i\in\text{odds}}}^{M} \sum_{\substack{j=1 \\ j\in\text{odds}}}^{M} \sum_{\substack{k=1 \\ k\in\text{odds}}}^{M} \frac{\zeta_{a,i}\ \zeta_{b,j}\ \zeta_{c,k}}{4\,(1+\delta_{m,0})} (\delta_{m,i+j-k} + \delta_{m,i-j+k} + \delta_{m,-i+j+k} + \delta_{m,-i-j-k} - \delta_{m,-i-j+k-2} - \delta_{m,-i+j-k-2} - \delta_{m,i-j-k-2} - \delta_{m,i+j+k+2}), \quad \text{(B.18d)}$$

for $m \in$ odds.

Combining Eqs. (B.18) yields the full product of the summations, which is used in the evolution of amplitudes:

$$\frac{\langle \phi_m, z_a\ z_b\ z_c \rangle}{\langle \phi_m, \phi_m \rangle} = \frac{\langle \phi_m, z_a^c\ z_b^c\ z_c^c \rangle}{\langle \phi_m, \phi_m \rangle} + \frac{\langle \phi_m, z_a^c\ z_b^s\ z_c^s \rangle}{\langle \phi_m, \phi_m \rangle} + \frac{\langle \phi_m, z_b^c\ z_a^s\ z_c^s \rangle}{\langle \phi_m, \phi_m \rangle} + \frac{\langle \phi_m, z_c^c\ z_a^s\ z_b^s \rangle}{\langle \phi_m, \phi_m \rangle}, \quad \text{(B.19)}$$

for $m \in$ evens, and

$$\frac{\langle \phi_m, z_a\ z_b\ z_c \rangle}{\langle \phi_m, \phi_m \rangle} = \frac{\langle \phi_m, z_a^c\ z_b^c\ z_c^s \rangle}{\langle \phi_m, \phi_m \rangle} + \frac{\langle \phi_m, z_b^c\ z_a^c\ z_c^s \rangle}{\langle \phi_m, \phi_m \rangle} + \frac{\langle \phi_m, z_c^c\ z_a^c\ z_b^s \rangle}{\langle \phi_m, \phi_m \rangle} + \frac{\langle \phi_m, z_a^s\ z_b^s\ z_c^s \rangle}{\langle \phi_m, \phi_m \rangle}, \quad \text{(B.20)}$$

for $m \in$ odds, where the terms that were not explicitly defined above come from Eq. (B.18b) and Eq. (B.18c), with the indices switched.

These relations provide a computationally efficient method to solve for the

rate of change equations of the amplitudes in a Galerkin projection on a periodic domain, provided the governing PDEs are low-order polynomials.

APPENDIX C

BLOCK JACOBIAN MATRIX

We evaluate the Jacobian matrix of a system of ODEs for amplitude evolution defined by the Galerkin projection in the neighborhood of a spatially homogeneous set of amplitudes ($\zeta_{i,m} = 0$ for all i and $m \geq 1$). This analysis is applicable for any set of orthogonal basis functions, ϕ_m for $m = 0, \ldots, M$, (as long as ϕ_0 is a spatially homogeneous basis function) and for an arbitrary function, $\dot{\omega}_i(z_j)$ for $i, j = 1, \ldots, R$. We choose to order the Galerkin projection species amplitude vector first by basis function and then by species by defining $\{i, m\} = mR + i$. Therefore, the vector, $\zeta_{\{i,m\}} = \zeta_{i,m}$ for $i = 1, \ldots, R$ and $m = 0, \ldots, M$, contains all $R(M+1)$ elements of the species amplitudes sorted in our prescribed fashion. The reaction source terms become ordered as

$$\dot{\Omega}_{\{i,m\}} = \frac{\langle \phi_m, \dot{\Omega}_i(\sum_{n=0}^{M} \zeta_{j,n}\phi_n)\rangle}{\langle \phi_m, \phi_m \rangle}, \text{ for } i, j = 1, \ldots, R \text{ and } m = 0, \ldots, M. \quad \text{(C.1)}$$

To find the Jacobian of a point in the spatially homogeneous subspace, $\zeta_{i,m}^{SH}$ (where $\zeta_{i,m}^{SH} = 0$ for $m > 0$), we then take the partial derivative of the Galerkin projection with respect to an arbitrary species amplitude,

$$\mathbf{J}_{\{i,m\},\{j,n\}} = \frac{\partial}{\partial \zeta_{j,n}} \left(\frac{\langle \phi_m, \dot{\Omega}_i(\sum_{n=0}^{M} \zeta_{j,n}\phi_n)\rangle}{\langle \phi_m, \phi_m \rangle} - \frac{m^2\pi^2\mathcal{D}}{\ell^2}\zeta_{i,m} \right) \Bigg|_{\zeta=\zeta^{SH}}. \quad \text{(C.2)}$$

We can distribute the partial derivative into the linear operators and apply them at the point in the spatially homogeneous subspace to get

$$\mathbf{J}_{\{i,m\},\{j,n\}} = \frac{\langle \phi_m, \frac{\partial}{\partial \zeta_{j,n}} \dot{\Omega}_i (\sum_{\hat{n}=0}^{M} \zeta_{\hat{j},\hat{n}} \phi_{\hat{n}}) \Big|_{\zeta=\zeta^{SH}} \rangle}{\langle \phi_m, \phi_m \rangle} - \frac{m^2 \pi^2 \mathcal{D}}{\ell^2} \left. \frac{\partial \zeta_{i,m}}{\partial \zeta_{j,n}} \right|_{\zeta=\zeta^{SH}}. \quad \text{(C.3)}$$

The partial derivative in the diffusion term can be reduced to a Kronecker delta function,

$$\mathbf{J}_{\{i,m\},\{j,n\}} = \frac{\langle \phi_m, \frac{\partial}{\partial \zeta_{j,n}} \dot{\Omega}_i (\sum_{\hat{n}=0}^{M} \zeta_{\hat{j},\hat{n}} \phi_{\hat{n}}) \Big|_{\zeta=\zeta^{SH}} \rangle}{\langle \phi_m, \phi_m \rangle} - \frac{m^2 \pi^2 \mathcal{D}}{\ell^2} \delta_{\{i,m\},\{j,n\}}. \quad \text{(C.4)}$$

Then we take the derivative of the arbitrary nonlinear reaction function. The derivative can be reduced to be with respect to z_j, since it is evaluated at the spatially homogeneous z^{SH}. Because of the chain rule, the basis function, ϕ_n, becomes a coefficient of the derivative, yielding

$$\mathbf{J}_{\{i,m\},\{j,n\}} = \frac{\langle \phi_m, \phi_n \frac{\partial \dot{\Omega}_i}{\partial z_j} \rangle}{\langle \phi_m, \phi_m \rangle} - \frac{m^2 \pi^2 \mathcal{D}}{\ell^2} \delta_{\{i,m\},\{j,n\}}. \quad \text{(C.5)}$$

Finally, the orthogonality of the basis functions will yield another Kronecker delta function, resulting in

$$\mathbf{J}_{\{i,m\},\{j,n\}} = \frac{\partial \dot{\Omega}_i}{\partial z_j} \delta_{m,n} - \frac{m^2 \pi^2 \mathcal{D}}{\ell^2} \delta_{\{i,m\},\{j,n\}}. \quad \text{(C.6)}$$

This Jacobian is in the form of a block diagonal matrix. The first term, $(\partial \dot{\Omega}_i / \partial z_j) \delta_{m,n}$, populates the $R \times R$ diagonal blocks with the spatially homogeneous Jacobian matrix. The second term, $(m^2 \pi^2 \mathcal{D} / \ell^2) \delta_{\{i,m\},\{j,n\}}$, yields a diffusion component along

the diagonal of each block.

APPENDIX D

BIFURCATION CONNECTION TO PHYSICAL WAVELENGTH

To simplify the process of finding equilibria in reaction-diffusion systems for a variety of domain lengths, ℓ, we seek to generalize the equilibria we find at one particular domain length. In this exercise we obtain a connection between the spatial structure of spatially inhomogeneous equilibria (such as the $\hat{R}$ equilibria identified in the pitchfork bifurcation analysis) and the physical wavelength of the basis functions.

We examine an arbitrary equilibrium solution, $\zeta^e_{i,m}$, in a Galerkin projection. This equilibrium satisfies the steady state equation,

$$\dot{\Omega}_{i,m}(\zeta^e_{j,n}) - \frac{m^2\pi^2\mathcal{D}}{\ell^2}\zeta^e_{i,m} = 0, \quad \text{for } i,j \in [1,R] \text{ and } m,n \in [0,M]. \tag{D.1}$$

Now, we examine an analogous Galerkin projection on an $\hat{m}$ times longer spatial domain, $x \in [0, \hat{m}\ell]$, where $\hat{m}$ is an integer greater than one. An analogous equilibrium, $\hat{\zeta}^e_{i,m}$, will exist on this longer domain length whose amplitudes that are a multiple of $\hat{m}$ are equal to the amplitudes of the original equilibrium, $\zeta^e_{i,m}$ on length ℓ,

$$\hat{\zeta}^e_{i,(\hat{m}\times m)} = \zeta^e_{i,m}, \quad \text{for } i \in [1,R] \text{ and } m \in [0,M], \tag{D.2}$$

and the remaining amplitudes are zero, $\hat{\zeta}^e_{i,m} = 0$, for $i \in [1,R]$, and for m not an integer multiple of m.

Each multiple of $\hat{m}$ amplitude in the $\hat{\zeta}^e_{i,m}$ equilibrium satisfies a steady state equation identical to a $\zeta^e_{i,m}$ equilibrium,

$$\dot{\Omega}_{i,(\hat{m}\times m)}(\hat{\zeta}^e_{j,(\hat{m}\times n)}) - \frac{(\hat{m}m)^2\pi^2\mathcal{D}}{(\hat{m}\ell)^2}\hat{\zeta}^e_{i,(\hat{m}\times m)} = 0, \text{ for } i,j \in [1,R], \text{ and } m,n \in [0,M]. \tag{D.3}$$

A simple algebraic reduction reveals that the diffusion term is identical, while the reaction term is not as apparent. The reaction term can be shown to be identical when using the definition of $\dot{\Omega}_{i,m}$ in the Galerkin projection. For cosine basis functions this is

$$\frac{\int_0^\ell \cos\left(\frac{m\pi x}{\ell}\right)\dot{\Omega}_i(z^e_{\hat{i}}(x))dx}{\int_0^\ell \cos^2\left(\frac{m\pi x}{\ell}\right)dx} = \frac{\int_0^{2\ell} \cos\left(\frac{\hat{m}m\pi x}{\hat{m}\ell}\right)\dot{\Omega}_i(z^e_{\hat{i}}(x))}{\int_0^{2\ell} \cos^2\left(\frac{\hat{m}m\pi x}{\hat{m}\ell}\right)dx}, \tag{D.4}$$

which is true because the basis functions force the Galerkin projection of the equilibrium solution to be spatially symmetric about ℓ, $z^e_i(x) = z^e_i(2\ell - x)$. This result is the same for sine and cosine basis functions. The steady state equations for the $\hat{\zeta}^e_{i,m}$ amplitudes that are not multiples of $\hat{m}$ are also satisfied

$$\dot{\Omega}_{i,m}(\hat{\zeta}^e_{j,n}) - \frac{m^2\pi^2\mathcal{D}}{(\hat{m}\ell)^2}\hat{\zeta}^e_{i,m} = 0, \tag{D.5}$$

for $i,j \in [1,R]$, $n \in [0, \hat{m}\times M]$, and m not an integer multiple of $\hat{m}$; the diffusion term is zero because each $\hat{\zeta}^e_{i,m}$ amplitude where m is not a multiple of $\hat{m}$ is also zero. The reaction term can be shown to be zero by expanding the inner product definition of $\dot{\Omega}_{i,m}$ and using trigonometric identities,

$$\int_0^\ell \cos\left(\frac{m\pi x}{\ell}\right)\dot{\Omega}_i(z^e_{\hat{i}}(x))dx = 0, \quad \text{for } m \text{ not a multiple of } \hat{m}. \tag{D.6}$$

Since each monomial of $\dot{\Omega}$, when expanded using trigonometric identities, results in

a cosine of the sums or differences of the basis mode number, all terms that are not multiples of $\hat{m}$ are zero; therefore, the resulting polynomial will only have nonzero terms in multiples of $\hat{m}$. The orthogonality of the basis functions guarantees the resulting $\dot{\Omega}_{i,m}$ will also only have nonzero terms in multiples of $\hat{m}$, which have already been shown to be in equilibrium. Therefore, any equilibrium solution of the Galerkin projection on domain length ℓ will have analogous solutions on domains of integer multiples of that length, $\hat{m}\ell$; this corresponds to equilibria manifolds with identical physical wavelengths in function space.

APPENDIX E

POINCARÉ SPHERE

To evaluate the dynamics at infinity, our domain is projected onto the Poincaré sphere [51], mapping $\boldsymbol{\zeta} \in \mathbb{R}^{M+1} \mapsto \boldsymbol{\eta} \in \mathbb{R}^{M+2}$ via the coordinate transformation,

$$\eta_i = \frac{\zeta_i}{\sqrt{1+\sum_{m=0}^{M}\zeta_m^2}}, \text{ for } i = 0, \ldots, M, \tag{E.1a}$$

$$\eta_{M+1} = \frac{1}{\sqrt{1+\sum_{m=0}^{M}\zeta_m^2}}. \tag{E.1b}$$

Under this transformation, the η-coordinates are constrained by

$$\sum_{i=0}^{M+1}\eta_i^2 = 1, \tag{E.2}$$

which means that the ζ-coordinate system is mapped onto an $(M+1)$-dimensional unit hypersphere in η-space. The inverse transformation exists,

$$\zeta_i = \frac{\eta_i}{\eta_{M+1}}, \text{ for } i = 0, \ldots, M. \tag{E.3}$$

When we only examine η_i for $i = 0, \ldots, M$, we project the unit hypersphere into an $(M+1)$-dimensional space, and the constraint in Eq. (E.2) becomes an inequality,

$$\sum_{i=0}^{M}\eta_i^2 \leq 1. \tag{E.4}$$

For this transformation, in the limit as $\zeta_i \to \infty$, for any $i = 0, \ldots, M$, η_i becomes 1. More generally, in the limit as any set of $\zeta_i \to \infty$, the resulting transformed variables, η_i, are finite and constrained by

$$\sum_{i=0}^{M} \eta_i^2 = 1. \tag{E.5}$$

Therefore, the points at infinity in ζ-coordinates are mapped onto an M-dimensional unit hypersphere in the η-coordinates. For finite values of ζ_i,

$$\sum_{i=0}^{M} \eta_i^2 < 1; \tag{E.6}$$

therefore, all of the finite dynamics in the ζ-coordinates are contained within the M-dimensional unit sphere in the η-coordinates. In the Poincaré sphere coordinate transformation, the entire ζ-coordinate system, both finite and infinite, is mapped onto a unit sphere. This allows the entire system's dynamics to be examined, including the dynamics at infinity.

APPENDIX F

MANIFOLD ATTRACTIVENESS METRIC FROM STRETCHING RATES

We adopt a stretching based metric similar to Adrover et al. [10] to quantify the attractiveness at a point on an invariant one-dimensional manifold, $\mathbf{z}_{\mathscr{M}}$, in an R-dimensional vector space governed by the ODEs

$$\frac{d\mathbf{z}}{dt} = \mathbf{f}(\mathbf{z}). \tag{F.1}$$

At $\mathbf{z}_{\mathscr{M}}$ there is a tangent vector,

$$\boldsymbol{v}_t = \mathbf{f}(\mathbf{z}_{\mathscr{M}}), \tag{F.2}$$

which can be normalized into a unit tangent vector,

$$\boldsymbol{\alpha}_t = \frac{\boldsymbol{v}_t}{\|\boldsymbol{v}_t\|}. \tag{F.3}$$

Using $\boldsymbol{\alpha}_t$ as one basis vector, we can generate an orthonormal basis that spans the R-dimensional vector space by finding $R-1$ orthonormal vectors, $\boldsymbol{\alpha}_{ni}$ for $i = 1, \ldots, R-1$, that span the space normal to the tangent vector.

A vector, $\boldsymbol{v}$, in the neighborhood of $\mathbf{z}_{\mathscr{M}}$ changes with the rate of

$$\frac{d\boldsymbol{v}}{dt} = \mathbf{J} \cdot \boldsymbol{v}, \tag{F.4}$$

where $\mathbf{J}$ is the Jacobian matrix evaluated at $\mathbf{z}_{\mathscr{M}}$,

$$\mathbf{J} = \left.\frac{\partial \mathbf{f}}{\partial \mathbf{z}}\right|_{\mathbf{z}_{\mathscr{M}}}. \tag{F.5}$$

To find the tangent stretching rate, we project the rate of change of $\boldsymbol{\alpha}_t$ onto the tangent direction by taking its inner product with $\boldsymbol{\alpha}_t$,

$$\sigma_t(\mathbf{z}_{\mathscr{M}}(t)) = \boldsymbol{\alpha}_t^T \cdot \mathbf{J} \cdot \boldsymbol{\alpha}_t. \tag{F.6}$$

Similarly, there are $R-1$ normal stretching rates:

$$\sigma_{ni}(\mathbf{z}_{\mathscr{M}}(t)) = \boldsymbol{\alpha}_{ni}^T \cdot \mathbf{J} \cdot \boldsymbol{\alpha}_{ni}, \text{ for } i = 1, \ldots, R-1. \tag{F.7}$$

We note that these stretching ratios have no contribution from the antisymmetric part of the Jacobian matrix; therefore, identical results are found when considering the symmetric part of the Jacobian matrix. The stretching ratios,

$$\hat{r}_i(\mathbf{z}_{\mathscr{M}}(t)) = \frac{\sigma_{ni}(\mathbf{z}_{\mathscr{M}}(t))}{|\sigma_t(\mathbf{z}_{\mathscr{M}}(t))|}, \text{ for } i = 1, \ldots, R-1, \tag{F.8}$$

provide a metric of the rate of normal stretching to tangential stretching, which quantifies how attractive the one-dimensional manifold is in each of the $R-1$ normal directions. To be attractive, we require the normal stretching rates to be negative; the more negative the stretching ratio, $\hat{r}_i(\mathbf{z}_{\mathscr{M}}(t))$, the more attractive the manifold.

When this stretching ratio is evaluated along the SIM, we find a singularity where the tangent stretching rate is zero. Since the SIM is initially tangent to the unstable eigenvector of the SIM-BIC, the tangent stretching rate is equal

to the corresponding eigenvalue and therefore is positive: $\sigma_t(\mathbf{z}_{\mathscr{M}}(0)) > 0$. The SIM is also tangent to the stable eigenvector with the slowest time scale in the neighborhood of the physical equilibrium; therefore, at this point on the manifold, the tangent stretching rate is equal to the corresponding eigenvalue, which is negative: $\sigma_t(\mathbf{z}_{\mathscr{M}}(\infty)) < 0$. The tangent stretching rates are a continuous function along the manifold; therefore, somewhere on the SIM there is a point that has a zero tangent stretching rate, $\sigma_t(\mathbf{z}_{\mathscr{M}}(t)) = 0$. To describe this, we use a simple thought experiment comparing the tangent stretching rate to accelerating in the vector field, since the Jacobian describes the local change in the rate of change vector. Near the SIM-BIC the positive stretching rate indicates the dependent variables are acceleration along the manifold in phase space. Near the physical equilibrium the negative stretching rate indicates a deceleration of the dependent variables in phase space towards their steady state values. Somewhere along the SIM, the dependent variables need to change from accelerating to decelerating, which indicates a zero tangent stretching rate.

This becomes a problem when using the stretching ratios to quantify attractiveness, since every SIM will be infinitely attractive at a point along the manifold when using the local stretching ratio. One could eliminate this issue by evaluating the normal stretching rate; however, without comparison to a tangent stretching rate, the stretching rate alone does not accurately quantify attractiveness. To remedy this problem, we suggest a modified stretching ratio using the slow eigenvalue at the physical equilibrium, $\mathbf{z}_{\mathscr{M}}(\infty)$, as the tangent stretching rate:

$$r_i(\mathbf{z}_{\mathscr{M}}(t)) = \frac{\sigma_{ni}(\mathbf{z}_{\mathscr{M}}(t))}{|\sigma_t(\mathbf{z}_{\mathscr{M}}(\infty))|}, \text{ for } i = 1, \ldots, R-1, \tag{F.9}$$

thus removing the singularity in the stretching ratio metric; however, $r_i(\mathbf{z}_{\mathscr{M}}(t))$

may not provide an accurate metric when tangent stretching rates have large variations along the manifold.

Since the manifold is constructed by integrating a trajectory that has an exponential growth away from the SIM-BIC and an exponential decay to the physical equilibrium, the length of the manifold does not directly correspond to the number of points which are calculated to approximate the manifold. Therefore, to plot metrics, such as the stretching ratios, along the manifold, we use the following manifold length function:

$$\begin{aligned} \hat{s}(\mathbf{z}_{\mathscr{M}}(t)) &= \int_0^t \sqrt{\sum_{i=1}^{R} \left(\left. \frac{dz_i}{d\hat{t}} \right|_{\mathbf{z}_{\mathscr{M}}(\hat{t})} \right)^2} d\hat{t}, \\ &= \int_0^t \sqrt{\sum_{i=1}^{R} f_i \left(\mathbf{z}_{\mathscr{M}}(\hat{t}) \right)^2} d\hat{t}. \end{aligned} \tag{F.10}$$

It is useful to normalize the distance function by the total length of the manifold,

$$s(\mathbf{z}_{\mathscr{M}}(t)) = \frac{\hat{s}(\mathbf{z}_{\mathscr{M}}(t))}{\hat{s}(\mathbf{z}_{\mathscr{M}}(\infty))}. \tag{F.11}$$

For systems with $R > 2$, we illustrate a shortcoming of our metric by evaluating two simple systems. The system first is governed by the ODEs,

$$\frac{dz_1}{dt} = \frac{1}{20}(1 - z_1^2), \tag{F.12a}$$

$$\frac{dz_2}{dt} = -2z_2 - \frac{35}{16} z_3, \tag{F.12b}$$

$$\frac{dz_3}{dt} = z_2 + z_3. \tag{F.12c}$$

We identify the two finite roots, R_1 at $z = \{-1, 0, 0\}$ and R_2 at $z = \{1, 0, 0\}$, by

inspection. The Jacobian of the system is

$$J = \begin{bmatrix} -z_1/10 & 0 & 0 \\ 0 & -2 & -35/16 \\ 0 & 1 & 1 \end{bmatrix}, \tag{F.13}$$

which has eigenvalues of $\lambda = \{.1, -.25, -.75\}$ at R_1 and $\lambda = \{-.1, -.25, -.75\}$ at R_2. Assuming R_2 is the physical equilibrium, the heteroclinic orbit that connects R_1 to R_2 along the $z_2 = z_3 = 0$ axis is a branch of the SIM. The unit tangent vector along the SIM is $\boldsymbol{\alpha}_t = \{1, 0, 0\}$. A sketch of the phase space for this system is provided in Figure F.1. Let us evaluate sets of unit normal vectors: i) $\boldsymbol{\alpha}_{n,1} = \{0, 1, 0\}$ and $\boldsymbol{\alpha}_{n,2} = \{0, 0, 1\}$, and ii) $\boldsymbol{\alpha}_{n,1} = \{0, 0.8271, 0.5621\}$ and $\boldsymbol{\alpha}_{n,2} = \{0, 0.8271, -0.5621\}$.

The normal stretching rates are constant along the manifold. For case i), the normal stretching rates are $\sigma_n(\mathbf{z}_{\mathscr{M}}) = \{-2, 1\}$ and the stretching ratios are $r_i(\mathbf{z}_{\mathscr{M}}) = \{-20, 10\}$, while for case ii), they are $\sigma_n(\mathbf{z}_{\mathscr{M}}) = \{-0.5, -0.5\}$ and $r_i(\mathbf{z}_{\mathscr{M}}) = \{-5, -5\}$. This simple example demonstrates how the results of our stretching ratio metric can vary based on the choice of normal vectors. This effect becomes more pronounced when the angles between the eigenvectors of the Jacobian are small.

The second system is similar to the previous, and governed by the ODEs,

$$\frac{dz_1}{dt} = \frac{1}{20}(1 - z_1^2), \tag{F.14a}$$

$$\frac{dz_2}{dt} = -2z_2 - \frac{35}{16}z_3 + 2(1 - z_1^2)z_3, \tag{F.14b}$$

$$\frac{dz_3}{dt} = z_2 + z_3. \tag{F.14c}$$

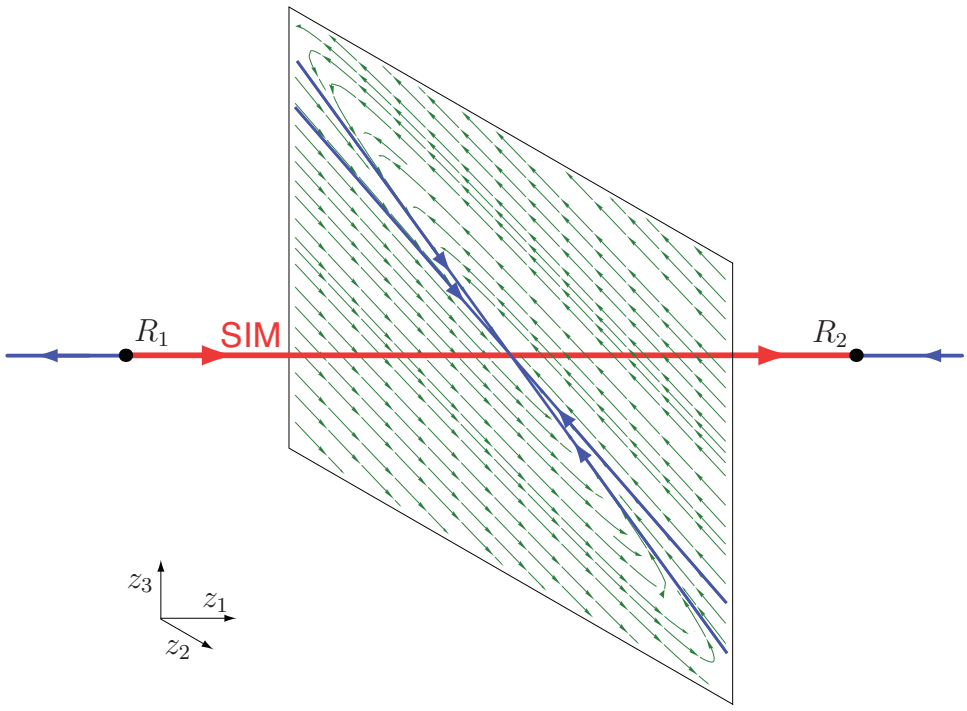

Figure F.1. Phase space sketch of the system governed by Eqs. (F.12).

This system has the same two finite roots, R_1 at $z = \{-1, 0, 0\}$ and R_2 at $z = \{1, 0, 0\}$. The Jacobian of the system is

$$J = \begin{bmatrix} -z_1/10 & 0 & 0 \\ -4z_1z_3 & -2 & -35/16 + 2(1 - z_1^2) \\ 0 & 1 & 1 \end{bmatrix}, \tag{F.15}$$

which again has eigenvalues of $\lambda = \{.1, -.25, -.75\}$ at R_1 and $\lambda = \{-.1, -.25, -.75\}$ at R_2. There is a SIM branch defined by the heteroclinic orbit that connects R_1 to R_2 along the $z_2 = z_3 = 0$ axis, which has identical dynamics as the SIM branch for Eqs. (F.12); however, we find that this branch does not attract neighboring trajectories along the entire manifold.

A sketch of the phase space for this second system is provided in Figure F.2, where we see an unstable eigenvector is oriented in a normal direction. Figure F.3 is a projection of phase space that shows the neighboring blue trajectories diverging away from the red SIM.

For the system governed by Eqs. (F.14), the normal stretching rates vary along the manifold. At $z_1 = 0$ on the SIM, for the two choices of normal vectors, $\boldsymbol{\alpha}_{n,1} = \{0, 1, 0\}$ and $\boldsymbol{\alpha}_{n,2} = \{0, 0, 1\}$, and $\boldsymbol{\alpha}_{n,1} = \{0, 0.7942, 0.6077\}$ and $\boldsymbol{\alpha}_{n,2} = \{0, -0.6077, 0.7942\}$, the normal stretching rates are $\sigma_n(\mathbf{z}_{\mathscr{M}}) = \{-2, 1\}$ and $\sigma_n(\mathbf{z}_{\mathscr{M}}) = \{-0.5, -0.5\}$, respectively. This shows that also for this unstable manifold, results will again vary with the choice of normal vector.

While this technique is able to provide some insights into local stretching rates and ratios, it does depend on the choice of normal vectors and fails to accurately quantify attractiveness. Identifying the maximum and minimum local normal stretching rates is a simple exercise that can be useful. Having all negative normal

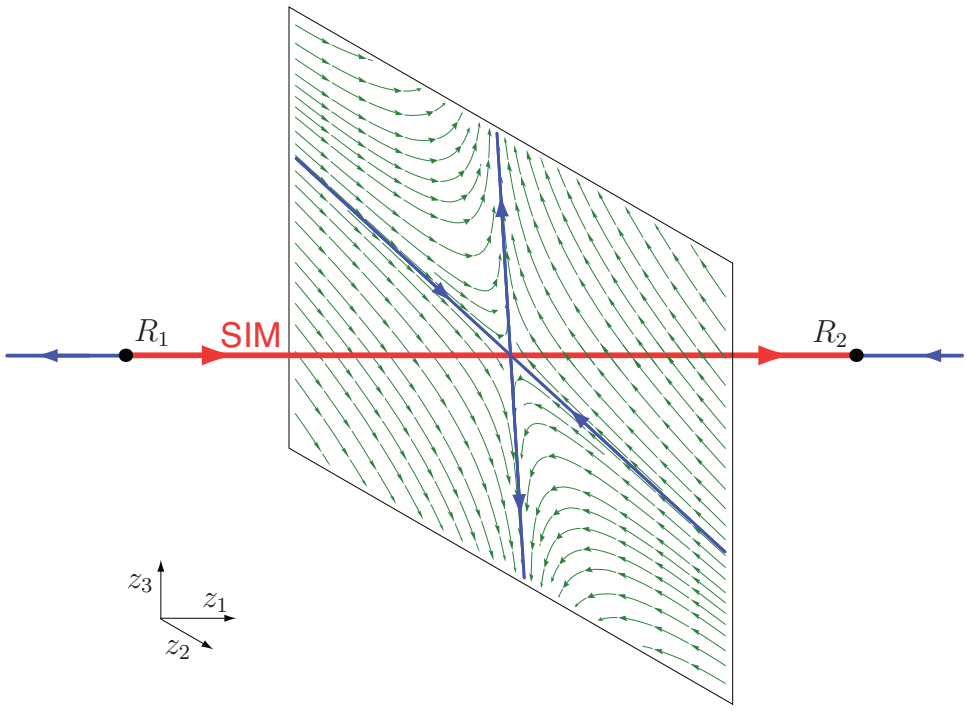

Figure F.2. Phase space sketch of the system governed by Eqs. (F.14).

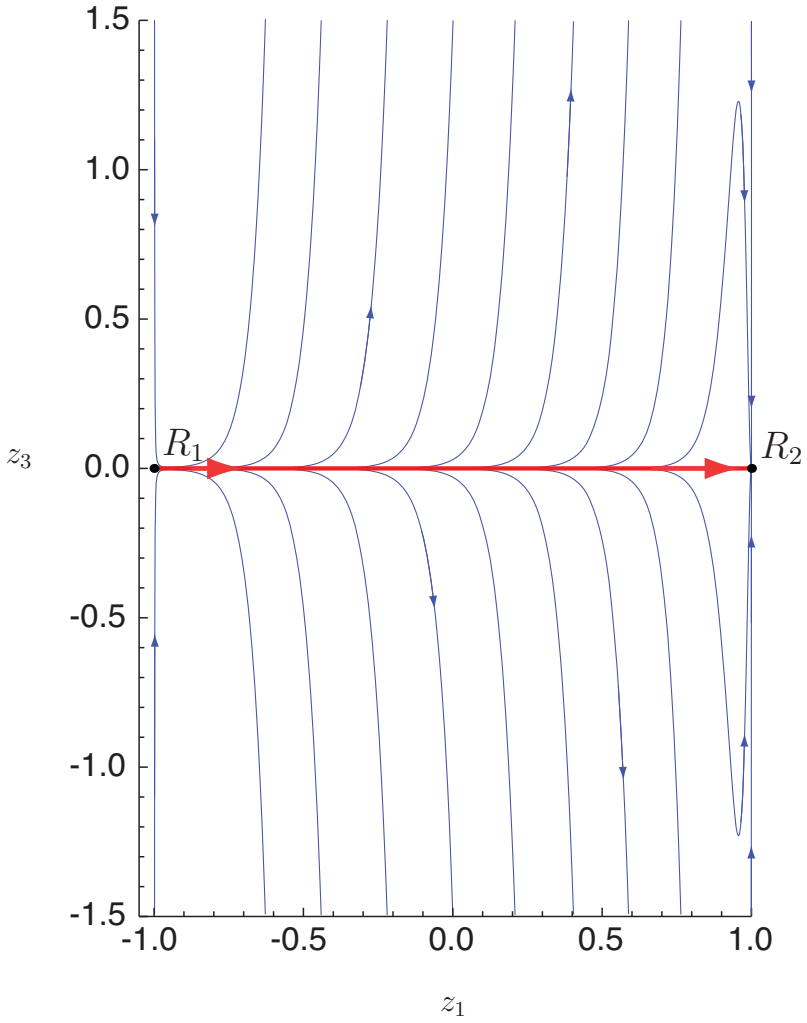

Figure F.3. Phase space projection of the SIM with diverging nearby trajectories for system governed by Eqs. (F.14).

stretching rates is a sufficient (but not necessary) condition for a manifold to be locally attractive. Conversely, having at least one negative normal stretching rate is a necessary (but not sufficient) condition. Adrover et al. [10] describe a more careful selection of normal vectors for higher dimensional systems.

We introduce a new metric to evaluate attractiveness. This metric is based on two assumptions: i) the dynamics along the manifold are slower than the dynamics normal to the manifold, and ii) we admit a phase error when projecting onto the manifold. The first assumption can be verified a posteriori. The justification for these two assumptions are as follows. If the tangential dynamics occur at faster time scales than the normal dynamics, the linear assumption to build a Jacobian will break down as the trajectory will progress to a different location on the manifold before appreciable normal dynamics occur. The second assumption is what allows us to only consider changes in the normal plane. In general, a perturbation in the normal direction will change the dynamics tangent to the manifold as well; however, by admitting phase error we can ignore the changes in the tangent direction and only consider variations normal to the manifold by projecting the changes into the normal space.

After making these two assumptions we now consider all dynamics normal to manifold to quantify normal stretching rates. The tangent stretching rate along a one-dimensional manifold is shown in Eq. (F.6); the normal dynamics are now governed by a local normal Jacobian matrix. To build the normal Jacobian matrix, any orthonormal basis that spans the normal space of the manifold can be used:

$$\mathbf{Q}_n = \begin{bmatrix} | & & | \\ \boldsymbol{\alpha}_{n1} & \cdots & \boldsymbol{\alpha}_{nR-1}, \\ | & & | \end{bmatrix}, \tag{F.16}$$

where $\mathbf{Q}_n$ is an $R \times R-1$ rectangular matrix with orthonormal columns. The normal Jacobian is

$$\hat{\mathbf{J}} = \mathbf{Q}_n^T \cdot \mathbf{J} \cdot \mathbf{Q}_n, \tag{F.17}$$

which is an $R-1 \times R-1$ matrix. This matrix describes the local dynamics of perturbations in all normal directions constrained to the normal directions. As long as assumption i) is satisfied, the eigenvalues of the normal Jacobian matrix, λ_n, describe the attractiveness of the manifold. If all eigenvalues have negative real parts, then we say that point on the manifold is attractive; however, if any eigenvalues has a positive real part, we say that point on the manifold is repulsive.

The reciprocal of the real part of negative normal eigenvalues will give the time scales of decay to the manifold, $\tau_n = 1/\lambda_n$, and can be used to check assumption i). The time scale in the tangential direction is the reciprocal of the tangent stretching rate, $\tau_t = 1/\sigma_t(\mathbf{z}_{\mathscr{M}})$; if the normal time scales are all faster than the tangent time scale, then this analysis will provide accurate results.

Notice that the diagonal of the normal Jacobian matrix is composed of the individual normal stretching rates from the previous analysis. This means that for one-dimensional manifolds in two-dimensional systems (where there is only one choice for orthonormal basis) this analysis is consistent with the normal stretching metric of Adrover et al. [10].

This metric is independent of the choice of orthonormal basis and accurately describes the predicted behaviors of the two simple examples given earlier in this appendix. For the example in Eqs. (F.12), both normal eigenvalues are real and negative, $\lambda_n = \{-3/4, -1/4\}\ 1/s$, and constant along the entire length of the SIM. We verify assumption i) by finding the normal time scales, $\tau_n = \{4/3, 4\}\ s$, and comparing them to the tangential time scales $\tau_t \geq 10\ s$; for this example the

normal dynamics are faster than the tangential dynamics. For the example in Eqs. (F.14), the normal eigenvalues are real, but vary along the SIM as shown in Figure F.4; the black dotted line indicates where the normal eigenvalues are zero, the cyan lines are negative normal eigenvalues, and the magenta line are positive normal eigenvalues. This result shows that while the manifold is attractive in the neighborhood of the SIM-BIC, R_1, and the physical equilibrium, R_2, it is not attractive along the majority of the manifold between the two equilibria. This result is consistent with the trajectories shown in Figure F.3.

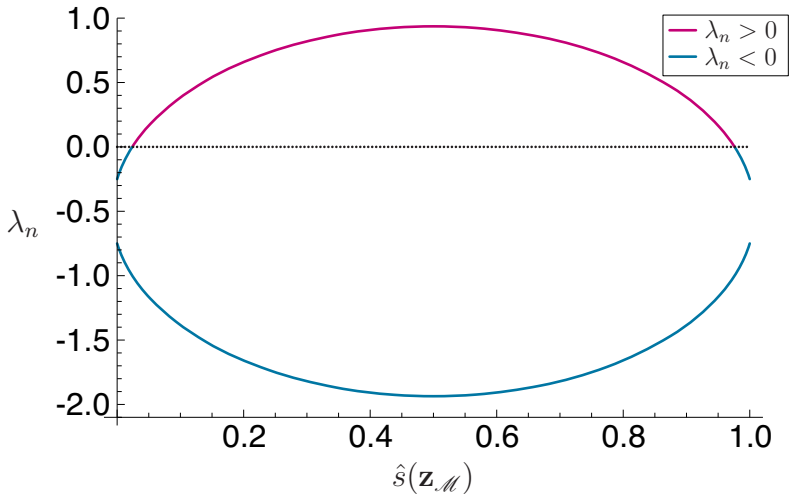

Figure F.4. Normal eigenvalues for system governed by Eqs. (F.14).

In Figure F.5, we demonstrate the normal eigenvalues for the two example problems: (a) shows the example governed by Eqs. (F.12), (b) shows the example governed by Eqs. (F.14). What Figure F.5 shows is the evolution of a manifold

of initial conditions that are all perturbed by ϵ away from the manifold at $z_{\mathscr{M}} = \{0, 0, 0\}$ for each system. The initial conditions for each case are shown on the left-most subfigures; each subsequent subfigure to the right depicts a later time. We admit phase error and only consider the dynamics in the directions normal to the SIM. Since for each of these systems the normal dynamics occur at faster time scales than the tangential dynamics, we can assume that these dynamics all occur in a linear neighborhood of the SIM at $z_{\mathscr{M}} = \{0, 0, 0\}$, which is shown as a red line from the lower left to the upper right. In this linear neighborhood, the real part of each eigenvalue indicates the rate of decay or grown and their associated eigenvector (shown as cyan and green arrows for stable and as magenta arrows for unstable) indicate the direction of those dynamics.

In case (a), there are two negative real normal eigenvalues, so the manifold is locally attractive. Note that there are positive normal stretching rates, so there is initial growth away from the SIM; however, the negative eigenvalues indicate that the local dynamics will result in a decay onto the manifold for all near-by trajectories. This can be seen in the later times as the dynamics of all initial conditions approach the manifold along the slow normal eigenvector.

In case (b), there is one positive and one negative real normal eigenvalue, indicating a locally repulsive manifold. The initial growth away from the SIM continues in the direction of the unstable normal eigenvector, and nearly all trajectories diverge away from the manifold at this point.

To explain the growth away from the SIM in Figure F.5(a) for short times, we can decompose the normal Jacobian into symmetric, $\hat{\mathbf{J}}_s$ and anti-symmetric $\hat{\mathbf{J}}_a$

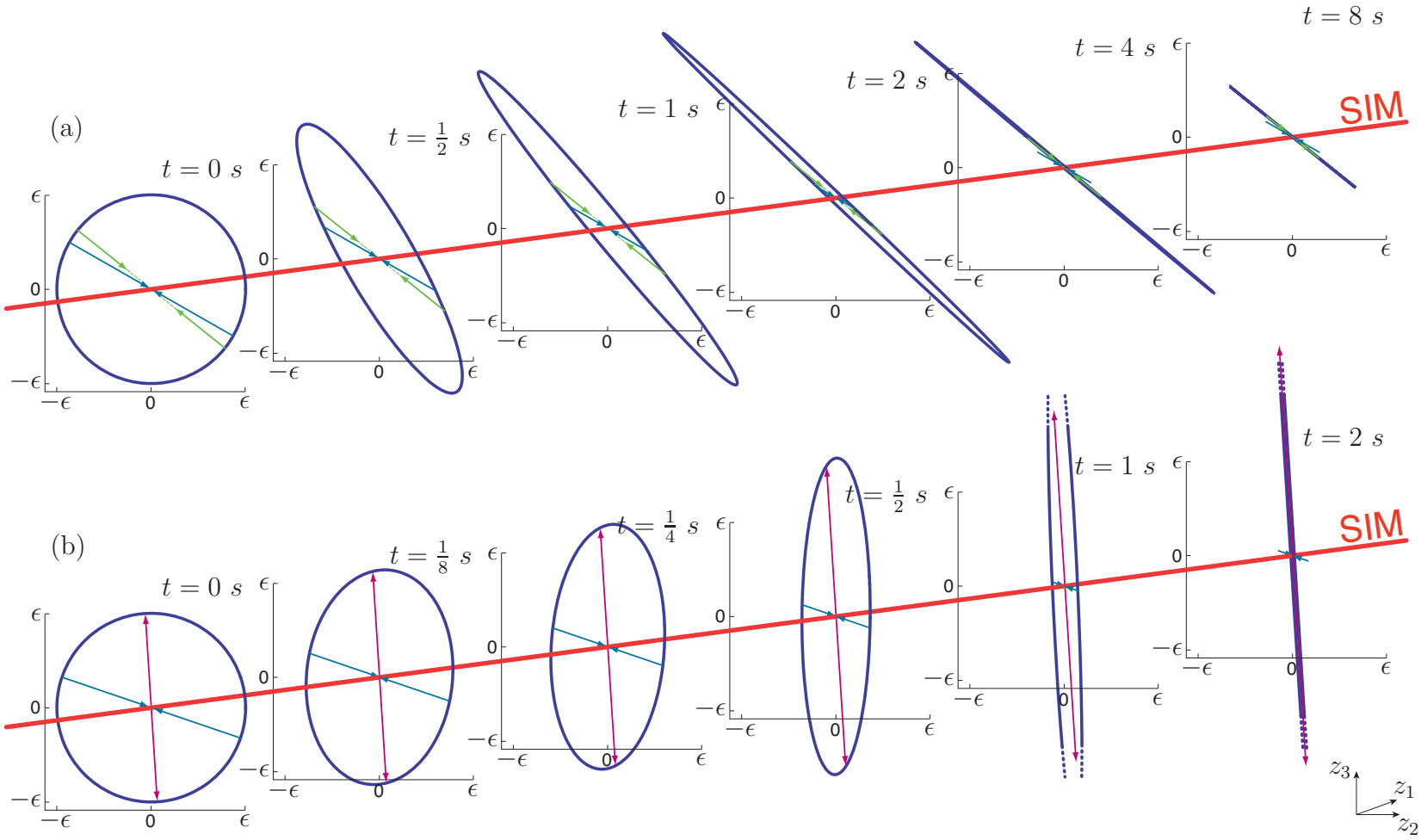

Figure F.5: Normal eigenvalues, local dynamics, and manifold attractiveness.

parts,

$$\hat{\mathbf{J}}_s = \frac{1}{2}(\hat{\mathbf{J}} + \hat{\mathbf{J}}^T), \tag{F.18a}$$

$$\hat{\mathbf{J}}_a = \frac{1}{2}(\hat{\mathbf{J}} - \hat{\mathbf{J}}^T). \tag{F.18b}$$

The normal Jacobian is the summation of the symmetric and anti-symmetric parts: $\hat{\mathbf{J}} = \hat{\mathbf{J}}_s + \hat{\mathbf{J}}_a$. For the system given in Eqs. (F.12) this decomposition results in the following matrices:

$$\hat{\mathbf{J}} = \begin{bmatrix} -2 & -35/16 \\ 1 & 1 \end{bmatrix}, \tag{F.19a}$$

$$\hat{\mathbf{J}}_s = \begin{bmatrix} -2 & -19/32 \\ -19/32 & 1 \end{bmatrix}, \tag{F.19b}$$

$$\hat{\mathbf{J}}_a = \begin{bmatrix} 0 & -51/32 \\ 51/32 & 0 \end{bmatrix}. \tag{F.19c}$$

The symmetric part has real eigenvalues, $\lambda_{ns} = \{-2.1132, 1.1132\}\ 1/s$, whose eigenvectors are orthogonal and correspond to the major and minor axes of an ellipse in short time stretching. The anti-symmetric part has imaginary eigenvalues, $\lambda_{na} = \{\pm 1.5938\mathbf{i}\}\ 1/s$, and corresponds to a rotation of the ellipse. The stretching and rotation processes are depicted in Figure F.6 and occur simultaneously. The dashed blue circle is the manifold of initial conditions, and the solid blue ellipse is the result after a short time, $\Delta t = 0.1\ s$. The eigenvectors of $\hat{\mathbf{J}}_s$ are the primary axes of the stretching corresponding to the symmetric part: the major axis, $\{0.1873, -0.9823\}$, shown is magenta, and grows as $\exp(1.1132t)$; the minor axis, $\{0.9823, 0.1873\}$, shown in cyan, decays as $\exp(-2.1132t)$. The counterclockwise

solid body rotation, which occurs at $51/32\ rad/s$, is indicated as yellow arrows. The stretching from the symmetric part is only valid for short time; for longer durations, the combination of stretching and rotation results in the eigenvalues of the normal Jacobian, $\hat{\mathbf{J}}$, dictating the evolution as shown in Figure F.5.

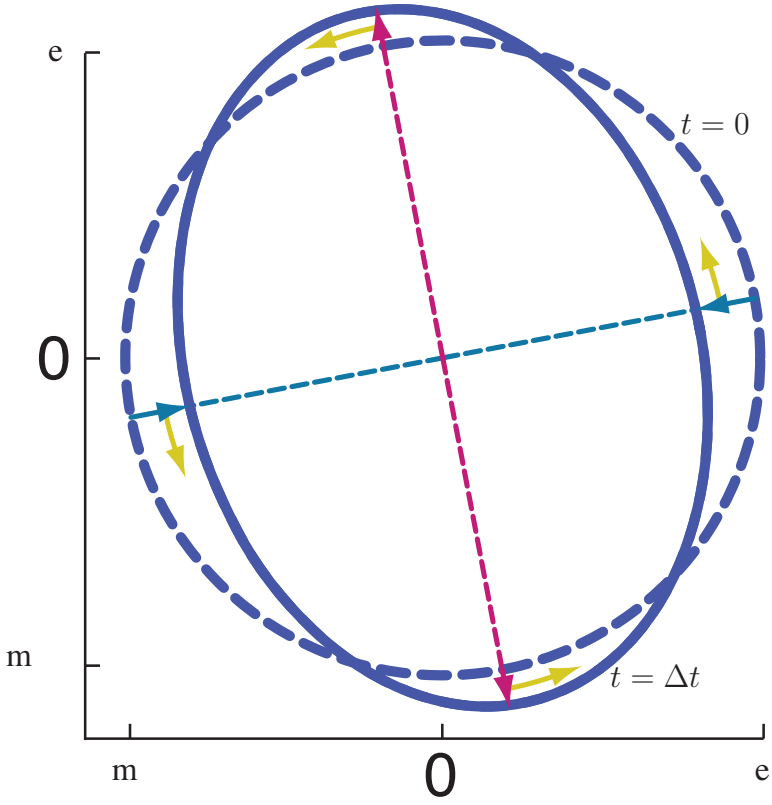

Figure F.6. Stretching and rotation in short time.

APPENDIX G

BERTINI HYDROGEN-AIR EQUILIBRIA FILES

The following is a `BERTINI` [109] input file used to identify the equilibria of the spatially homogeneous hydrogen-air CSTR from Section 5.2.

```
CONFIG

PRINTPATHMODULUS: 250;
TRACKTOLBEFOREEG: 1e-7;
TRACKTOLDURINGEG: 1e-7;
FINALTOL: 1e-11;
MAXNORM: 1e7;
SECURITYMAXNORM: 1e7;
SAMPLEFACTOR: 0.1;
TARGETTOLMULTIPLIER: 100;
AMPSAFETYDIGITS1: 2;
AMPSAFETYDIGITS2: 2;
CONDNUMTHRESHOLD: 1e100;

END;

INPUT

variable_group Z1,Z2,Z3,Z5,Z6,Z7;
function f1,f2,f3,f5,f6,f7;
constant q,rho,Z1In,Z2In,Z3In,Z5In,Z6In,Z7In,Z4,kj1,kj2,kj3,kj4,kj5,kj6,kj7,kj8,kj9,kj10,kj11,
     kj12,kj13,kj14,kj15,kj16,kj17,kj18,kj19,kj20,Kc1,Kc2,Kc3,Kc4,Kc5,Kc6,Kc7,Kc8,Kc9,Kc10,Kc11
     ,Kc12,Kc13,Kc14,Kc15,Kc16,Kc17,Kc18,Kc19,Kc20;

q = 10000/11;
rho = 37/40000;
Z1In = 10487131/1434890352;
Z2In = 10487131/1434890352;
Z3In = 0;
Z5In = 0;
Z6In = 0;
Z7In = 0;

kj1 = 1143860129615719642970361746847629547/250000000000000000000000000000000;
kj2 = 5909852972141319/4096;
kj3 = 1628888993217991/128;
kj4 = 3334888518636303/16384;
kj5 = 2519313429910801;
kj6 = 7500000000000;
kj7 = 5187237774867427/64;
kj8 = 8299580439787883/1024;
kj9 = 4804356598414959/1024;
kj10 = 4048582995951417/4;
kj11 = 2937403826326235/2;
kj12 = 10831910667233980;
kj13 = 16391024275106952;
kj14 = 989777376262101;
kj15 = 6014752887851375/128;
kj16 = 12500000000000;
kj17 = 2000000000000;
kj18 = 1500115727280437/134217728;
kj19 = 3783502520921157/16384;
kj20 = 2046771090666097/512;
```

```
Kc1 = 20170754999042307589046663096610245 7/62500000000000000000000000000000000000000;
Kc2 = 19110330959585528489697026088833808 9/40000000000000000000000000000000000000;
Kc3 = 53231110381254904950765194371342659/20000000000000000000000000000000000000;
Kc4 = 10737116858272700847809488777784281 41/12500000000000000000000000000000000000000;
Kc5 = 4275008033649445/65536;
Kc6 = 7129584254238697/32;
Kc7 = 1578149203837201/1048576;
Kc8 = 6563018317777155/16384;
Kc9 = 5561994438264127893489785492420196533/10000000000000000000000000000000000000000;
Kc10 = 30420266531846797393920;
Kc11 = 30420266531846797393920;
Kc12 = 30420266531846797393920;
Kc13 = 14533534032559932394438656;
Kc14 = 26130076528979287736320;
Kc15 = 69546649399236715442339 84;
Kc16 = 7640573354569225/16384;
Kc17 = 5850935575193973/268435456;
Kc18 = 13231702210664091450181563985768 8553/12500000000000000000000000000000000000000000000000;
Kc19 = 10697704002416023286059498786926 26953/50000000000000000000000000000000000;
Kc20 = 5487804912230929/536870912;

Z4 = 8835743/329411710;
Z8 = -2*Z1 + 2*Z2 + Z3 + Z6 - Z7;
Z9 = 10487131/1434890352 + Z1 - 2*Z2 - 3*Z3/2 - Z5/2 - Z6 + Z7/2;

ZM = (Z1 + Z2 + Z3 + Z4 + Z5 + Z6 + Z7 + Z8 + Z9);
ZM5 = (Z1 + 286*Z2/100 + 186*Z3/10 + 126*Z4/100 + Z5 + Z6 + Z7 + Z8 + Z9);
ZM10 = (Z1 + Z4 + Z5 + Z6 + Z7 + Z8 + Z9);
ZM1314 = (Z1 + Z2 + 5*Z3 + Z4 + Z5 + Z6 + Z7 + Z8 + Z9);

r1 = kj1*rho*(Z1*Z2 - Z5^2/Kc1);
r2 = kj2*rho*(Z2*Z5 - Z3*Z6/Kc2);
r3 = kj3*rho*(Z5*Z7 - Z1*Z6/Kc3);
r4 = kj4*rho*(Z2*Z7 - Z5*Z6/Kc4);
r5 = kj5*rho*ZM5*(rho*Z1*Z6 - Z8/Kc5);
r6 = kj6*rho*(Z5*Z8 - Z3*Z1/Kc6);
r7 = kj7*rho*(Z6*Z8 - Z5^2/Kc7);
r8 = kj8*rho*(Z7*Z8 - Z1*Z5/Kc8);
r9 = kj9*rho*(Z5^2 - Z3*Z7/Kc9);
r10 = kj10*rho*ZM10*(rho*Z6^2 - Z2/Kc10);
r11 = kj11*rho*(rho*Z6^2*Z2 - Z2^2/Kc11);
r12 = kj12*rho*(rho*Z6^2*Z3 - Z2*Z3/Kc12);
r13 = kj13*rho*ZM1314*(rho*Z5*Z6 - Z3/Kc13);
r14 = kj14*rho*ZM1314*(rho*Z6*Z7 - Z5/Kc14);
r15 = kj15*rho*ZM*(rho*Z7^2 - Z1/Kc15);
r16 = kj16*rho*(Z6*Z8 - Z1*Z2/Kc16);
r17 = kj17*rho*(Z8^2 - Z1*Z9/Kc17);
r18 = kj18*rho*ZM*(Z9 - rho*Z5^2/Kc18);
r19 = kj19*rho*(Z6*Z9 - Z2*Z8/Kc19);
r20 = kj20*rho*(Z5*Z9 - Z3*Z8/Kc20);

f1 = -r1 + r3 - r5 + r6 + r8 + r15 + r16 + r17 - q*(Z1 - Z1In);
f2 = -r1 - r2 - r4 + r10 + r11 + r12 + r16 + r19 - q*(Z2 - Z2In);
f3 = r2 + r6 + r9 + r13 + r20 - q*(Z3 - Z3In);
f5 = 2*r1 - r2 - r3 + r4 - r6 + 2*r7 + r8 - 2*r9 - r13 + r14 + 2*r18 - r20 - q*(Z5 - Z5In);
f6 = r2 + r3 + r4 - r5 - r7 - 2*r10 - 2*r11 - 2*r12 - r13 - r14 - r16 - r19 - q*(Z6 - Z6In);
f7 = -r3 - r4 - r8 + r9 - r14 - 2*r15 - q*(Z7 - Z7In);

END;
```

When BERTINI is executed with this input file, 97 real finite equilibria are identified and found in the file 'real_finite_solutions.'

BIBLIOGRAPHY

1. U.S. Department of Energy Annual Energy Review, report number: DOE/EIA-0384. http://www.eia.gov/aer/contents.html, 2009.

2. J. M. Powers. Review of multiscale modeling of detonation. *Journal of Propulsion and Power*, 22(6):1217–1229, 2006.

3. D. K. Manley, A. McIlroy, and C. A. Taatjes. Research needs for future internal combustion engines. *Physics Today*, 61(11):47, 2008.

4. S. Singh. *Rational Reduction of Reactive Flow Models and Efficient Computation of Their Solutions*. Ph.D. dissertation, University of Notre Dame, Notre Dame, Indiana, 2003.

5. M. J. Davis and R. T. Skodje. Geometric investigation of low-dimensional manifolds in systems approaching equilibrium. *Journal of Chemical Physics*, 111(3):859–874, 1999.

6. J. C. Robinson. *Infinite-Dimensional Dynamical Systems*. Cambridge University Press, Cambridge, 2001.

7. R. Temam. *Infinite-Dimensional Dynamical Systems in Mechanics and Physics*. Springer, Berlin, 1997.

8. E. N. Lorenz. Deterministic Nonperiodic Flow. *Journal of the Atmospheric Sciences*, 20(2):130–141, 1963.

9. M. J. Davis. Low-dimensional manifolds in reaction-diffusion equations. 1. Fundamental aspects. *Journal of Physical Chemistry A*, 110(16):5235–5256, 2006.

10. A. Adrover, F. Creta, M. Giona, and M. Valorani. Stretching-based diagnostics and reduction of chemical kinetic models with diffusion. *Journal of Computational Physics*, 225:1442–1471, 2007.

11. B. Sportisse. An analysis of operator splitting techniques in the stiff case. *Journal of Computational Physics*, 161(1):140–168, 2000.

12. W. Hundsdorfer and J. G. Verwer. *Numerical Solutions of Time-Dependent Advection-Diffusion-Reaction Equations*. Springer-Verlag, Berlin, Germany, 2003.

13. D. L. Ropp, J. N. Shadid, and C. C. Ober. Studies of the accuracy of time integration methods for reaction-diffusion equations. *Journal of Computational Physics*, 194(2):544–574, 2004.

14. A. N. Al-Khateeb and J. M. Powers. Analysis of the spatio-temporal scales of laminar premixed flames near equilibrium. *Combustion Theory and Modelling*, in review. Also see A. N. Al-Khateeb and J. M. Powers, Analysis of the Reaction-Advection-Diffusion Spectrum of Laminar Premixed Flames, 48th AIAA Aerospace Sciences Meeting and Exhibit, Orlando, Florida, AIAA 2010–0954, 2012.

15. K. Mazaheri, Y. Mahmoudi, and M. I. Radulescu. Diffusion and hydrodynamic instabilities in gaseous detonations. *Combustion and Flame*, 159(6):2138–2154, 2012.

16. R. B. Bird, W. E. Stewart, and E. N. Lightfoot. *Transport Phenomena*. John Wiley & Sons, New York, 1960.

17. L. D. Landau and E. Lifshitz. *Fluid Mechanics*. Pergamon, London, 1959.

18. J. F. Griffiths. Reduced kinetic-models and their application to practical combustion systems. *Progress in Energy and Combustion Science*, 21(1):25–107, 1995.

19. T. Lu and C. K. Law. Toward accommodating realistic fuel chemistry in large-scale computations. *Progress in Energy and Combustion Science*, 35(2):192–215, 2009.

20. W. G. Vincenti and C. H. Kruger. *Introduction to Physical Gas Dynamics*. John Wiley, New York, 1965.

21. J. D. Buckmaster and G. S. S. Ludford. *Theory of Laminar Flames*. Cambridge University Press, Cambridge, 1982.

22. J. D. Buckmaster. The structure and stability of laminar flames. *Annual Review of Fluid Mechanics*, 25:21–53, 1993.

23. S. Vajda, P. Valko, and T. Turanyi. Principle component analysis of kinetic-models. *International Journal of Chemical Kinetics*, 17(1):55–81, 1985.

24. L. Petzold and W. Zhu. Model reduction for chemical kinetics: an optimization approach. *AIChE Journal*, 45(4):869–886, 1999.

25. G. Li and H. Rabitz. A general-analysis of exact lumping in chemical-kinetics. *Chemical Engineering Science*, 44(6):1413–1430, 1989.

26. G. Li and H. Rabitz. A general-analysis of approximate lumping in chemical-kinetics. *Chemical Engineering Science*, 45(4):977–1002, 1990.

27. G. Li, A. S. Tomlin, H. Rabitz, and J. Tóth. A general analysis of approximate nonlinear lumping in chemical kinetics. I. unconstrained lumping. *Journal of Chemical Physics*, 101(2):1172–1187, 1994.

28. A. S. Tomlin, G. Li, H. Rabitz, and J. Tóth. A general analysis of approximate nonlinear lumping in chemical kinetics. II. constrained lumping. *Journal of Chemical Physics*, 101(2):1188–1201, 1994.

29. J. Warnatz, U. Maas, and R. W. Dibble. *Combustion*. Springer, Berlin, 2006.

30. J. C. Keck and D. Gillespie. Rate-controlled partial-equilibrium method for treating reacting gas-mixtures. *Combustion and Flame*, 17(2):237–241, 1971.

31. J. C. Keck. Rate-controlled constrained-equilibrium theory of chemical-reactions in complex-systems. *Progress in Energy and Combustion Science*, 16(2):125–154, 1990.

32. G. P. Beretta, J. C. Keck, M. Janbozorgi, and H. Metghalchi, The rate-controlled constrained-equilibrium approach to far-from-local-equilibrium thermodynamics. *Entropy*, 14(2):92–130, 2012.

33. Q. Tang and S. B. Pope. A more accurate projection in the rate-controlled constrained-equilibrium method for dimension reduction of combustion chemistry. *Combustion Theory and Modelling*, 8(2):255–279, 2004.

34. S. H. Lam. Using CSP to understand complex chemical kinetics. *Combustion Science and Technology*, 89(5-6):375–404, 1993.

35. S. H. Lam. The CSP method for simplifying kinetics. *International Journal of Chemical Kinetics*, 26(4):461–486, 1994.

36. U. Maas and S. B. Pope. Simplifying chemical kinetics: intrinsic low-dimensional manifolds in Composition Space. *Combustion and Flame*, 88(3-4):239–264, 1992.

37. V. Bykov, V. Gol'dshtein, and U. Maas. Simple global reduction technique based on decomposition approach. *Combustion Theory and Modelling*, 12(2):389–405, 2008.

38. M. Valorani and S. Paolucci. The G-Scheme: A framework for multi-scale adaptive model reduction. *Journal of Computational Physics*, 228(13):4665–4701, 2009.

39. E. N. Lorenz. On the existence of a slow manifold. *Journal of the Atmospheric Sciences*, 43(15):1547–1557, 1986.

40. S. J. Jacobs. Existence of a slow manifold in a model system of equations. *Journal of Atmospheric Sciences*, 48(7):893–901, 1991.

41. E. N. Lorenz. The slow manifold – what is it? *Journal of Atmospheric Sciences*, 49(24):2449–2451, 1992.

42. S. J. Fraser. The steady state and equilibrium approximations: a geometrical picture. *Journal of Chemical Physics*, 88(8):4732–4738, 1988.

43. M. R. Roussel and S. J. Fraser. Geometry of the steady-state approximation: perturbation and accelerated convergence methods. *Journal of Chemical Physics*, 93(2):1072–1081, 1990.

44. M. R. Roussel and S. J. Fraser. On the geometry of transient relaxation. *Journal of Chemical Physics*, 94(11):7106–7113, 1991.

45. H. G. Kaper and T. J. Kaper. Asymptotic analysis of two reduction methods for systems of chemical reactions. *Physica D*, 165(1-2):66–93, 2002.

46. C. W. Gear, T. J. Kaper, I. G. Kevrekidis, and A. Zagaris. Projecting to a slow manifold: singularly perturbed systems and legacy codes. *SIAM Journal on Applied Dynamical Systems*, 4(3):711–732, 2005.

47. F. Creta, A. Adrover, S. Cerbelli, M. Valorani, and M. Giona. Slow manifold structure in explosive kinetics. 1. bifurcations of points-at-infinity in prototypical models. *Journal of Physical Chemistry A*, 110(50):13447–13462, 2006.

48. M. Giona, A. Adrover, F. Creta, and M. Valorani. Slow manifold structure in explosive kinetics. 2. extension to higher dimensional systems. *The Journal of Physical Chemistry. A*, 110(50):13463–74, 2006.

49. A. N. Al-Khateeb, J. M. Powers, S. Paolucci, A. J. Sommese, J. A. Diller, J. D. Hauenstein, and J. D. Mengers. One-dimensional slow invariant manifolds for spatially homogenous reactive systems. *Journal of Chemical Physics*, 131(2):24118, 2009.

50. D. Lebiedz, J. Siehr, and J. Unger. A variational principle for computing slow invariant manifolds in dissipative dynamical systems. *SIAM Journal on Scientific Computing*, 33(2):703–720, 2011.

51. L. Perko. *Differential Equations and Dynamical Systems*. Springer, Berlin, 2001.

52. J. M. Powers and S. Paolucci. Uniqueness of chemical equilibria in ideal mixtures of ideal gases. *American Journal of Physics*, 76(9):848–885, 2008.

53. Y. B. Zel'dovich. A proof of the uniqueness of the solution of the equations for the law of mass action. *Zhurnal Fizicheskoi Khimii*, 11(5):685–687, 1938.

54. S. B. Pope. Gibbs function continuation for the stable computation of chemical equilibrium. *Combustion and Flame*, 139:222–226, 2004.

55. A. J. Sommese and C. W. Wampler. *The Numerical Solution of Systems of Polynomials*. World Scientific Publishing Company, Singapore, 2005.

56. A. Andronov. *Qualitative Theory of Second-Order Dynamic Systems*. Wiley, New York, 1973.

57. D. Lebiedz. Computing minimal entropy production trajectories: an approach to model reduction in chemical kinetics. *Journal of Chemical Physics*, 120(15):6890–6897, 2004.

58. D. Kondepudi and I. Prigogine. *Modern Thermodynamics*. John Wiley, New York, 1998.

59. M. M. Mamedov. On the incorrectness of the traditional proof of the Prigogine principle of minimum entropy production. *Technical Physics Letters*, 29(4):340–341, 2003.

60. L. M. Martyushev, A. S. Nazarova, and V. D. Seleznev. On the problem of the minimum entropy production in the nonequilibrium stationary state. *Journal of Physics A: Mathematical and Theoretical*, 40:371–380, 2007.

61. I. Müller. *Entropy and Energy: a Universal Competition*. Springer, Berlin, 2005.

62. A. N. Gorban and I. V. Karlin. Method of invariant manifold for chemical kinetics. *Chemical Engineering Science*, 58(21):4751–4768, 2003.

63. A. N. Gorban, I. V. Karlin, and A. Y. Zinovyev. Constructive methods of invariant manifolds for kinetic problems. *Physics Reports*, 396(4-6):197–403, 2004.

64. Z. Ren, S. B. Pope, A. Vladimirsky, and J. M. Guckenheimer. The invariant constrained equilibrium edge preimage curve method for the dimension reduction of chemical kinetics. *The Journal of Chemical Physics*, 124(11):114111, 2006.

65. Z. Ren and S. B. Pope. Reduced description of complex dynamics in reactive systems. *Journal of Physical Chemistry A*, 111:8464–8474, 2007.

66. M. J. Davis and A. S. Tomlin. Spatial dynamics of steady flames 1. phase space structure and the dynamics of individual trajectories. *Journal of Physical Chemistry A*, 112(34):7768–7783, 2008.

67. M. J. Davis and A. S. Tomlin. Spatial dynamics of steady flames 2. low-dimensional manifolds and the role of transport processes. *Journal of Physical Chemistry A*, 112(34):7784–7805, 2008.

68. Z. Ren and S. B. Pope. The use of slow manifolds in reactive flows. *Combustion and Flame*, 147(4):243–261, 2006.

69. U. Maas and S. B. Pope. Implementation of simplified chemical kinetics based on intrinsic low-dimensional manifolds. *Proceedings of the Combustion Institute*, 24:103–112, 1992.

70. U. Maas and S. B. Pope. Laminar flame calculations using simplified chemical kinetics based on intrinsic low-dimensional manifolds. *Proceedings of the Combustion Institute*, 25:1349–1356, 1994.

71. Z. Ren, S. B. Pope, A. Vladimirsky, and J. M. Guckenheimer. Application of the ICE-PIC method for the dimension reduction of chemical kinetics coupled with transport. *Proceedings of the Combustion Institute*, 31(1):473–481, 2007.

72. Z. Ren and S. B. Pope. Transport-chemistry coupling in the reduced description of reactive flows. *Combustion Theory and Modelling*, 11(5):715–739, 2007.

73. S. H. Lam. Reduced chemistry-diffusion coupling. *Combustion Science and Technology*, 179(4):767–786, 2007.

74. M. Hadjinicolaou and D. A. Goussis. Asymptotic solution of stiff PDEs with the CSP method: The reaction diffusion equation. *SIAM Journal on Scientific Computing*, 20(3):781–810, 1998.

75. S. Singh, J. M. Powers, and S. Paolucci. On slow manifolds of chemically reactive systems. *Journal of Chemical Physics*, 117(4):1482–1496, 2002.

76. V. Bykov and U. Maas. The extension of the ILDM concept to reaction-diffusion manifolds. *Combustion Theory and Modelling*, 11(6):839–862, 2007.

77. M. J. Davis. Low-dimensional manifolds in reaction-diffusion equations. 2. numerical analysis and method development. *Journal of Physical Chemistry A*, 110(16):5257–5272, 2006.

78. R. Haberman. *Applied Partial Differential Equations*. Pearson/Prentice Hall, Upper Saddle River, New Jersey, 2004.

79. C. Foias, G. R. Sell, and R. Temam. Inertial manifolds for nonlinear evolutionary equations. *Journal of Differential Equations*, 73(2):309–353, 1988.

80. E. S. Titi. On approximate inertial manifolds to the Navier-Stokes equations. *Journal of Mathematical Analysis and Applications*, 149:540–557, 1990.

81. T. R. Marchant. Cubic autocatalytic reaction-diffusion equations: semi-analytic solutions. *Proceedings of the Royal Society A*, 458:873–888, 2002.

82. R. Temam and D. Wirosoetisno. Slow manifolds and invariant sets of the primitive equations. *Journal of the Atmospheric Sciences*, 68(3):675–682, 2011.

83. M. Marion and R. Temam. Nonlinear Galerkin methods. *SIAM Journal of Numerical Analysis*, 26(5):1139–1157, 1989.

84. B. Garcia-Archilla and J. de Frutos. Time integration of the non-linear Galerkin method. *IMA Journal of Numerical Analysis*, 15:221–244, 1995.

85. R. Aris. *Elementary Chemical Reactor Analysis*. Dover, New York, 1999.

86. F. W. Schneider and A. F. Münster. Chemical oscillations, chaos, and fluctuations in flow reactors. *Journal of Physical Chemistry*, 95(6):2130–2138, 1991.

87. L. Györgyi and R. J. Field. Simple models of deterministic chaos in the Belousov-Zhabotlnsky reaction. *Journal of Physical Chemistry*, 95(17):6594–6602, 1991.

88. M. Desroches, J. Guckenheimer, B. Krauskopf, C. Kuehn, H. M. Osinga, and M. Wechselberger. Mixed-mode oscillations with multiple time scales. *SIAM Review*, 54(2):211–288, 2012.

89. A. L. Lin, M. Bertram, K. Martinez, H. L. Swinney, A. Ardelea, and G. F. Carey. Resonant phase patterns in a reaction-diffusion system. *Physical Review Letters*, 84:4240–4243, 2000.

90. P. Gray and S. K. Scott. Autocatalytic reactions in the isothermal, continuous stirred tank reactor - isolas and other forms of multistability. *Chemical Engineering Science*, 38(1):29–43, 1983.

91. P. Gray and S. K. Scott. Autocatalytic reactions in the isothermal, continuous stirred tank reactor - oscillations and instabilities in the system $A + 2B \rightarrow 3B$ – $B \rightarrow C$. *Chemical Engineering Science*, 39(6):1087–1097, 1984.

92. P. Gray and S. K. Scott. Sustained oscillations and other exotic patterns of behavior in isothermal reactions. *Journal of Physical Chemistry*, 89(1):22–32, 1985.

93. J. E. Pearson. Complex patterns in a simple system. *Science*, 261(5118):189–192, 1993.

94. T. Hsu, C. Mou, and D. Lee. Macromixing effects on the Gray-Scott model in a stirred reactor. *Chemical Engineering Science*, 51(11):2589–2594, 1996.

95. A. Doelman, T. J. Kaper, and P. A. Zegeling. Pattern formation in the one-dimensional Gray-Scott model. *Nonlinearity*, 10:523–563, 1997.

96. B. W. Boehm. *Software Engineering Economics*. Prentice Hall, 1981.

97. F. G. Blottner. Accurate Navier-Stokes results for the hypersonic flow over a spherical nosetip. *Journal of Spacecraft and Rockets*, 27(2):113–122, 1990.

98. P. J. Roache. *Verification and Validation in Computational Science and Engineering*. Hermosa, Albuquerque, New Mexico, 1998.

99. W. L. Oberkampf, T. G. Trucano, and C. Hirsch. Verification, validation, and predictive capability in computational engineering and physics. *Applied Mechanics Reviews*, 57(5):345–384, 2004.

100. W. L. Oberkampf and C. J. Roy. *Verification and Validation in Scientific Computing*. Cambridge University Press, Cambridge, 2010.

101. S. H. Lam and J. Bellan. On de-coupling of Shvab-Zel'dovich variables in the presence of diffusion. *Combustion and Flame*, 132(4):691–696, 2003.

102. J. A. Miller, R. E. Mitchell, M. D. Smooke, and R. J. Kee. Toward a comprehensive chemical kinetic mechanism for the oxidation of acetylene: comparison of model predictions with results from flame and shock tube experiments. *Proceedings of the Nineteenth Symposium (International) on Combustion, Combustion Inst.*, 19(1):181–196, 1982.

103. R. J. Kee, L. G. Dixon, J. Warnatz, M. E. Coltrin, and J. A. Miller. A Fortran computer code package for the evaluation of gas-phase multicomponent transport properties. Technical Report SAND86-8246, Sandia National Laboratories, 1991.

104. R. J. Kee, F. M. Rupley, and J. A. Miller. The chemkin thermodynamic database. Technical Report SAND87-8215B, Sandia National Laboratories, 1992.

105. K. Radhakrishnan and A. C. Hindmarsh. Description and use of LSODE, the Livermore solver for ordinary differential equations. Technical Report UCRL-ID-113855, Lawrence Livermore National Laboratories, 1993.

106. P. A. Davidson. *Turbulence*. Oxford University Press, Oxford, 2004.

107. S. Kalamatianos and D. G. Vlachos. Bifurcation behavior of premixed hydrogen/air mixtures in a continuous stirred tank reactor. *Combustion Science and Technology*, 109:347–371, 1995.

108. J. A. Miller and C. T. Bowman. Mechanism and modeling of nitrogen chemistry in combustion. *Progress in Energy and Combustion Science*, 15(4):287–338, 1989.

109. D. J. Bates, J. D. Hauenstein, A. J. Sommese, and C. W. Wampler. BERTINI, software for numerical algebraic geometry. available at `http://www.nd.edu/~sommese/bertini/`.

110. J. M. Powers. *Lecture Notes on Intermediate Fluid Mechanics*. Unpublished, available at `http://www.nd.edu/~powers/ame.60635/`. Version accessed 1 April 2012